LES of High-Re Reacting Flows: Active Scalar Conservation and Boundedness

A THESIS
SUBMITTED TO THE FACULTY OF THE GRADUATE SCHOOL
OF THE UNIVERSITY OF MINNESOTA
BY

Cheranellore Anand Vijay Kartha

IN PARTIAL FULFILLMENT OF THE REQUIREMENTS
FOR THE DEGREE OF
DOCTOR OF PHILOSOPHY

Graham V. Candler, Advisor

January, 2018

Acknowledgements

There are many people who I wish to thank for their contribution to my time in graduate school. First and foremost, I would like to thank my advisor, Prof. Graham V. Candler, for giving me an opportunity to be a student in his research group and for entrusting me with an interesting project. I'm thankful for his valuable advice and constant support during the project.

I'm indebted to my mentor, Dr. Pramod K. Subbareddy, for constantly motivating me and patiently answering all my naive questions. Frequent discussions with him helped me improve my understanding and gain a better perspective of the subject. I would also like to thank Profs. Ellen Longmire, Thomas Schwartzentruber and Krishnan Mahesh for teaching graduate school courses with a lot of passion. Their classes made me more interested in fluid dynamics. I'm grateful to Profs. Paul Dimotakis, Joseph Nichols, Terrence Simon and Sean Garrick for providing valuable suggestions during the my dissertation.

I would like to thank my colleagues in Prof. Candler's group for helping me during various stages of my work. I had several constructive discussions with Ioannis Nompelis, Pietro Ferrero, Sidharth GS., Ross Chaudhry, Jeffery Komives, Joseph Brock, Eric Stern, Alan Schwing, Sriram Doraiswamy, Aaron Neville, Derek Dinzl, John Reinert, John Thome, Tyler Hendrickson and other members in Prof. Candler's group without which this work would have been impossible. Also, my friends in the department, Yan Min Tan, Yixuan Li, Aswin Gnanaskandan, Savio Poovathingal, Prahlad Iyer, A. Rajapandian, Aman Verma, Durgesh Chandel and Anubhav Dwivedi helped me make my graduate school an enjoyable experience.

I'm glad to have made friends with Aditya GV., Sreekanth Narayanaswamy, Raghuveer Devulapalli, Pavani Medapuram, Divyanshu Pandey, Kanchan Kulkarni, Rahul

Saladi, Harita B, Aruna R., Suma Karnam, Palak Ambawani, Jyothi Joby, Davis Jose, Thaseem T., Jikku Thomas, G. Balaji, Neetha E., Govind Saraswat, Supriya T., Maya R., K. Ravindra, Ganesh R. and Tarun G. They have been like my extended family in Minneapolis. I have enjoyed their support and thank them for the memorable times we spent together in Minneapolis.

I feel lucky to continue to have close friendship with P. Ravi Teja, Nikhil Bandale, Karthik NV., Sapeksh V., Pramod Chandra, Phani Kishan, Varun T., Prathyusha E., Sadhvi S., Kshama Raj, P. Anusha and C. Jagadish. I cherish the friendship we had right from kindergarten and the umpteen number of things we learnt from each other over the years. Also, I wish to thank my teachers from school for continuous encouragement and care all through the years. I'm thankful to all of them for keeping me in positive spirits during my good times and bad.

I had several exciting discussions with Bhushan Maskay, Shameek Ganguly, Adeel Ahmed, Tejas Mehrotra, and many more friends during my undergraduate days which inspired me. I'm also thankful to Prof. Subhash C. Mishra and Prof. Vinayak Kulkarni, my advisors at IIT Guwahati, for always motivating me. This was one of the many factors that encouraged me to go to graduate school.

Last, and perhaps most importantly, I thank my parents Vijayalakshmy and Vijay Kumar, my sister Varada, my cheerful brother Achuth and my Grandparents for being there for me every single day during this journey. I don't think I would have made it this far without their constant prayers, support and motivation. I can't express enough thanks to Vasudevan, Madhusudanan, Rajendran, Sudha, Chandran, Bhaskaran Kartha and their families for extending their support, good wishes and valuable advices over the years. I've always felt the warmth and love of all the Cherusserry Madom family members, I thank you all for your support. During my undergraduate and graduate days I had the good fortune of living very close to my cousins Nisha, Suresh, Vinita, Raghu and their kids. I wish to express my sincere thanks to them for keeping me happy and for making me feel at home during these vital years. Thank you all!

Dedication

To Amma and Achan.
(In memory of Varada.)

Abstract

We aim to bring predictive capabilities to reacting flow simulations at high Reynolds numbers. In particular, we are interested in non-premixed reacting flows with realistic inflow conditions and heat release. These flows find their application in Scramjet engines, used for hypersonic propulsion. Higher-order, low-dissipation simulations of non-premixed combustion flows are often subject to numerical errors due to the presence of sharp gradients in species mass-fractions. These dispersive errors lead to overshoots and undershoots in species mass-fractions, resulting in violation of conservation of mass. In reacting flows, these errors result in overshoots of temperature above that allowed by the adiabatic flame temperature rise, rendering the simulations unreliable. To overcome this issue, we develop a new switched, low-dissipation flux methodology that mitigates these errors. The new method is validated on a range of one, two and three-dimensional problems, showing its effectiveness and promise to provide reliable solutions.

We use this newly developed method to simulate chemically reacting, spatially evolving subsonic and supersonic mixing layers at high Reynolds numbers. We investigate the effect of inflow conditions on subsonic reacting mixing layers, following the experiments of Slessor et al. [1], performed at the California Institute of Technology. Results from the simulations show close agreement to the experimentally measured velocity and temperature profiles, indicating that the entrainment and heat release is predicted with good accuracy. We also observe that varying the inflow conditions changes the nature of entrainment into the mixing layers, consistent with the past experimental observations. We also investigate the effect of heat release in supersonic reacting flows in an inclined ramp geometry, following the work of Bonanos et al. [2]. Probability density function plots and mass-fraction isosurfaces of 'tracer' species reveal that heat release significantly alters the flow field.

Contents

List of Tables

List of Figures

Chapter 1

Introduction

1.1 Motivation

Understanding the process of combustion in high-speed flows is of great interest due to its application to hypersonic propulsion. The aspect of efficient and sustained fuel-oxidizer combustion is not only of significant consequence in commercial aviation, but is also the mainstay for design and development of high-speed flight. This necessitates fundamental understanding of the physics of mixing and energy release in high-speed flows. Decades of research was thus focused on gaining in-depth understanding of various aspects of this topic through several experimental and computational studies. This thesis focuses on one of the aspects of mixing and combustion: fuel-oxidizer mixing at high Reynolds numbers, studied using large eddy simulations (LES).

Hypersonic vehicles (traveling at five times the speed of sound or faster) are propelled by a Scramjet engine, in which, fuel-oxidizer mixing occurs at supersonic speeds. Arriving at an engine design to provide sustained and efficient combustion, at these high speeds and turbulent flow conditions, is a task that has often been compared to keeping 'a match lit in a storm'. Meeting the dual objective of maintaining sustained and efficient combustion demands sound knowledge of fluid motion inside the engine and clear understanding of fuel-oxidizer interaction, both physically and chemically. Developing such an understanding, through numerical simulations, is the broad theme of this thesis.

Experiments conducted over several decades have provided invaluable data, enabling us to make big strides in our understanding of combustion in high-speed flows. However,

they are tremendously costly, requiring expensive instrumentation and have budgets that often run into many millions of dollars. In contrast, computational simulations are relatively inexpensive and provide a more detailed picture of the state of the flow at such conditions, providing the scope for exhaustive analysis. Computational simulations for these flows should have the capability to accurately represent flow features at the scale of the engine and should incorporate accurate models to account for chemical reactions which happen at the molecular level. This large range of length scales makes a fully resolved simulation (one that captures all the length scales) prohibitively expensive. To mitigate the cost, large eddy simulations (LES) of these flows are performed, where only the relatively large scales of motion in the flow are explicitly computed, while the smallest scales are represented using physical models. This thesis focuses on using accurate numerical methods in the LES framework to simulate and analyze high-speed reacting flows.

With the above mentioned objectives, simulations are performed to understand the physics in a mixing layer. A mixing layer is formed when of two parallel streams of fluids moving at different speeds, initially separated, interact with each other. When these fluids come in contact with each other, they form a wedge-like turbulent region where the two streams mix, changing the local composition, momentum and energy. The simple geometry of the mixing layer is ideal for studying a class of turbulent flows at different flow conditions. The effect of inflow conditions on the mixing layer evolution and heat release effects in a practical combustor geometry is studied here.

1.2 Brief overview of mixing layer studies

Decades of experimental work have helped to shed light on the physics of mixing layers. The structures in the flow field, the growth rate of the mixing layers, their dependence on velocity and density ratios, Mach number, inflow conditions, and heat release have been extensively studied through numerous experiments [7–18]. Physics of entrainment and changes induced due to species composition variation were also investigated [19–23].

Availability of large computational resources, along with advancements in numerical methods and modeling further enhanced the understanding in these flows. Predominantly, computational studies have investigated temporal mixing layers due to their

simple computational setup: enforcing streamwise and spanwise periodicity [24–31]. These simulations are powerful in bringing out the fundamental aspects like growth rate, nature of stresses and the pressure-strain behavior in a mixing layer. However, these simulations fail to capture the asymmetric entrainment and long-range coupling of the local flow behavior [32, 33], which are key features that determine the realistic growth rate, product formation and heat release in chemically reacting mixing layer flows. This demands the simulation of spatially-evolving mixing layers. A more detailed review of experimental and computational mixing layer studies is presented in Chapter 5.

Further, to understand the effect of heat release, reacting flow simulations in an inclined ramp geometry is also investigated. Low-speed simulations of this experimental study were done by Matheou [34], however, we are not aware of computational investigations at supersonic conditions in this geometry. Finally, we study reacting flows at supersonic conditions in an inclined ramp geometry to understand the effects of heat release in realistic geometries. In short, we study spatially-evolving mixing layers to understand the effects of inflow conditions and heat release, and provide a reliable framework for studying Scramjet propulsion.

1.3 Numerical issues in a reacting flow

Simulations of fuel-oxidizer mixing involve formation, destruction and transport of multiple species (or scalar fields, in general) and are often accompanied by heat release and density variations. Accurate computations of these non-premixed flows are a particular challenge because the thickness of the fuel/oxidizer interface scales inversely with Reynolds number. Sharp interfaces can also be present in the initial or boundary conditions. When higher-order numerical methods are used in LES of these flows, numerical (dispersive) errors [35] occur due to the presence of sharp gradients in species mass-fractions. These errors result in aphysical undershoots and overshoots in the scalar variables (*e.g.,* passive scalars, species mass fractions, or progress variable) leading to violation of conservation of mass. In reacting flows, this issue is aggravated as it leads to aphysical temperature rise and incorrect thermodynamics, rendering the simulation

data unreliable. This is usually the case if sufficient numerical dissipation is not provided in the regions where sharp gradients in species concentration are present. These numerical issues are especially prominent when low-dissipation methods are used, since sharp jumps in flow variables are not always coincident with regions of strong variation in the scalar fields: consequently, special detection mechanisms and dissipative fluxes are needed. Most numerical methods diffuse the interface, resulting in artificial mixing and spurious reactions. Addressing this issue is a preliminary requirement for reliable numerical simulations investigating reacting flows. In this thesis, a numerical method that mitigates this issue is proposed. The effectiveness of the developed method is demonstrated with several examples. Further, as the smallest scales in these simulations are not captured, using appropriate models to represent turbulence-chemistry interaction within a computational cell becomes relevant. Several variants of partially stirred reactor (PaSR) model that represent turbulence chemistry interaction are also explored in this thesis.

1.4 Scope of the present work

In this work, LES are performed using the US3D flow solver (a code developed at University of Minnesota) to investigate chemically reacting flows. We aim to develop a numerical method that mitigates dispersive errors resulting from sharp gradients in species mass fractions in such flows. Subsequently, the new numerical method is used to simulate experiments on mixing layers, studied at the California Institute of Technology.

In Chapter 2, the mathematical formulation, and various models and boundary conditions that facilitate the simulations in this study are described. Chapter 3 describes the numerical method used in the computations of the simulations presented here. The finite volume method, the newly developed bounded active scalar inviscid fluxes, the viscous fluxes and the time integration methods are discussed. Chapter 4 focuses on validation of the numerical method mentioned in Chapter 3. Results from multiple test problems are shown to demonstrate the performance and behavior of the numerical scheme. In Chapter 5, reacting and non-reacting mixing layer simulations at subsonic, high Reynolds number conditions with laminar and turbulent inflow conditions are studied. Supersonic-reacting mixing layers are studied in an inclined ramp geometry to

understand the effects of heat release in Chapter 6. Finally, Chapter 7 offers a discussion of the analyses presented in the thesis, and recommendations for future work.

Chapter 2

Mathematical formulation

2.1 Introduction

In this chapter, the mathematical formulation used to simulate multi-component reacting flows is discussed. Flows of interest in this study exhibit a large range of length scales. Computations of such a flow with grids that capture all the scales of the flow (direct numerical simulation or DNS) are extremely expensive. To make such flow computations tractable, LES is performed, where relatively large scales of motion in the flow are explicitly computed, while physical models are employed to represent the smallest scales. Such an approach involves filtering the governing equations at the size of the grid and using models to represent the physics at scales smaller than the grid size. In the following sections the filtered form of Navier-Stokes equations, the coupled partial differential equations of species, momentum and energy, are presented. Following this, the assumptions used in this work are summarized.

2.2 LES equations

The LES equations are obtained by spatially filtering the Navier-Stokes equations, the equations for conservation of mass (separate equations are solved for each of the species densities), momentum and energy. Using the notation $\widetilde{(\cdot)}$ to denote Favre averaging, $\tilde{f} = \overline{\rho f}/\overline{\rho}$, we get

$$\frac{\partial \bar{\rho}_s}{\partial t} + \frac{\partial \bar{\rho}_s \tilde{u}_j}{\partial x_j} = -\frac{\partial \bar{J}_{s,j}}{\partial x_j} - \frac{\partial \mathscr{V}_{s,j}}{\partial x_j} + \bar{\omega}_s \tag{2.1a}$$

$$\frac{\partial \bar{\rho}\tilde{u}_i}{\partial t} + \frac{\partial \bar{\rho}\tilde{u}_i\tilde{u}_j}{\partial x_j} = -\frac{\partial \bar{p}}{\partial x_i} + \frac{\partial \bar{\sigma}_{ij}}{\partial x_j} - \frac{\partial \tau_{ij}}{\partial x_j} \tag{2.1b}$$

$$\frac{\partial \bar{E}}{\partial t} + \frac{\partial}{\partial x_j}\left[(\bar{E}+\bar{p})\tilde{u}_j + \bar{q}_j - \bar{\sigma}_{ij}\tilde{u}_i + \sum_s \bar{\rho}_s \tilde{h}_s \tilde{v}_{s,j}\right] = -\frac{\partial}{\partial x_j}\left(\tilde{q}_{t,j} + \mathscr{J}_j - \mathscr{D}_j + \sum_s h_s^0 \mathscr{V}_{s,j}\right). \tag{2.1c}$$

In Eq. (2.1a-c), the species densities are denoted by $\rho_s \equiv \rho Y_s$, where Y_s is the mass fraction of species s. The filtered pressure, total energy, viscous shear stress, species diffusive flux and heat flux vector are $\bar{p}$, $\bar{E}$, $\bar{\sigma}_{ij}$, $\bar{J}_{s,j}$ and $\tilde{q}_j$ respectively.

Neglecting effects of vibrational non-equilibrium, the total energy per unit volume is defined as:

$$\bar{E} = \sum_s \bar{\rho}_s \int_0^{\tilde{T}} C_{v,s} dT + \frac{1}{2}\bar{\rho}\tilde{u}_k\tilde{u}_k + \sum_s \tilde{\rho}_s h_s^\circ + \bar{\rho}k \tag{2.2}$$

where, $\tilde{T}$ is the static temperature, while $C_{v,s}$ and h_s° are the specific heat at constant volume and the enthalpy of formation for species s, respectively. Using the perfect gas law and Daltons law for a multi-species system, pressure is expressed as:

$$\bar{p} = \sum_{n=1}^{ns} p_s = \sum_{n=1}^{ns} \bar{\rho}_s \frac{R}{M_s}\tilde{T}, \tag{2.3}$$

.

where R and M_s are the universal gas constant and species molecular weight, respectively. The source term due to chemical reactions is $\bar{\omega}_s$. The species enthalpy is defined as $\tilde{h}_s = \int_0^{\tilde{T}} C_{p,s} dT$. Here, $C_{p,s}$ is the species specific heat at constant pressure for species 's'.

2.2.1 Diffusive terms

The expressions for the viscous, thermal and mass diffusion terms, in the LES equations, are explained in this section. Viscous shear stress is expressed as (assuming Newtonian fluid and using Stokes' hypothesis):

$$\bar{\sigma}_{ij} = 2\mu\left(\tilde{S}_{ij} - \frac{1}{3}\tilde{S}_{kk}\delta_{ij}\right), \tag{2.4}$$

where, $\tilde{S}_{ij}$ is the symmetric part of the velocity gradient tensor, μ and κ are the dynamic viscosity and thermal conductivity coefficients. The dynamic viscosity is obtained using Sutherland's Law. Thermal (heat) diffusive fluxes are assumed to follow Fourier's Law

$$\tilde{q}_j = -k_i \nabla \tilde{T}, \tag{2.5}$$

where k and T are thermal conductivity for the mixture and temperature of the gas.

The species mass diffusion is driven by gradients of concentration, pressure, and temperature. In this work, we assume that the pressure gradients are small and neglect the effect of temperature gradients (Soret effect). Thus, the species mass diffusion is only dependent on gradients of species concentration. The species mass flux in the LES equations is expressed as

$$\bar{J}_{s,j} = \bar{\rho}_s \tilde{v}_{s,j}. \tag{2.6}$$

The diffusion velocities ($\tilde{v}_s$) for each species are then obtained by solving

$$\nabla \tilde{X}_s = \sum_{k=1}^{N} \frac{\tilde{X}_s \tilde{X}_k}{D_{sk}} (\tilde{v}_s - \tilde{v}_k) \tag{2.7}$$

where $\tilde{X}_s$ and D_{sk} are the mole fraction and diffusion coefficients of each species respectively. Although, a simple model assuming identical diffusion coefficients (Fick's law) could be used, in this work, the Hirschfelder-Curtiss approximation [36, 37] is used to handle multiple species with different molecular weights and diffusion coefficients. The resulting diffusion velocity is

$$\tilde{v}_s = -D_s \frac{\nabla \tilde{X}_s}{\tilde{X}_s} + \tilde{v}_c, \tag{2.8}$$

where D_s is the equivalent diffusion coefficient of species 's' in the mixture. It is important to note that D_s is not the binary diffusion coefficient, and in this work, D_s is obtained by assuming that each species diffuses into the most prominent diluent. The binary diffusion coefficient of each species is then calculated with respect to the most prominent diluent. In the reacting flow simulations studied here, the prominent diluent is nitrogen, and hence the binary diffusion coefficient for each species is calculated with respect to nitrogen. The diffusion coefficient for nitrogen, however, is assumed to be mixture mass diffusion obtained using a constant Lewis number. And, $\tilde{v}_c$ is the correction velocity, added to ensure global mass conservation. Summing up the individual

species mass conservation equations and enforcing conservation of mass, gives

$$\tilde{v}_c = \frac{1}{(\sum \tilde{X}_k \tilde{W}_k)} \sum_{k=1}^{N} D_s W_k \nabla \tilde{X}_k. \tag{2.9}$$

2.3 Sub-grid scale terms

Filtering the non-linear advection terms in the governing equations leads to terms that represent the physics at scales smaller than the local grid size (the filter width used in this study), and hence require modeling. The sub-grid scale (SGS) terms that need to be modeled are the SGS stress tensor, τ_{ij}, the turbulent mass flux, $\mathscr{V}_{s,j}$, the turbulent heat flux, $q_{t,j}$, the turbulent diffusion $\mathscr{J}_j$, and the SGS viscous diffusion $\mathscr{D}_j$. In this work, $\mathscr{J}_j$ and $\mathscr{D}_j$ are ignored. $\mathscr{V}_{s,j}$, τ_{ij} and $q_{t,j}$ are modeled using an eddy-viscosity assumption

$$\mathscr{V}_{s,j} = -\frac{\mu_t}{\mathrm{Sc_t}} \frac{\partial \tilde{c}_s}{\partial x_j}, \quad \tau_{ij} = -2\mu_t \left(\tilde{S}_{ij} - \frac{1}{3} \tilde{S}_{kk} \delta_{ij} \right), \quad q_{t,j} = -\frac{\mu_t}{\mathrm{Pr_t}} \frac{\partial \tilde{T}}{\partial x_j}, \tag{2.10}$$

in which $\tilde{S}_{ij}$ is the resolved rate of strain tensor, and the turbulent Schmidt, $\mathrm{Sc_t}$, and Prandtl, $\mathrm{Pr_t}$, numbers are constants of the model. The values of $\mathrm{Sc_t}$ and $\mathrm{Pr_t}$ used in this work are both set to 0.9. The turbulent viscosity μ_t ($\nu_t = \mu_t/\rho$) is obtained from the eddy-viscosity assumption using the Vreman turbulence model [38]. In the Vreman model,

$$\nu_t = c \sqrt{\frac{B_\beta}{\alpha_{ij}\alpha_{ij}}}, \tag{2.11}$$

$$\alpha_{ij} = \frac{\partial u_i}{\partial x_j}, \ \beta_{ij} = \Delta_m^2 \alpha_{mi} \alpha_{mj}, \tag{2.12}$$

$$B_\beta = \beta_{11}\beta_{22} - \beta_{12}^2 + \beta_{11}\beta_{33} - \beta_{13}^2 + \beta_{22}\beta_{33} - \beta_{23}^2. \tag{2.13}$$

The model constant c is related to the Smagorinky constant, C_s, by $c \approx 2.5 C_s^2$. The value of the Smagorinsky constant is set to 0.17 in this work. This model has been demonstrated to give reasonable agreement with experimental data for mixing layers and was shown to perform as well as the dynamic Smagorinsky model, while consuming significantly less computational time [38].

2.4 Chemical source terms

The source term $\bar{\omega}_s = \overline{\omega_s(\rho_s, T)}$ is a nonlinear function of the species concentrations and the temperature. In the present LES, this term is initially computed as

$$\overline{\omega_s(\rho_s, T)} \approx \omega_s(\tilde{\rho}_s, \tilde{T}), \tag{2.14}$$

which means that the effect of SGS turbulent fluctuations on the chemical source terms are neglected. This expression for the source term referred to as the 'laminar-chemistry' source term (or laminar finite-rate chemistry model) in this work.

Following the description given in Poinsot and Veynante [37], a generic chemical system of 'ns' species reacting with M reactions can be written as:

$$\sum_{n=1}^{ns} \nu'_{s,j} \mathscr{A}_s \leftrightharpoons \sum_{n=1}^{ns} \nu''_{s,j} \mathscr{A}_s \quad , \text{ for } \quad j = 1, .., M \tag{2.15}$$

$\mathscr{A}_s$ is the chemical symbol for species s, ν' and ν'' are molar stoichiometric coefficients for species s in the reaction M. Conservation of mass requires:

$$\sum_{n=1}^{ns} \left(\nu'_{s,j} - \nu''_{s,j}\right) \mathscr{A}_s = 0 \quad , \text{ for } \quad j = 1, .., M \tag{2.16}$$

The chemical source term for species s is the sum of the reaction rates $\omega_{s,j}$ of all M reactions,

$$\omega_s = \sum_{n=1}^{ns} \omega_{s,j} = \sum_{n=1}^{ns} \left(\mathscr{M}_s \sum_{n=1}^{M} \left(\nu'_{s,j} - \nu''_{s,j}\right) \mathscr{Q}_j \right) \tag{2.17}$$

where $\mathscr{Q}_j$ is the progress of the reaction j is a function of $[X_s]$:

$$\mathscr{Q}_j = k_{f_j} \prod_{n=1}^{ns} [X_s]^{\nu'_{s,j}} - k_{bj} \prod_{n=1}^{ns} [X_s]^{\nu''_{s,j}} \tag{2.18}$$

where k_{f_j} and k_{bj} are the forward and backward reaction rates, respectively. The forward rate is computed using the Arrehenius law,

$$k_{f_j} = C_{f_j} T^{\eta_j} \exp\left(\frac{-E_a}{RT}\right). \tag{2.19}$$

Here, the pre exponential factor, C_{f_j}, the temperature exponent, η_j, and the activation energy, E_a, are empirical coefficients. The backward reaction rates, k_{bj}, are obtained

from the forward rate and the equilibrium rate, K_{eq_j}, as :

$$k_{bj} = \frac{k_{f_j}}{K_{eq_j}}. \tag{2.20}$$

The equilibrium constant, however, is assumed to be a function of temperature alone, and is evaluated using the NASA Lewis curve-fits.

2.5 Sub-grid scale chemistry turbulence model

In the previous section, the chemical source terms were evaluated neglecting the effect of sub-grid scale turbulent fluctuations on the chemical source terms. In LES, neglecting these fluctuations implicitly assumes that the species in each cell is well mixed. However, in reality, the amount of mixing in a cell is determined by how quickly turbulence mixes the species. But, the assumption fails when the Damkohler number,

$$Da = \frac{t_s}{t_c}, \tag{2.21}$$

is high, where t_s represents the time scale of sub-grid scale turbulence and t_c is an estimate of the chemistry time scales. If the amount of time taken by turbulence to mix the species in the cell is less than the characteristic time for the reactions, then the assumption of neglecting the SGS chemical source term can be justified. Computations with the laminar chemistry assumption, often over-predict reactivity in a computational cell, resulting in higher product formation and temperature estimates. To address this issue, many models have been used by researchers, notably: flamelet progress variable (FPV), conditional moment closure (CMC), linear eddy model (LEM), filtered mass density function methods (FMDF), to name a few. Pitch [39], and more recently Fureby [40] present good reviews of the existing methods. These models involve tabulations, transporting additional conserved quantity like mixture fraction, their variance and/or assumptions of certain shape for mixture fraction distributions. In this study, a partially stirred reactor (PaSR) model is preferred as it serves as an easy-to-implement, yet effective representation of the turbulence-chemistry interaction at scales below the grid size. We follow the work of Fulton et al. [41], where a fraction, γ^*, is used to represent the unmixedness in a computational cell. Although they present multiple expressions

to estimate γ^*, in this work we choose to model γ^* along the lines of the PaSR-2 model in their work. Specifically,

$$\gamma^* = \frac{t_c}{\max(t_c, \frac{\mathrm{Re}_\Delta - 1}{\mathrm{Re}_\Delta} t_\mathrm{s})} \text{ where } \mathrm{Re}_\Delta = \frac{\max(\mathrm{u}'_\mathrm{SGS}, \frac{\nu}{\Delta})\Delta}{\nu}. \tag{2.22}$$

Here, Re_Δ is a measure of the local unsteadiness evaluated in a computational cell of width Δ, using an estimate for velocity fluctuations, u'_SGS, and the kinematic visosity, ν. By construction, γ^* in this model assumes a value of 1 in the laminar regions of the flow (as $\mathrm{Re}_\Delta \to 1$) and a positive fraction less than 1 in the turbulent regions of the flow. This behavior of the model and the relatively lower computational costs were the factors behind the choice of this model. Fulton et al. [41] evaluate t_c and t_s as:

$$\frac{1}{t_c} \equiv \frac{\max\left(\left\| \widetilde{\dot{\omega}}^+_{lam} \right\|, \left\| \widetilde{\dot{\omega}}^-_{lam} \right\| \right)}{\bar{\rho}} \tag{2.23}$$

$$\left\| \widetilde{\dot{\omega}}^+_{lam} \right\| = \left(\sum_{s=1}^{ns} \left(\dot{\omega}^+_{s,lam} \right)^2 \right)^{\frac{1}{2}} \tag{2.24}$$

$$\left\| \widetilde{\dot{\omega}}^-_{lam} \right\| = \left(\sum_{s=1}^{ns} \left(\dot{\omega}^-_{s,lam} \right)^2 \right)^{\frac{1}{2}} \tag{2.25}$$

$$t_s = \frac{\Delta}{\max(u'_{SGS}, \frac{\nu}{\Delta})} \tag{2.26}$$

$$u'_{SGS} = \sqrt{\frac{1}{3}\left(\overline{\tilde{u}}^2 - \overline{\tilde{u}}^2 + \overline{\tilde{v}}^2 - \overline{\tilde{v}}^2 + \overline{\tilde{w}}^2 - \overline{\tilde{w}}^2 \right)} \tag{2.27}$$

A quantity with an overline is defined as:

$$\bar{q}_{i,j,k} = \frac{1}{2} q_{i,j,k} + \frac{1}{12}(q_{i-1,j,k} + q_{i+1,j,k} + q_{i,j-1,k} + q_{i,j+1,k} + q_{i,j,k-1} + q_{i,j,k+1}) \tag{2.28}$$

In this work, however, two changes were made to this model. First, the expression to estimate the chemistry time scale is modified as

$$\frac{1}{t_c} \equiv \frac{\max\left(\left\| \widetilde{\dot{\omega}}^+_{lam} \right\|, \left\| \widetilde{\dot{\omega}}^-_{lam} \right\| \right)}{\bar{\rho} - \bar{\rho}_\mathrm{inert}}, \tag{2.29}$$

where ρ_{inert} is the density of inert gases, while all other estimates are kept unchanged. We refer to this model as PaSR-2a. The modification to the expression of t_c makes the estimate smaller than that obtained with Eq. 2.23. This leads to an increase in the local estimate of Da, which results in lower values of γ^*. In PaSR-2 and PasR-2a, γ^* effectively represents the fraction of the cell volume in which the reactants are assumed to be well mixed. But, in PaSR-2b, we assume that only a fraction of the number of moles of the reactants in a computational cell are well-mixed. Hence, $\gamma^*(\rho_s/M_s)$ would represent the mole-densities that effectively contribute to the evaluation of the chemical source terms. So, in this model, we retain all the estimates from PaSR-2a, but evaluate the source term as:

$$\overline{\omega_s(\rho_s, T)} \approx \omega_s(\gamma^* \tilde{\rho}_s, \tilde{T}). \tag{2.30}$$

For a general set of chemical reactions, this model scales the source term depending on the order of reactions. However, as the set of reactions considered here are second order chemical reactions, $\overline{\omega_s(\rho_s, T)} \approx \gamma^{*2} \omega_s(\tilde{\rho}_s, \tilde{T})$.

2.6 Boundary Conditions

2.6.1 Subsonic outflow boundary conditions

Inaccurate treatment of boundary conditions for realistic flows at subsonic conditions results in numerical errors that significantly affect the flow field predictions. Writing the governing equations in the characteristic form elucidates that one of the characteristics in a subsonic flow propagates information upstream, while the others carry information downstream. Inability to handle this upstream-traveling characteristic at the boundaries, causes spurious wave reflections. The presence of long-range downstream to upstream coupling in flows like subsonic mixing layers enables feedback of these errors, thereby self-exciting the mixing layers, affecting the growth rate [32, 42]. Several modeling approaches have been reported in the literature to minimize erroneous reflections at the domain boundaries in convectively unstable flows like the mixing layers and wakes. Colonius [43] presents a review of these methods and a comparative study of the recently developed methods has been reported by Granet et al. [44].

The characteristic form of the Navier-Stokes equations enables distinct identification

of outgoing and incoming waves. These equations are written as

$$\begin{bmatrix} \left(\frac{\partial p}{\partial t} - \rho c \frac{\partial u_1}{\partial t}\right) \\ \left(c^2 \frac{\partial \rho}{\partial t} - \frac{\partial p}{\partial t}\right) \\ \left(\frac{\partial u_2}{\partial t}\right) \\ \left(\frac{\partial u_3}{\partial t}\right) \\ \left(\frac{\partial p}{\partial t} + \rho c \frac{\partial u_1}{\partial t}\right) \\ \left(\frac{\partial \rho_s}{\partial t}\right) \end{bmatrix} + \begin{bmatrix} \mathcal{L}_1 \\ \mathcal{L}_2 \\ \mathcal{L}_3 \\ \mathcal{L}_4 \\ \mathcal{L}_5 \\ \mathcal{L}_{5+s} \end{bmatrix} + \begin{bmatrix} \mathcal{T}_1 \\ \mathcal{T}_2 \\ \mathcal{T}_3 \\ \mathcal{T}_4 \\ \mathcal{T}_5 \\ \mathcal{T}_{5+s} \end{bmatrix} = \begin{bmatrix} 0 \\ 0 \\ 0 \\ 0 \\ 0 \\ \dot{\omega}_s \end{bmatrix}. \tag{2.31}$$

in the work by Yoo et al. [45] where, c is the speed of sound. $\mathcal{L}$ is the amplitude of the waves given by:

$$\vec{\mathcal{L}} = \begin{pmatrix} \vec{\mathcal{L}}_1 \\ \vec{\mathcal{L}}_2 \\ \vec{\mathcal{L}}_3 \\ \vec{\mathcal{L}}_4 \\ \vec{\mathcal{L}}_5 \\ \vec{\mathcal{L}}_{5+s} \end{pmatrix} = \begin{pmatrix} \lambda_1 \left(\frac{\partial p}{\partial x_1} - \rho c \frac{\partial u_1}{\partial x_1}\right) \\ \lambda_2 \left(c^2 \frac{\partial \rho}{\partial x_1} - \frac{\partial p}{\partial x_1}\right) \\ \lambda_3 \frac{\partial u_2}{\partial x_1} \\ \lambda_4 \frac{\partial u_3}{\partial x_1} \\ \lambda_5 \left(\frac{\partial p}{\partial x_1} + \rho c \frac{\partial u_1}{\partial x_1}\right) \\ \lambda_{5+s} \left(\frac{\partial \rho_s}{\partial x_1}\right), \end{pmatrix}. \tag{2.32}$$

where, $\lambda_1 = u_1 - c,\ \lambda_5 = u_1 + c,\ \lambda_{2,3,4,5+s} = u_1$, are the characteristic velocities with x_1 being the flow direction. And, the transverse terms are:

$$\vec{\mathcal{T}} = \begin{pmatrix} \vec{\mathcal{T}}_1 \\ \vec{\mathcal{T}}_2 \\ \vec{\mathcal{T}}_3 \\ \vec{\mathcal{T}}_4 \\ \vec{\mathcal{T}}_5 \\ \vec{\mathcal{T}}_{5+s} \end{pmatrix} = \sum_{i=2,3} \begin{pmatrix} u_i \left(\frac{\partial p}{\partial x_i} - \rho c \frac{\partial u_i}{\partial x_i}\right) + \gamma p \frac{\partial u_i}{\partial x_i} \\ u_i \left(c^2 \frac{\partial \rho}{\partial x_i} - \frac{\partial p}{\partial x_i}\right) + c^2 \rho \frac{\partial u}{\partial x_i} - \gamma p \frac{\partial u_i}{\partial x_i} \\ u_i \frac{\partial u_2}{\partial x_i} + \frac{1}{\rho} \frac{\partial p}{\partial x_i} \\ u_i \frac{\partial u_3}{\partial x_i} + \frac{1}{\rho} \frac{\partial p}{\partial x_i} \\ u_i \left(\frac{\partial p}{\partial x_i} + \rho c \frac{\partial u_i}{\partial x_i}\right) + \gamma p \frac{\partial u_i}{\partial x_i} \\ u_i \left(\frac{\partial \rho_s}{\partial x_i}\right) \end{pmatrix}, \tag{2.33}$$

where γ is the ratio of specific heats. The slowly traveling acoustic wave, associated with λ_1, is an incoming wave at a subsonic outflow. The incoming waves at the boundaries depend on information from outside the domain, which are yet to be determined and need to be modeled. All the other waves (outgoing waves) at the boundaries depend only on the information from inside the computational domain, which makes the

evaluation trivial. Poinsot & Lele [46] use locally one-dimensional inviscid (LODI) assumptions for the Navier-Stokes characteristic based boundary conditions (NSCBC) to obtain the amplitude of the incoming waves. However, for a three-dimensional flow at the boundary, these assumptions have to be improved by including the contributions from the transverse terms. Inclusion of transverse terms have been shown to handle flow distortions more effectively than the LODI assumption [45, 47]. The LODI assumption along with the transverse terms, neglecting viscous, diffusive and body forces, is used to solve for primitive quantities as:

$$\frac{\partial}{\partial t}\begin{pmatrix}\rho\\ u\\ v\\ w\\ p\\ \rho_s\end{pmatrix}+\begin{pmatrix}(\mathcal{L}_1+\mathcal{L}_5+2\mathcal{L}_2)/2c^2\\ (\mathcal{L}_5-\mathcal{L}_1)/2\rho c\\ \mathcal{L}_3\\ \mathcal{L}_4\\ (\mathcal{L}_5+\mathcal{L}_1)/2\rho c\\ \mathcal{L}_{5+s}\end{pmatrix}+\begin{pmatrix}(\mathcal{T}_1+\mathcal{T}_5+2\mathcal{T}_2)/2c^2\\ (\mathcal{T}_5-\mathcal{T}_1)/2\rho c\\ \mathcal{T}_3\\ \mathcal{T}_4\\ (\mathcal{T}_5+\mathcal{T}_1)/2\rho c\\ \mathcal{T}_{5+s}\end{pmatrix}=\begin{pmatrix}0\\ 0\\ 0\\ 0\\ 0\\ \dot{\omega}_s\end{pmatrix}, \tag{2.34}$$

Here, the amplitude of the incoming wave is prescribed as:

$$\mathcal{L}_1 = K(p-p_t)+(\beta-1)\mathcal{T}_1 = 0. \tag{2.35}$$

So, the effective boundary condition is then written as

$$\left(\frac{\partial p}{\partial t}-\rho c\frac{\partial u_1}{\partial t}\right)+K(p-p_t)+\beta\mathcal{T}_1 = 0. \tag{2.36}$$

In the above equation, $K = \frac{\sigma c(1-M^2)}{l_x}$ as proposed by Rudy & Strikwerda [48] and $\beta \in [0,1]$. M is the maximum Mach number at the boundary and l_x is the characteristic size of the domain in x_1 direction. Although the value of σ when set to zero represents a perfectly non-reflecting boundary condition, is seen to cause reflections and does not help to maintain the desired pressure at the boundary [45,47,49]. In most cases, σ is set to a value between 0.25 and 0.27. The value of β, the transverse damping parameter, is 1 in the study by Poinsot & Lele [50], and assumes a value of either a mean Mach number over the boundary, $\overline{M} = \overline{\frac{u(x,t)}{c(x,t)}}$, or a local Mach number, $M_l = \frac{u(x,t)}{c(x,t)}$, in the study by Yoo & Im [45]. In this study, we follow the characteristic based approach presented in Yoo & Im and set β to $\overline{M}$.

2.6.2 Subsonic inflow boundary conditions

The boundary condition at the subsonic inflow depends on the upstream-traveling information from inside the computational domain. Disregarding this information and holding the primitives at the ghost cell to a constant, leads to an aphysical rise in pressure at the inflow. Such a change in inflow conditions proves to be detrimental for flows that are extremely sensitive to the boundary conditions, like mixing layers. To overcome this issue, in this work, NSCBC boundary conditions for subsonic inflow are implemented as mentioned in Poinsot & Lele [46]. The velocity, u_1, at the inflow is imposed, which leads to

$$\mathcal{L}_5 = \mathcal{L}_1 - 2\rho c\frac{du}{dt}. \tag{2.37}$$

Further, imposing a temperature for the incoming stream gives

$$\mathcal{L}_2 = \frac{1}{2}(\gamma - 1)(\mathcal{L}_5 + \mathcal{L}_1) + \frac{\rho c^2}{T}\frac{dT}{dt}. \tag{2.38}$$

The above equations help in obtaining density at the inflow boundary as

$$\frac{\partial \rho}{\partial t} + d_1 + \frac{\partial(\rho u_2)}{\partial x_2} = 0, \text{ where } \mathrm{d_1} = \frac{1}{\mathrm{c}^2}\left[\mathcal{L}_2 + \frac{1}{2}(\mathcal{L}_2 + \mathcal{L}_5)\right] \tag{2.39}$$

where, u_2 and x_2 are the transverse velocity and direction respectively.

2.7 Inflow turbulence

In most practical flow configurations, the incoming streams are turbulent. Simulations of such flows either require a very long upstream domain to allow the flow to reach a fully turbulent state or need an appropriate prescription of turbulent flow conditions. Large computational costs associated with the former approach necessitate implementing reliable, yet, practical methods for the latter. Common practices in the literature rely on 'library-based' methods, recycling-rescaling-based methods and synthetic turbulence generators. The review papers by Dhamankar et al. [51] and Wu [52] provide a good overview of various methods to prescribe inflow turbulence. Each of these methods has many approaches to generate artificial turbulence and each approach has inherent advantages and shortcomings. In all of these approaches, however, the goal is to generate

time-dependent inflow conditions that would mimic the realistic turbulent flow. Such conditions are generated by constructing a fluctuating field for flow variables that satisfy first and higher-order moments, spatial correlations (single and two-point), turbulent kinetic energy spectra and integral length scales in the mean. If not satisfying all the conditions, reliable methods try to satisfy at least a few of them.

Library based methods use stored sets of information from a secondary simulation run prior to the primary simulation. In some cases the primary simulation could also use stored data from a simultaneous run. The stored information is then transferred to the inflow plane of the primary simulation and imposed as the fluctuating turbulent field [53]. Although practical constraints limit the large data storage, many studies have focused on mitigating such issues by clever use of smaller data sets [54–57]. Turbulence injection with this method is realistic as it is obtained from a secondary simulation run at conditions close to that of the main simulation. But, the issue of storing large data sets, the uncertainty of extent of data required, and the frequent reading and writing required from and to the disk during the primary simulation raise pragmatic concerns.

Recycling-rescaling based turbulent injection relies on a secondary simulation (usually of flat plate boundary layers) performed on a short domain. In this method, the secondary simulation is run simultaneously with the primary simulation (the simulation of practical flow configurations) with information transferred from the secondary to the primary simulation. In the secondary simulation, the mean and the fluctuating quantities at the outflow of this simulation are appropriately scaled using similarity laws and fed back into the inflow [58–61]. The information so generated at a downstream location is used as the inflow plane for the primary simulation. To avoid the complexity of two simulations being run synchronously in parallel with data transfer, the secondary simulation, is included in the primary simulation as an upstream domain in many studies. In spite of the fact that this method is good for flat plate boundary layers, disadvantages of this method include the need to have a good starting fluctuation field for turbulence generation (to avoid re-laminarization) [62,63], the possibility of introducing low frequency behaviors [56], and the complexities associated with accurate information exchange between outflow and inflow planes of the secondary simulation in a parallel framework.

While the above mentioned methods depend on auxiliary simulations for prescribing the fluctuations at the inflow, synthetic turbulence generators rely on mathematical tools to replicate turbulent statistics at the inflow boundary. Numerous techniques including those based on Fourier transform, proper orthogonal decomposition, phase information, digital filter technique, diffusion, vortex method and synthetic eddy models have been applied in the literature [64–72] (an extensive literature review is presented in Dhamankar et al. [51]). These turbulent flow generators can, however, only satisfy certain turbulent flow statistics at the inflow boundary. So, unlike the library based and recycling-rescaling based methods, the synthetic turbulence generators need to include a development region in the simulations, for the injected fluctuations to evolve and resemble realistic turbulence. This shortcoming might restrict the use of these generators in certain practical simulations where the addition of an upstream domain becomes infeasible. However, the ability of these approaches to generate data in real time without the requirement of concurrent simulations, complex data exchanges in a parallel framework and large data storage gives these methods a slight upper hand. For these reasons, synthetic turbulence generation is used in this work, and specifically, digital filter based inflow turbulence generation is implemented.

2.7.1 Digital filter based inflow turbulence generation

Initially, the digital filter method requires 'p' random numbers with zero mean and unit variance. If r_k, for $k = 1, .., p$, is the set of random numbers (generated using the Mersenne-Twister algorithm [73]), then $\Sigma_{k=1}^{p} r_k/p = 0$ and $\overline{r_k r_k} = 1$ is a preliminary requirement. This requirement can be met by using the Box-Muller theorem which ensures the desired properties for pair of numbers (c, d) obtained from two independent numbers (a, b) uniformly distributed in (0,1] such that $c = \sqrt{-2\ln(a)}\cos(2\pi b)$ and $d = \sqrt{-2\ln(a)}\sin(2\pi b)$. A linear filter is subsequently applied on this random field, such that

$$\nu_k \equiv F_N(r_k) = \sum_{j=-N}^{N} b_j r_{k+j}. \tag{2.40}$$

In this one-dimensional filtering operation, the filter coefficients b_k are approximated as

$$b_k \approx \frac{\tilde{b}_k}{\left(\sum_{j=-N}^{N} \tilde{b}_j^2\right)^{1/2}} \quad \text{with} \quad \tilde{b}_k = \exp\left(-\frac{\pi x}{n}\right). \tag{2.41}$$

'n' in the above equation is defined as $I_x/\Delta x$, where I_x is the integral length scale. This form for b_j is obtained assuming an exponential two point-correlation (see Touber & Sandham [74], Xie & Castro [75]). In the two-dimensional case, the filter coefficients are expressed as a convolution $b_{jk} = b_j b_k$. This leaves us with prescribing relevant integral length scales in the flow. In this work we use curve fits to the data presented in Pirozzoli & Bernardini [76], to obtain the value of the integral length scales. Now, to impose streamwise correlation (essentially to avoid three-dimensional filtering), the filtered filed is modified as:

$$\mathfrak{f}_k = \mathfrak{f}_k^{old} \exp\left(-\frac{\pi \Delta t}{2\tau}\right) + \nu_k \sqrt{1 - \exp\left(-\frac{\pi \Delta t}{\tau}\right)}, \tag{2.42}$$

where Δt is the time-step, $\tau = I_x/U$ and U is the mean streamwise velocity. After the two-point correlations are prescribed, Lund's transformation [77] is used to prescribe the single-point correlation as follows:

$$\begin{bmatrix} u(0,y,z,t) \\ v(0,y,z,t) \\ w(0,y,z,t) \end{bmatrix} = \begin{bmatrix} \langle u(0,y,z)\rangle \\ \langle v(0,y,z)\rangle \\ \langle w(0,y,z)\rangle \end{bmatrix} + [\mathscr{R}] \begin{bmatrix} \mathfrak{f}_u(y,z) \\ \mathfrak{f}_v(y,z) \\ \mathfrak{f}_w(y,z) \end{bmatrix} \tag{2.43}$$

$$\text{where, } \mathscr{R} = \begin{bmatrix} \sqrt{R_{11}} & 0 & 0 \\ R_{21}/\sqrt{R_{11}} & \sqrt{R_{22} - \left(R_{21}/\sqrt{R_{11}}\right)^2} & 0 \\ 0 & 0 & \sqrt{R_{33}} \end{bmatrix}. \tag{2.44}$$

Here, the values of R_{ij} are obtained as curve fits to the data in Degraff & Eaton [78]. In the subsonic cases, thermodynamic fluctuations are assumed to be very small, hence neglected. However, for supersonic flows thermodynamic fluctuations are obtained using the strong Reynolds analogy.

Chapter 3

Numerical Method

3.1 Introduction

In this chapter, the numerical method used for solving the coupled partial differential equations discussed in Chapter 2 is described. First, the numerical challenges associated with multi-component flow are introduced with a review of relevant approaches in the literature. Then, discretization and the approximations used in solving the weak form of the Navier-Stokes equations are discussed in the context of the finite volume method. Finally, a novel approach for inviscid flux evaluation that addresses the challenges outlined in Chapter 1 is presented. We conclude this chapter with the discussion of viscous flux evaluation and time integration methods used in this work.

3.2 Numerical challenges in multi-component flows

Accurate computations of scalar fields in high Reynolds number compressible flows pose several numerical challenges. Thin interfaces must be resolved without excessive numerical diffusion: this requires the use of relatively high-order, low dissipation schemes that promise to resolve these high wavenumber features. In addition, it is often crucial that the physical bounds on the scalar values set by the initial and boundary values of the simulation are not violated. For instance, we would like to ensure that the mass fractions of chemical species are individually in the range $[0, 1]$ and to sum to unity; naively correcting deviations from this can result in a scheme that does not conserve

mass. The use of spatially high-order methods in reacting flow calculations often results in local undershoots and overshoots in the species mass fractions, causing aphysical results. This results in mass fraction or other scalar non-conservation, and for reacting cases, these errors can cause temperatures to exceed that allowed by the adiabatic flame temperature rise. In other cases, we would like to ensure that scalar concentrations are everywhere strictly in some range of prescribed values. This includes passive scalar fields, mass fractions of chemical species and transported turbulence quantities, among many other examples. While the use of high-order, low-dissipation schemes for the computation of compressible flow is now fairly commonplace, the issue of ensuring scalar boundedness has received less attention, and is the focus of this thesis. Consider the usual inviscid conservation equations for mass, along with the equation for the evolution of a scalar in compressible flow

$$\frac{\partial \rho}{\partial t} + \frac{\partial \rho u_j}{\partial x_j} = 0 \tag{3.1}$$

$$\frac{\partial \rho \phi}{\partial t} + \frac{\partial \rho \phi u_j}{\partial x_j} = 0, \tag{3.2}$$

where the symbols have the same definitions as in Chapter 2. Combining equations (3.1) and (3.2), it is easy to show that

$$\frac{\partial \phi}{\partial t} + u_j \frac{\partial \phi}{\partial x_j} = 0, \tag{3.3}$$

implying that for the inviscid equations, in the absence of source terms, ϕ is a purely convected quantity which should be bounded by initial and boundary values. We would like to ensure that the numerical method for solving equations (3.1)–(3.2) respects this in a discrete sense.

Note that preserving the positivity of density and pressure (or internal energy) while solving the conservation equations for mass, momentum and energy is a related numerical issue that has been the subject of several discussions in the literature. Given initial conditions with positive density and pressure, a positivity preserving scheme will produce solutions which also have positive density and pressure: these schemes usually have an additional CFL constraint that guarantees this property. Of course, this CFL restriction should not be excessive for the methods to be useful. Perthame [79] constructed positivity preserving Boltzmann type schemes for the Euler equations. Perthame and

Shu [80], in a pioneering paper demonstrated that higher-order positive schemes in space and time could be built from one-dimensional, first-order building blocks and specially constructed high-order reconstructions. In a similar vein, Linde and Roe [81] showed that given a first order one-dimensional positive scheme, one can construct a second-order, multidimensional MUSCL type scheme that is also positive: notably, the analysis uses a generic finite-volume formulation that should work for unstructured meshes as well. The notion of positivity preservation has played an important role in the construction of several popular approximate Riemann solvers as well: we mention, in particular, its influence on the HLLE [82] and AUSM [83] schemes.

In a series of recent papers, Zhang and Shu [84–86], building on the idea in Perthame and Shu [80], and incorporating the idea of a 'linear-scaling limiter' from Liu and Osher [87], developed genuinely high order finite volume and discontinuous Galerkin schemes that satisfy the strict maximum principle for scalar conservation laws and the positivity principle for the Euler equations, when certain CFL conditions are satisfied. Hu, Adams and Shu [88] later constructed a positive flux-limiter scheme for the Euler equations which also produces positive solutions, under a slightly less restrictive CFL condition.

Note that artificial viscosity methods based on the paper by von Neumann and Richtmyer [89] form the basis for a distinct and increasingly popular set of numerical schemes that can be used to address some of these issues. We refer the reader to section 3.3 in the review paper by Pirozzoli [90] for background and relevant references. In the context of the issues discussed here, we mention the work of Cook and Cabot [91] who use a sensitive detector formed using high-order derivatives to create a low dissipation artificial viscosity method. Fiorina and Lele [92] and Cook [93] extended the method to multi-species calculations by augmenting the physical diffusivity coefficients with artificial ones. We note that the artificial diffusion term for species diffusivity in Cook's [93] formulation is sensitized to global mass fraction bounds via the use of Heaviside functions (equation 18 in [93]).

Let us assume that we have a finite volume code that satisfactorily solves the mass, momentum and energy equations. The method may or may not be strictly positivity preserving for the density and pressure (the code should stop with an error message of some sort if the density or pressure assume negative values). The fluxes in the method

should satisfy the entropy condition in order to prevent physically ambiguous solutions. For time accurate, unsteady simulations, the dissipation terms in the fluxes may be damped by a shock-detecting switch to localize the numerical diffusion. Given this common framework, we would like to add additional transport equations describing, for example, passive scalars, multiple chemical species (perhaps in lieu of the total mass conservation equation), or advected variables that feed into a turbulence model. The key question we examine here relates to achieving bounded (maximum-principle satisfying) schemes that also have low levels of dissipation for these fields.

It should be noted that, for compressible flow as well as flows with strong density variation, numerical methods that aim to preserve the maximum principle for fields determined by (3.2) should take into account (3.1) (the variation of the density field) as well: these equations are strongly coupled and the discretization should respect this.

3.3 Finite volume method

The conservation equations are written in compact form as:

$$\frac{\partial U}{\partial t} + \nabla \cdot \vec{F} = W. \tag{3.4}$$

Here, U is the vector of conserved variables, $\vec{F}$ is total fluxes, and W is the vector of source terms. The total flux $\vec{F}$ is split into convective (inviscid) and diffusive flux vectors as

$$F_j = F_{Ij} + F_{vj}, \tag{3.5}$$

where the index j stands for directions in the Cartesian co-ordinate system. These terms are

$$U = \begin{pmatrix} \rho_s \\ \rho u \\ \rho v \\ \rho w \\ \rho \phi \\ \rho e_v \\ E \end{pmatrix}, \quad F_{Ij} = \begin{pmatrix} \rho_s u_j \\ \rho u u_j + p\delta_{1j} \\ \rho v u_j + p\delta_{2j} \\ \rho w u_j + p\delta_{3j} \\ \rho \phi u_j \\ \rho e_v u_j \\ (E+p)u_j \end{pmatrix}, \quad F_{vj} = \begin{pmatrix} \rho_s v_j \\ -\tau_{1j} \\ -\tau_{2j} \\ -\tau_{3j} \\ 0 \\ q_{vj} + \rho e_v v_j \\ F_{Ev} \end{pmatrix}, \quad W = \begin{pmatrix} \omega_s \\ 0 \\ 0 \\ 0 \\ \omega_\phi \\ \omega_v \\ 0 \end{pmatrix}, \tag{3.6}$$

where, $F_{Ev} = q_j + q_{v_j} - (\vec{\tau}_{ij}\vec{u}_j) + \sum_{n=1}^{ns} \rho_s h_s v_{js}$. Here, we include an equation for a generic conserved passive scalar, $\rho\phi$, and the equation for the vibrational energy, ρe_v. w_v and q_v representing the source terms and heat flux corresponding to the vibrational energy. In Eqs. (3.6), we have used both u_j $(j = 1, 2, 3)$ and u, v, w to denote the velocity components. The vibrational energy is coupled to the total energy (defined below), and the equation can be considered a surrogate for other equations that are similarly coupled (such as the subgrid kinetic energy, for instance). The total energy,

$$E = \sum_s \rho_s C_{v,s} T + \frac{1}{2}\rho(u^2 + v^2 + w^2) + \rho e_v + \sum_s \rho_s h_s^0,$$

is the sum of the internal, kinetic and vibrational energies and the mass-weighted sum of the heats of formation (h_s^0) of each of the component species. The mass fraction of species s is $Y_s = \frac{\rho_s}{\rho}$, and we can alternatively write the species transport equations as

$$\frac{\partial \rho Y_s}{\partial t} + \frac{\partial \rho Y_s u_j}{\partial x_j} = 0 \qquad s = 1, ..., ns. \tag{3.7}$$

In this multi-component system, the mean molecular mass of the mixture is

$$M = \sum_s X_s M_s = \frac{1}{\sum_s \frac{Y_s}{M_s}}$$

and the mole and mass fractions are related by $X_s = Y_s M / M_s$. Using this we can define $p = \rho R T$, where $R = R_u / M$. We can also define a mean value for C_v using $C_v = \sum_s Y_s C_{v,s}$ and a mean ratio of specific heats (C_p/C_v) for the mixture, γ,

$$\frac{1}{\gamma - 1} = \sum_s \frac{X_s}{\gamma_s - 1} = \frac{\sum_s Y_s C_{v,s}}{\sum_s Y_s R_u / M_s}.$$

With this set of equations, we do not solve for the total density directly; the sum of the ns species densities defines ρ. For the inviscid non-reacting form of the equations, it is easy to show that each Y_s is a purely convected quantity:

$$\frac{DY_s}{Dt} = 0.$$

The strong form of the conservation equations, as mentioned in Eq. 3.4, is integrated over an arbitrary control volume Ω (a cell in the computational domain) to obtain the

weak form of the conservation equation. Invoking the Green's Theorem, the resulting weak form of the conservative equation is

$$\frac{\partial \bar{U}}{\partial t} + \frac{1}{V} \oint_{\Omega} (\vec{F} \cdot \hat{n}) dS = \bar{W}, \tag{3.8}$$

where V is the total volume, $\hat{n}$ is the outward pointing normal to the surface, $\bar{U}$ and $\bar{W}$ are averaged over Ω. When the considered volume is a computational cell, the resulting fluxes are effectively summed over the faces and Eq. 3.8 becomes

$$V_i \frac{\partial U_i}{\partial t} = -\sum_{\mathsf{f}} F'_{\mathsf{f}} S_{\mathsf{f}} + V_i \bar{W}. \tag{3.9}$$

where U_i is the volume averaged value of the vector of conserved variables in cell i bounded by the faces indexed by f and F'_{f} is the flux at the face f and S_{f} is its area.

3.4 Inviscid flux evaluation

Considering only the inviscid fluxes (discarding viscous and source terms), the Eq. 3.8 in its semi-discrete form is:

$$V_i \frac{\partial U_i}{\partial t} = -\sum_{\mathsf{f}} F'_{\mathsf{f}} S_{\mathsf{f}}. \tag{3.10}$$

where

$$F'_{\mathsf{f}} = \begin{pmatrix} \rho_s u' \\ \rho u u' + p s_x \\ \rho v u' + p s_y \\ \rho w u' + p s_z \\ \rho \phi u' \\ \rho e_v u' \\ (E+p) u' \end{pmatrix}_{\mathsf{f}}.$$

Note that (s_x, s_y, s_z) are the direction cosines of the unit-normal to face f. The prime denotes a dot product: $u' = u s_x + v s_y + w s_z$ is the face-normal velocity. The flux vector for these equations is homogeneous of degree one: $F'_{\mathsf{f}}(\alpha U) = \alpha F'_{\mathsf{f}}(U)$.

As with the single-component flow equations, there are several choices for the variables we reconstruct at the face. For consistency with the choice for the single-component flow equations that gives us a stable, kinetic-energy consistent method [94], we elect to

reconstruct u, v, w and p. This leaves us with the task of picking ns additional variables to represent the thermodynamic state. There are several feasible options: for instance, we could reconstruct the density, ρ, and any $ns-1$ of the species mass fractions; the ns species densities ρ_s; the partial pressures p_s, or combinations of the above. We choose to reconstruct the ns species densities, ρ_s: this choice will be justified later.

Let us consider the one-dimensional version for simplicity[1] for a cell i of size h, spanning $x_i - h/2 \leq x \leq x_i + h/2$, and with a simple Euler forward[2] time discretization, we get

$$U_i^{n+1} = U_i^n - \lambda \left(F_{i+1/2} - F_{i-1/2} \right),$$

where $\lambda = \Delta t/h$. U is the vector of conserved quantities, $F_{i+1/2} = F(U^L_{i+1/2}, U^R_{i+1/2})$ is the numerical approximation to the flux at face $i+1/2$ between cells i and $i+1$. The states U^L and U^R are reconstructed approximations to the fields on the left and right side of the face, respectively: the first-order version of the flux $F_{i+1/2}$ would be $F(U_i, U_{i+1})$. Typically, the flux is computed as the approximate solution to the Riemann problem at the face with U^L and U^R as the adjacent states: a prototypical example is the Roe-type flux function

$$F_{i+1/2}(U^L, U^R) = \underbrace{F_{c,i+1/2}(U^L, U^R)}_{\text{symmetric}} - \underbrace{\frac{1}{2}|\mathbb{A}_{i+1/2}| \left(U^R - U^L \right)}_{\text{dissipative}}. \tag{3.11}$$

In the above equation, $F_{c,i+1/2}$ is a centered approximation to the flux and $\mathbb{A}_{i+1/2}$ is the Jacobian matrix $\partial F/\partial U$, computed either using density-weighted averages of the left and right states, for the Roe flux [96], or simple averages, as in the modified Steger-Warming scheme [97]. $|\mathbb{A}|$ is computed as $\mathbb{R}|\Lambda|\mathbb{R}^{-1}$ after applying an eigen-decomposition, $A = \mathbb{R}\Lambda\mathbb{R}^{-1}$, where Λ is the diagonal matrix of eigenvalues, and $\mathbb{R}$ is the matrix of right eigenvectors of A. The eigenvalues in Λ are usually modified to satisfy the entropy condition. The simpler and more dissipative Lax-Friedrichs flux has a similar form, except that the matrix $|\mathbb{A}|$ is replaced by its (global or local) maximum eigenvalue, $\lambda_{\max}$. In many versions of "low-dissipation" schemes (see [90]), including the ones we

[1] This is not necessarily an over-simplification of the problem since it is possible to construct multidimensional schemes using one-dimensional building blocks [80, 81].

[2] Similarly, using a first-order time discretization is not overly restrictive if we can express the high order time integrator as a convex combination of first-order schemes: for instance, the SSP TVD Runge-Kutta methods of Gottlieb, Shu and Tadmor [95] achieve this.

consider here, the dissipative portion of the flux is damped by a multiplicative factor $\alpha_{i+1/2} \in [0,1]$ in order to localize the dissipation: an elegant and popular example of this shock-detecting switch is due to Ducros [98].

3.4.1 Symmetric flux

The construction of the symmetric/central portion of the flux uses the notion of a kinetic-energy consistent method presented in [94]. In one dimension, the central flux is

$$F'_{c,\mathsf{f}} = \begin{pmatrix} \rho_1 u \\ \vdots \\ \rho_{ns} u \\ \rho u u + p \\ \rho \phi u \\ \rho e_v u \\ (E+p)u \end{pmatrix}_{\mathsf{f}}.$$

symmetric average values of the variables ρ_s, u, ϕ and p are computed at each face f and used in the flux. Note that $\rho = \sum_s \rho_s$. On structured meshes, high order polynomials are constructed in each cell: the averages of their traces on either side of each face are used to define the face values. We elaborate on this in the next section. For unstructured grids, nominally high order face values are found using gradient based reconstructions. For example, at a face f separating cells l and r, using

$$u_{\mathsf{f}} = \frac{u_l + u_r}{2} + \frac{8}{15}\left(\nabla u_l \cdot \Delta x_{\mathsf{f},l} + \nabla u_r \cdot \Delta x_{\mathsf{f},r}\right) - \frac{1}{45}\left(\nabla u_{l2} \cdot \Delta x_{\mathsf{f},l2} + \nabla u_{r2} \cdot \Delta x_{\mathsf{f},r2}\right)$$

gives a sixth-order approximation to u_{f} on a uniform mesh. In the expression above, $l2$ and $r2$ are the cells to the left and right, respectively, of cells l and r. $\Delta x_{\mathsf{f},l}$ is the vector connecting the center of cell l to the center of the face f, and Δu_l is the gradient of u at cell l. A sketch is shown in figure (3.1). The coefficients 8/15 and 1/45 can be adjusted for non-uniform grids.

Note that the reconstruction of ρ_s and ϕ will need to be modified from the expression above to achieve boundedness. This is discussed in the following sub-sections; reconstruction of the other variables is not affected.

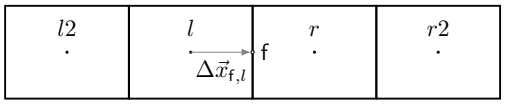

Figure 3.1: Sketch of the stencil used for the inviscid flux reconstruction at face f using data from cell centers l, r, $l2$ and $r2$.

Broadly speaking, most finite volume methods that attempt to prevent spurious overshoots in solution quantities (not just the scalar fields) use variants of two basic ideas. Assume that we can find a low-order flux function F^{low} that gives bounded results, even if it is diffusive: for instance, first order Lax-Friedrichs, HLLE or Steger-Warming fluxes could be used. The flux-corrected transport (FCT) method of Boris and Book [99] (see also Zalesak [100]) essentially involves composing the numerical flux at a face as a blend of low-order and high-order ("anti-diffusive" in their terminology) fluxes,

$$F_{i+1/2} = F^{\text{low}}_{i+1/2} + \beta(F^{\text{high}}_{i+1/2} - F^{\text{low}}_{i+1/2}),$$

and attempting to find the maximum value of $\beta \in [0, 1]$ that preserves a desirable quality of the scheme, such as monotonicity and scalar boundedness, for example. The second, more prevalent method is to express the high-order states that determine the flux function as

$$U^L = U_i + \delta U_i \quad \text{and} \quad U^R = U_{i+1} + \delta U_{i+1},$$

and to limit the variation from the first-order state in a manner that preserves desirable properties of the solution; in other words, $\delta U_{i,i+1}$ are replaced with limited versions $\widehat{\delta U}_{i,i+1}$. We use the latter approach.

3.4.2 Species fluxes: Active scalar boundedness

In the governing equations, the 'ns' individual species densities equations, without the diffusion terms, represent Lagrangian transport of mass fractions with the flow. Clearly, these 'active' scalars are strongly coupled to the flow: a flux of species s carries with it, in addition to mass, a fraction of the momentum and enthalpy. This coupling can be seen in the structure of the entropy eigenvectors in equation (3.13). Ensuring boundedness for advected scalars is a challenge that has been discussed at length in the works

of Subbareddy, Candler and Ferrero [101], Matheou & Dimotakis [35] and later in Subbareddy, Kartha and Candler [102]. While Matheou & Dimotakis [35] present the issues of passive scalars clearly, the work by Subbareddy, Candler and Ferrero [101] present a numerical method to address them in the context of passive scalars. Building on the previous work, Subbareddy, Kartha and Candler [102] extend the study to include the numerical issues in the context of active scalars. In the case of active scalars, apart from preserving sensible bounds for Y_s, there are a few other issues that arise while considering species flux forms:

Choice of reconstructed variable: The reconstructed variables play an important role. The passive scalar formulation discussed in the previous section would suggest that we reconstruct Y_s and ρ separately. However, this turns out to be a poor choice in our framework. While this approach (in conjunction with the use of a linear scaling type limiter) can preserve scalar boundedness, we observe large excursions in the temperature field which rapidly degrades the solution and defeats one of the original purposes of attempting to preserve scalar bounds - controlling temperature overshoots in multispecies flow calculations. In this context, Terashima et al. [103] point out the role of the molar concentration, $c = \sum_s c_s = \sum_s \rho_s/M_s = \rho/M$, in the temperature prediction. The temperature is updated at each time step using

$$T = \frac{p}{\rho R} = \frac{pM}{\rho R_u} = \frac{p}{R_u c},$$

and errors in the molar concentration c have a strong influence on the solution. It is useful to examine the simple case of transport in a uniform velocity field. The molar concentration c obeys

$$\frac{\partial c}{\partial t} + \frac{\partial c u_j}{\partial x_j} = 0$$

for the inviscid equations. In a uniform velocity field, if the initial molar concentration is also uniform, it should not change with time. As a simple example, consider a one-sided linear reconstruction,

$$\rho_{s,\mathsf{f}} = \frac{3}{2}\rho_{s,i} - \frac{1}{2}\rho_{s,i-1}.$$

Dividing by M_s and summing over all species gives $c_\mathsf{f} = \frac{3}{2}c_i - \frac{1}{2}c_{i-1}$. On the other hand,

using the split form

$$\rho_{s,\mathsf{f}} = \rho_{\mathsf{f}} Y_{\mathsf{f}} = \left(\frac{3}{2}\rho_i - \frac{1}{2}\rho_{i-1}\right)\left(\frac{3}{2}Y_{s,i} - \frac{1}{2}Y_{s,i-1}\right),$$

gives $c_{\mathsf{f}} = \rho_{\mathsf{f}}\left(\frac{3}{2M_i} - \frac{1}{2M_{i-1}}\right)$. If the initial concentration is uniform, interpolating ρ_s preserves the uniform value at the face, while the split form does not. Since the temperature excursions while using the split form are significant, we use reconstructed values of ρ_s at the face in the species fluxes.

Bounded polynomial reconstruction: The mass fractions Y_s must still obey the global bounds: $0 \leq Y_s \leq 1$. Since by definition,

$$Y_s = \frac{\rho_s}{\sum_k \rho_k},$$

we need to ensure that each of the species densities, ρ_k, is greater than or equal to zero to meet this constraint. Denoting the polynomial that represents the variation of ρ_k in cell i with $r_{k,i}(x)$, the linearly scaled version,

$$\tilde{r}_{k,i}(x) = \rho^n_{k,i} + \theta_{k,i}(r_{k,i}(x) - \rho^n_{k,i}), \quad \theta_{k,i} = \min\left\{|\frac{\rho^n_{k,i}}{m_{k,i} - \rho^n_{k,i}}|, 1\right\}, \tag{3.12}$$

could be used to help preserve the positivity of ρ_k. The polynomial smoothly transitions to a low order representation as θ assumes small values. Although the linear scaling limiter is very effective in preserving boundedness for the passive scalar cases we have looked at, it is constrained by the fact that the global bounds $m_{k,i}$ and $M_{k,i}$ appear in its definition: it is agnostic of sharp local gradients in the species densities when they are not close to the bounds m or M. This may result in spurious oscillations in these regions if the order of the central reconstruction is not lowered to prevent interpolation on a stencil containing steep solution variations. A simple remedy is to use locally defined bounds (M_{local}, m_{local}) in the definition of θ; however, this results in excessively diffusive solutions. We find that using a jump detector,

$$J_{k,i} = (1 - s_{k,i})^p, \qquad s_{k,i} = \frac{|2g_i g_{i+1}|}{g_i^2 + g_{i+1}^2 + \epsilon}, \qquad g_{k,i} = (\nabla \rho_k)_i\,,$$

where p is an integer (we use p =2 or 4) and ϵ prevents division by zero, is an effective way to achieve this. The jump detector J is incorporated by modifying the definition

of θ in equation (3.12) as follows

$$\theta'_{k,i} = 1 - J_{k,i}\,(1 - \theta_{k,i})\,.$$

The form of the jump detector is inspired by Harten's ACM switch [104]; while there are a large number of alternative definitions for J, this form is an effective, localized, jump detector for the cases we tested.

Dissipative flux: While using the linearly scaled reconstructions, the factor $\theta_{k,i}$ in equation (3.12) above effectively functions as a switch that detects possible excursions of the species density below zero. However, for compressible flow simulations on coarse grids, there will be regions where the solution profiles are too sharp to be resolved, even when the bounds are respected: this could be the result of initial conditions with sharp jumps or due to shocks or contact/material discontinuities. If these steep gradients are ignored, the solutions are extremely dispersive, as one might expect. These jumps in the species densities can be present (quasi-) independently of jumps in the other flow variables, and the goal is to control these without excessively dissipating the flow field. To achieve this we need an efficient low-dissipation switch, $0 \leq \beta_{s,i+1/2} \leq 1$, that signals the presence of a steep variation in the solution. For single component flow, the dissipative fluxes in equation (3.11) are damped by a shock detecting switch, α_{shock}. For the multispecies equations, given switches β_s that detect jumps in the species densities, we selectively add additional dissipation of the form

$$-\frac{1}{2}\sum_s \max(0, \beta_s - \alpha_{\mathsf{shock}})\lambda_1 w_s \mathbb{e}_s,$$

where $\mathbb{e}_s$ is the entropy eigenvector corresponding to species s, λ_1 is nominally the magnitude of the convective eigenvalue, $|u'|$, and w_s is the associated characteristic variable constructed using local solution averages and the jumps, $\Delta U = U^R - U^L$ at the face, as described in section (3.4.3). The values of $U^{L/R}$ used to construct ΔU are a linear combination of MUSCL interpolants and the traces of the limited polynomials: the linear factor is the jump detection switch β_s. Note that the other waves, and in particular the shear and acoustic waves are not affected by the added diffusion: this serves to significantly lower the overall levels of numerical dissipation.

Low-dissipation switch: For applications where the locally available stencil of surrounding cell values is small, finding an effective switch β_s is a significantly challenging

task. A switch based on local gradients of flow variables such as the Ducros switch used for shock detection would be ideal. In addition, the switch must be robust enough to ignore relatively tiny local variations in the solution. One version we found effective is a variant of Harten's ACM switch [104] due to Ren et al. [105]:

$$\sigma_i = \min_s \frac{\left|2\Delta f_{s,i+1/2}\Delta f_{s,i-1/2}\right| + \epsilon}{(\Delta f_{s,i+1/2})^2 + (\Delta f_{s,i-1/2})^2 + \epsilon}$$
$$\beta_{i+1/2} = \{\max(1-\sigma_i, 1-\sigma_{i+1})\}^p$$

where ϵ sets the threshold for the switch and is problem dependent: we use $\epsilon = 10^{-7}$ for the cases in this paper. The exponent p (not to be confused with the pressure) is a small integer: we have used values up to 4 for the cases presented. The function f_s in the switch is a suitable function of the flow variables: in the original version, characteristic variables are used. Among the options tested, $f_s = \rho_s$, where $\hat{n}$ is the face-normal unit vector, was found to be particularly effective, and is used for the results in this thesis.

3.4.3 Dissipative flux: the eigenvector decomposition

Using the notation $h = (E+p)/\rho$ for the specific enthalpy, and denoting the speed of sound by a, the matrix of eigenvectors, $\mathbb{R}$ in the eigen-decomposition above (in one dimension) is given by

$$\mathbb{R} = \begin{pmatrix} 1 & 0 & \cdots & 0 & 0 & 0 & Y_1 & Y_1 \\ 0 & 1 & & 0 & 0 & 0 & Y_2 & Y_2 \\ \vdots & & \ddots & & & & & \vdots \\ 0 & 0 & & 1 & 0 & 0 & Y_{ns} & Y_{ns} \\ u & u & & u & 0 & 0 & u+a & u-a \\ \phi & \phi & & \phi & 1 & 0 & \phi & \phi \\ e_v & e_v & & e_v & 0 & 1 & e_v & e_v \\ \frac{\partial E}{\partial \rho_1} & \frac{\partial E}{\partial \rho_2} & \cdots & \frac{\partial E}{\partial \rho_{ns}} & 0 & \frac{1}{\rho}\frac{\partial E}{\partial e_v} & h+au & h-au \end{pmatrix}, \tag{3.13}$$

where the entries are formed using a suitable average (arithmetic or density weighted, for example). The partial derivatives in the matrix are

$$\frac{\partial E}{\partial \rho_s} = \left(C_{v,s} - \frac{C_v}{R}\frac{R_u}{M_s}\right)T + \frac{u^2}{2} + h_s^0, \quad \frac{\partial E}{\partial e_v} = \rho.$$

An arbitrary $\Delta U^f = U^R - U^L$ is expressed as a projection onto the columns of $\mathbb{R}$ (the eigenvectors). The coefficients of this expansion are the characteristic variables:

$$\mathbb{R}^{-1}\Delta U^f = \begin{pmatrix} \Delta\rho_1^f - \frac{Y_1}{a^2}\Delta\tilde{p}^f \\ \Delta\rho_2^f - \frac{Y_2}{a^2}\Delta\tilde{p}^f \\ \vdots \\ \Delta\rho_{ns}^f - \frac{Y_{ns}}{a^2}\Delta\tilde{p}^f \\ \Delta\left(\rho\phi\right)^f - \phi\Delta\rho^f \\ \Delta\left(\rho e_v\right)^f - e_v\Delta\rho^f \\ \frac{1}{2a^2}\left\{\Delta\tilde{p}^f + a\Delta(\rho u)^f - au\Delta\rho^f\right\} \\ \frac{1}{2a^2}\left\{\Delta\tilde{p}^f - a\Delta(\rho u)^f + au\Delta\rho^f\right\} \end{pmatrix}. \tag{3.14}$$

The pseudo pressure-jump that appears above is

$$\Delta\tilde{p}^f = \sum_k \frac{\partial p}{\partial U_k}\Delta U_k^f,$$

where U_k is the k-th component of the state vector U. The matrix of eigenvalues is $\Lambda = \mathrm{Diag}\left(\lambda_1, \cdots, \lambda_1, \lambda_p, \lambda_m\right)$, where the first $ns+2$ entries are equal to λ_1, which represents (nominally) the magnitude of the convective eigenvalue $|u'|$. λ_p and λ_m similarly represent $|u'+a|$ and $|u'-a|$. These eigenvalues are modified from their nominal values using a correction factor: for example, $\lambda_1 = \sqrt{|u'|^2 + \epsilon a^2}$, where ϵ is a small number. The first ns characteristic variables and the corresponding columns of $\mathbb{R}$ represent 'entropy waves', and the last two correspond to acoustic waves.

Note that the one-dimensional decomposition does not contain the shear/vorticity eigenvectors. The eigenvectors presented are not unique: several alternate forms appear in the literature. While we discuss a 'Roe-type' scheme of the form in equation (3.11), variants of the dissipative flux such as the Steger-Warming form,

$$-\frac{1}{2}\left\{\left(\mathbb{R}|\Lambda|\mathbb{R}^{-1}\right)_{i+1} U^R - \left(\mathbb{R}|\Lambda|\mathbb{R}^{-1}\right)_i U^L\right\},$$

can be analyzed similarly, with the additional complication that two sets of eigenvectors are used. Note that the left and right states used to form the averages that appear in the matrices above can, in general, be different from the reconstructed left and right states at the cell, U^L and U^R.

3.5 Viscous flux evaluation

Viscous fluxes are computed at the face of a computational cell using the gradients of species mass-fractions, temperature and velocity. These gradients are evaluated at the cell centers using a least-squares fit (suitable for unstructured grids), weighted using inverse distance, as mentioned in Mavriplis [106]. The face-centered gradients are then obtained by interpolating the cell-centered gradients using a deferred correction method [107].

3.6 Time Integration

After the evaluation of inviscid and viscous fluxes, Eq 3.9 needs to be integrated in time. Explicit time integration method is used in this work, which allows to accurately capture the flow dynamics of the unsteady flows simulated here. The third order, strong-stability-preserving explicit Runge-Kutta scheme due to Gottlieb, Shu & Tadmor [95] is used. However, in the case of very stiff chemistry source terms, explicit methods impose prohibitively small time-step requirements. The semi-implicit GRK4A method of Kaps & Rentrop [108] is employed to locally integrate the source terms using the Strang splitting approach [109]. We follow the algorithm mentioned in Ziegler et al. [110] for implementing this method, where chemistry is integrated from t to $t+\Delta t/2$, followed by time advancing the fluxes from t to $t+\Delta t$ and eventually using the updated information to time advance chemistry from $t + \Delta t/2$ to $\Delta t/2$.

For an efficient implementation, in this study, at the first iteration ($t = 0$), chemical source terms are time advanced by $\Delta t/2$. At any later iteration the solution is obtained using two steps: 1) the fluxes are integrated from t to $t + \Delta t$ and then 2) chemical source terms are integrated from $t + \frac{1}{2}\Delta t$ to $t + \frac{3}{2}\Delta t$. Although such a minor change in algorithm avoids calling the expensive source term evaluation multiple times in the same iteration, it requires the simulation to time advance at a constant time-step Δt.

Chapter 4

Validation

4.1 Introduction

In this chapter, the results of the simulations performed to validate the novel fluxes are presented. To understand the numerical issues associated with the presence of steep gradients in species-densities, simulations are performed with increasing levels of complexity. First, a set of one-dimensional simulations are performed with original US3D fluxes (higher-order shock-capturing fluxes) to illustrate the numerical issues. Then, comparison of the performance of the newly developed fluxes and the original are presented. Next, two-dimensional simulations of temporal mixing layers and a shock-density bubble problem are performed. These simulations are followed by three-dimensional simulations of non-reacting and reacting (temporal/spatial) mixing layers. Towards the end of this chapter, validations of the implemented inflow turbulence generation and characteristic boundary conditions required for high fidelity simulations of unsteady reacting flows are presented.

4.2 Active scalar boundedness

4.2.1 One-dimensional advection with equal molar mass and γ.

These basic test cases are meant to test the ability of the method disussed in Chapter 3 to handle sharp jumps in species concentration profiles and to preserve the solution in smooth regions with little or no added dissipation. The two species are N_2 and a

surrogate gas with the same properties, $\mathrm{N}_2^{\mathrm{A}}$. The initial condition has variations only in the species mass fractions; the velocity and all other thermodynamic properties are uniform. We consider two cases. In the first, a sharp top-hat shaped initial mass fraction profile is convected through the (periodic) domain for two periods. The domain spans $-1 \leq x \leq 1$. The second case uses a more complex initial profile that consists of smooth regions interspersed among discontinuities in the species mass fractions:

$$Y_{\mathrm{N}_2} = \begin{cases} 0.1 + 0.4(1 - \tanh(\alpha_1(|x + \beta_1)| + \gamma_1))) & -25 \leq x \leq -5 \\ 0.1 + 0.4(1 - \tanh(\alpha_2(|x + \beta_2)| + \gamma_2))) & -5 < x \leq 0 \\ 0.1 + 0.4(1 - \tanh \alpha_3) + \beta_3 \sin(\gamma_3 x) & 0 < x \leq 14 \\ 0.5 & 14 < x \leq 18 \\ 0.1 & x > 18 \end{cases} \tag{4.1}$$

$$Y_{\mathrm{N}_2^{\mathrm{A}}} = 1 - Y_{\mathrm{N}_2},$$

where $\alpha_i = (5, 0.5, -0.5)$, $\beta_i = (5, 4, 0.05)$ and $\gamma_i = (-10, -5, 2)$. The domain spans $-25 \leq x \leq 25$. The simulation is run for one flow period with a constant time step corresponding to a CFL number of ≈ 0.8 and the Mach number is 1.2. The gradient extrapolation method (section 3.4.1) is used for the central fluxes.

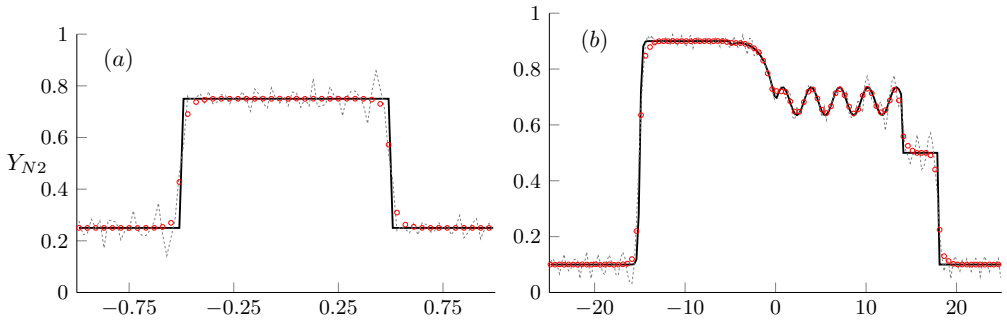

Figure 4.1: (a) Top hat profile convected for two periods. (b) initial profile given by equation (4.1) after one period. Dashed lines: standard shock-capturing fluxes, circles: bounded fluxes.

Figure (4.1a) shows the mass fraction profiles for the first case (symbols): the initial condition (solid line) and a solution using standard fluxes (thin dashed line) are also shown. Note that the local mass fraction bounds are preserved and the sharp initial

profile is reasonably well captured: there is a small diffusive spread around the sharp jumps whose extent compares favorably with results from other high-order schemes in the literature. Fluxes which do not detect and limit sharp jumps in scalar values result in noisy solutions that quickly corrupt the entire domain. Figure (4.1b) shows the mass fraction profiles for the second case. Note that the smooth regions of the profile are represented with very little dissipation and the jumps are captured with no ringing or other spurious oscillations. Solutions that use standard shock capturing fluxes are also shown (dashed lines): these do not use the bounded polynomial reconstruction specified in section 4. Note that oscillations which start at the locations of the discontinuities have polluted the entire solution by this time instant.

4.2.2 One-dimensional material and contact discontinuities

These test cases contain material or contact discontinuities that are advected by an initially uniform velocity field. There are jumps in the initial mass fractions, density and temperature (for contact discontinuities) that are constrained to give a uniform initial pressure. The challenge is to maintain the uniformity of the velocity and pressure (temperature as well, for material discontinuities), and to simultaneously preserve mass fraction bounds as the discontinuities are advected by the nominally uniform velocity field.

Material discontinuities.

The initial conditions are similar to those of Johnsen and Ham [111] and Terashima et al. [103]. The interfaces separate two gases: N_2 and either H_2 or He. The initial conditions are given by

$$(\rho, u, p, \gamma, M) = \begin{cases} (M_{\mathrm{N}_2}/M_{\mathrm{X}}, 1, 1/\gamma_{\mathrm{N}_2}, \gamma_{\mathrm{N}_2}, M_{\mathrm{N}_2}) & \text{if } -0.5 \leq x \leq 0.5 \\ (1, 1, 1/\gamma_{\mathrm{N}_2}, \gamma_{\mathrm{X}}, M_{\mathrm{X}}) & \text{otherwise,} \end{cases}$$

where X is either H_2 or He, with $\gamma_{\mathrm{X}} = (1, 4, 1.66)$ and $M_{\mathrm{X}} = (4, 2)$, respectively. M_{N_2} and γ_{N_2} are 28 and 1.4, respectively. These simulations use 100 uniformly spaced grid points. Figure (4.2) shows profiles of the pressure, density, velocity and Y_{N_2} after one flow time for both cases; the computations use the proposed fluxes. Note that the sharp density of mass fraction jumps are captured cleanly, with no oscillations or excursions. The pressure, temperature and velocity fields are in equilibrium.

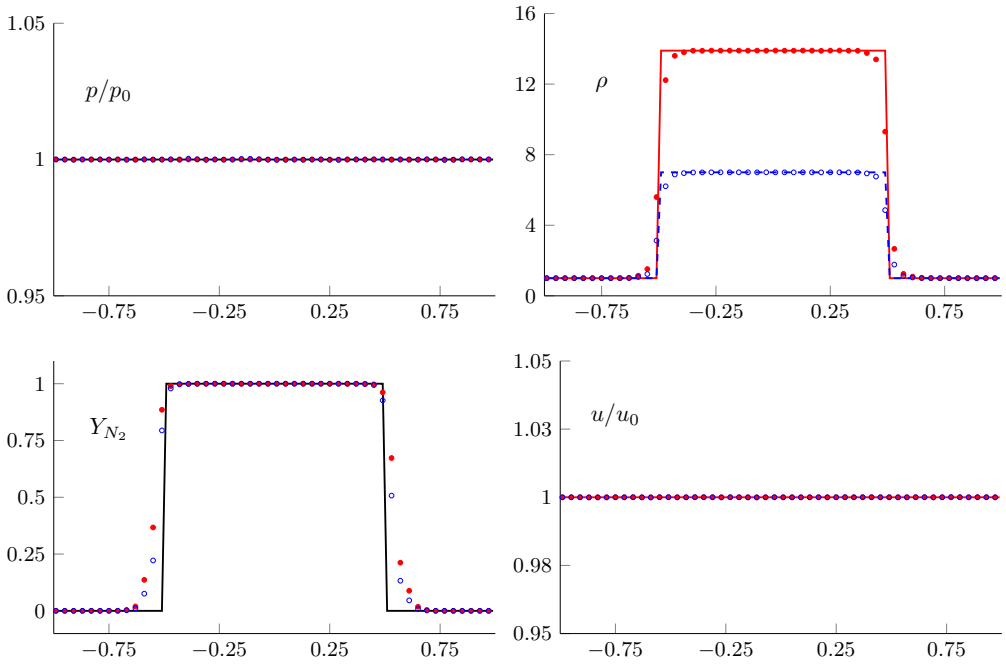

Figure 4.2: Profiles of pressure, density, mass fraction of N_2 and velocity after one flow through time. Solid lines correspond to the initial condition, filled (red) circles: H_2 and unfilled (blue) circles: He.

Contact discontinuities.

The initial conditions for the first set of cases we consider are almost identical to those of the material discontinuity presented above. The only difference is that the density for the region containing N_2 is multiplied by a factor of two: this introduces a jump in the temperature profiles as well.

$$(\rho, u, p, \gamma, M) = \begin{cases} (2M_{\mathrm{N}_2}/M_{\mathrm{X}}, 1, 1/\gamma_{\mathrm{N}_2}, \gamma_{\mathrm{N}_2}, M_{\mathrm{N}_2}) & \text{if } -0.5 \leq x \leq 0.5 \\ (1, 1, 1/\gamma_{\mathrm{N}_2}, \gamma_{\mathrm{X}}, M_{\mathrm{X}}) & \text{otherwise,} \end{cases}$$

Figure (4.3) shows profiles of the pressure, density, velocity and Y_{N_2} after one flow time for both cases; the computations use the proposed fluxes. It is important to note that, although the concentration profiles are bounded, equilibrium of pressure and velocity is not preserved for the case when the ratio of specific heats is different for the two gases.

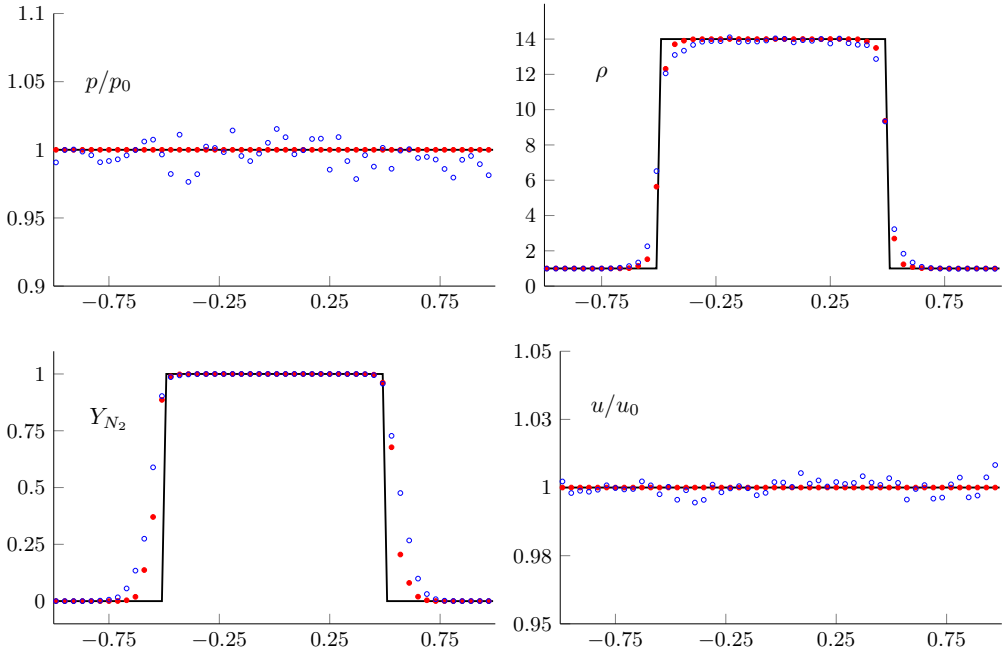

Figure 4.3: Profiles of pressure, density, mass fraction of N_2 and velocity after one flow through time. Solid lines correspond to the initial condition, filled (red) circles: H_2 and unfilled (blue) circles: He.

This is a well known issue and strategies to address this have been proposed in the literature. For instance, Karni [112] proposed a non-conservative primitive algorithm which solves an additional transport equation for γ. Abgrall [113] and, later, Billet and Abgrall [114] formulated the 'double-flux' model to mitigate this issue (the energy is not exactly conserved in the original formulation). These two ideas have been extended further by several researchers. We have experimented with the double-flux model; while it does preserve the expected thermodynamic equilibrium, the energy conservation error was high in our experiments, and we do not use it for the results in this paper: the oscillations in these fields are relatively small (around 3% or lower).

Adapted from the paper by Lv and Ihme [115], the setup for the second case we simulate is similar to that used by Houim and Kuo [116] and Johnsen and Ham [111], except that the initial profiles are smoothed using a hyperbolic tangent function. Note

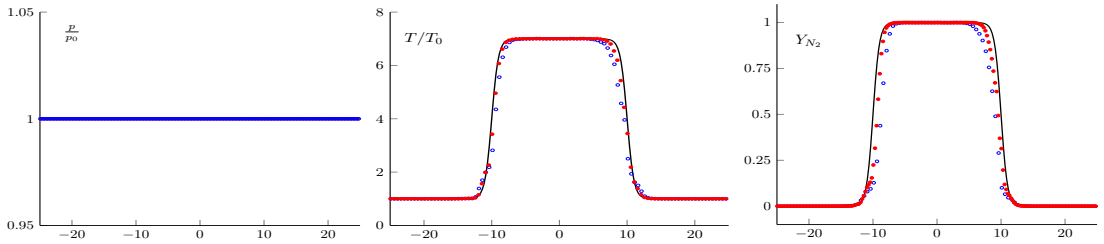

Figure 4.4: Profiles of (a) pressure, (b) temperature and (c) Y_{N_2} after one periodic revolution. Lines: initial condition, filled (red) circles: results using grid spacing $h = 0.125$, open (blue) circles: using $h = 0.25$.

that this represents a smoothed contact discontinuity. The interface separates two species, H_2 and O_2, and the initialization is

$$u = 500\,\mathrm{m/s}, \quad Y_{\mathrm{H}_2} = \frac{1}{2}[1 - \tanh(|x| - \eta)], \quad T = \frac{T_\circ}{2}[(1+\theta) + (1-\theta)\tanh(|x| - \eta)],$$

where $T_\circ$ =300 K, $\theta = 7$, and $\eta = 10$ with $p = 1$ bar. The domain spans $-25 \leq x \leq 25$, and we use either 200 or 400 points. The normalized pressure, temperature and Y_{N_2} profiles after one time-period are shown in figure (4.4). Note that the pressure remains uniform and the mass fractions stay bounded. There is a small but noticeable difference in the levels of diffusion between the two grids: this is a function of the resolution of the initial hyperbolic tangent profile used to prescribe the initial condition.

4.2.3 Two-dimensional mixing layer

In many practical applications, the global maximum and minimum values of species mass fractions are different from the meaningful physical limits: $0 \leq Y_s \leq 1$. In addition, local flow conditions impose localized bounds on scalar values that will be different from globally-defined maxima, irrespective of the actual magnitudes of these maxima. Limiters that use global extremal values explicitly in their definition are not effective, by themselves, in preserving these local bounds. Some flavor of numerical discontinuity detection now becomes a necessary ingredient. The issue then is to preserve low levels of numerical diffusion, since such schemes, based on standard shock capturing methods such as MUSCL or WENO, for e.g., are often severely dissipative. The addition of source

terms due to chemical reactions further complicates the picture.

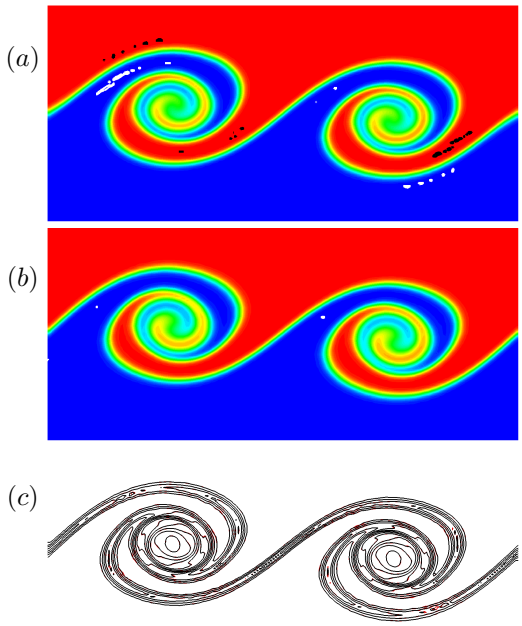

Figure 4.5: (a) and (b): Contours of $Y_{\mathrm{N_2^A}}$ at non-dimensional time $t^* = 40$. (a) Standard low-dissipation fluxes (b) Proposed method. Black and white contours show regions where the mass fractions overshoot the local bounds. (c) Iso-contours of vorticity magnitude at the same time instant; results from proposed method overlaid with results using a single species (pure $\mathrm{N_2}$).

We use a two-dimensional temporally evolving mixing layer to demonstrate that the dissipation in the proposed method is well localized and does not affect the vorticity field. This follows from the structure of the added scalar dissipation which does not change the vorticity eigenvectors. The setup of the velocity and thermodynamic fields is similar to that of Sandham and Yee [117], and we refer to their paper for the full details. The grid size used here is 200×200, with uniform spacing in the x (streamwise) direction and stretching in the y (cross-stream) direction. The stretching used is identical to that in [117]. The convective Mach number is 0.2 and the Reynolds number, defined by the velocity difference between the top and bottom streams, the vorticity thickness and

viscosity based on the freestream temperature, is 1000. The two streams contain a mixture of three nominally identical species: N_2, N_2^A and N_2^B. While these gases have the same physical properties, the numerical method treats these scalars as separate entities; in particular, sharp profiles exist in the species density fields while the total density is overall uniform, initially. The initial mass fractions $(Y_{N_2}, Y_{N_2^A}, Y_{N_2^B})$ are $(0.1, 0.8, 0.1)$ and $(0.1, 0.1, 0.8)$ in the top and bottom streams, respectively, with sharp jumps across the middle of the layer. Figure (4.5a) shows contours of $Y_{N_2^A}$ using a standard low-dissipation scheme (no special limiting or detection used) along with lines showing pockets of the flow where the mass fraction of N_2^A overshoots local bounds (0.8 in the top stream and 0.1 in the bottom stream). The excursions are around 2% in magnitude. Figure (4.5b) is the result obtained with the proposed method - note that the excursions are not zero, but are much diminished in extent and magnitude (around 0.1% in magnitude). Finally figure (4.5c) overlays iso-contours of the vorticity magnitude obtained using the mixture of gases with those obtained from a run with pure N_2. Note that the vorticity is unaffected by the added scalar dissipation.

4.2.4 Shock density-bubble interaction

The experimental study by Haas and Sturtevant [118] on the interaction of shock waves with isolated inhomogeneities provides a useful baseline for testing numerical methods in the context of scalar mixing and boundedness. Here, we use conditions borrowed from their paper to examine the two-dimensional interaction of a Mach 1.22 shock with an isolated cylindrical Helium bubble in air; this particular case has been used by several other researchers ([119], [3], [115]) in a similar context. The early stages of this interaction are dominated by inviscid effects and the results presented neglect diffusive terms. The setup and conditions for this case are similar to those in the papers above. A schematic of the setup is shown in figure (4.6).

The initial diameter of the Helium bubble is $D = 50\,\text{mm}$, and the shock is initially located one diameter upstream of the bubble center. Normal-shock conditions are imposed around the shock location, along with supersonic inflow and outflow boundary conditions at the right and left ends of the domain, respectively. The top and bottom boundaries are treated as symmetry (slip) boundaries. The initial He bubble and surrounding (pre-shock) air densities are 0.2347 and 1.29 kg/m^3, respectively. The initial

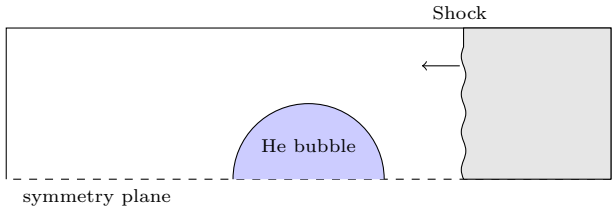

Figure 4.6: Schematic for the shock-bubble interaction problem

pressure in the He and surrounding still air is 1 bar. The grid is cartesian, with spacings $\Delta x = \Delta y = 0.005$D. Density contours at three distinct times are shown in figure (4.7): the top row plots results from the proposed method and the bottom row uses a standard low-dissipation numerical scheme. The flow structure is clean, shows well developed instabilities with no noticeable spurious oscillations, and the resolution compares well with the results of a discontinuous Galerkin scheme used by Lv and Ihme [115]. Note that the scheme without some form of species limiting produces unacceptable levels of noise.

To obtain a quantitative measure of the He bubble development, we plot the x-locations of three points on the interface as a function of time in figure (4.8a). These are in good agreement with previous measurements reported in the literature. One way to quantify the levels of over/undershoots in the course of the simulation is to enforce a hard cutoff on the values of the mass fractions at each new time step - e.g., if Y_{He} goes below zero in a cell, the excursion is truncated. Due to the conservative fluxes used, this hard cutoff will cause the total mass of He to drop. Clearly, this is undesirable. Figure (4.8b) plots the total mass of He for the proposed and unmodified schemes. The mass of He drops by more than 4% for the unmodified scheme. While the total mass of He is not exactly constant for the current method, the net loss is less than 0.02%, which may be acceptable for most simulations of practical interest.

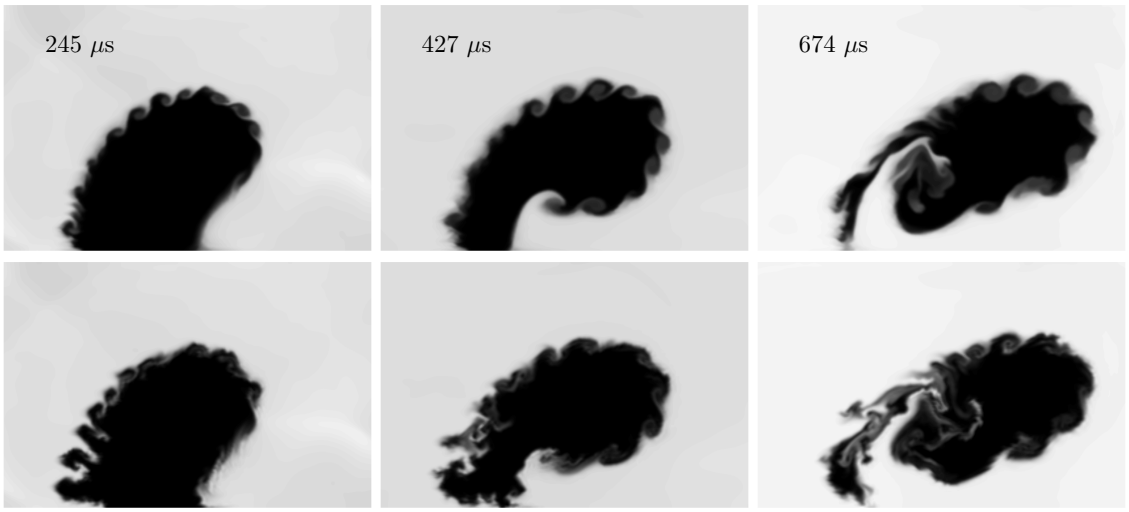

Figure 4.7: Contours of density at three different times in the simulation. Top row: proposed method, bottom row: standard scheme (without bounded polynomial reconstruction.).

4.2.5 Three-dimensional mixing layer

Temporal, non-reacting mixing layer simulations

A three-dimensional temporally evolving mixing layer provides a controlled computational set up to study the evolution of instabilities. The primary objective of the study is to evaluate the levels of undershoots and overshoots in the simulation with a standard shock capturing scheme and the new bounded active scalar fluxes. Further, we aim to understand the temporal evolution of the instability-growth in these mixing layers. We follow the study by Pantano & Sarkar [30] to set up the simulations. The computational domain dimensions are $[0, L_1] \times [-L_2/2, L_2/2] \times [0, L_3]$ in the streamwise (x), transverse (y) and spanwise (z) directions, respectively. Here L_1, L_2, L_3, non-dimensionalized with $\delta_{\omega,0}$, are 74.16, 37.07, 18.53. Initial vorticity thickness, $\delta_{\omega,0}$, is obtained from the initial condition $Re_{\omega,0} = \frac{\overline{\rho}\Delta U \delta_{\omega,0}}{\mu} = 640$. Uniform grid spacing is maintained in the computational domain with 512, 256, 128 points in the streamwise, transverse and spanwise direction respectively. The Reynolds number is calculated using average density and dynamic viscosity of the two streams. A hyperbolic-tangent profile is used to initialize

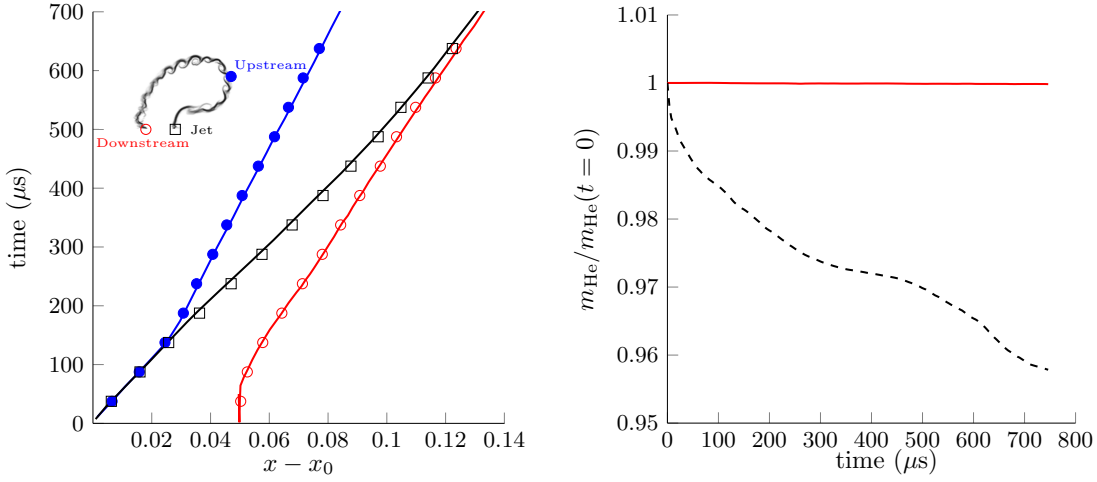

Figure 4.8: (a) Spatio-temporal evolution of three distinct points indicated in the inset. Symbols: current simulation, lines: data from ref. [3]. (b) Total mass of He (normalized) in the domain as a function of time. Solid line: proposed method, dashed line: standard scheme (without bounded polynomial reconstruction.)

the streamwise velocity with equal densities in both streams. Broadband fluctuations are added to the mean velocities to accelerate the transition to turbulence. Isotropic turbulence spectrum of the form

$$E(k) = \left(\frac{k}{k_0}\right)^4 \exp\left[-2\left(\frac{k}{k_0}\right)^2\right] \tag{4.2}$$

with $k_0 = 48$ is used to generate these broadband fluctuations. A sharp discontinuity is imposed in the initial mass-fraction field such that $(Y_{\mathrm{N}_2}, Y_{\mathrm{N}_2^{\mathrm{A}}}, Y_{\mathrm{N}_2^{\mathrm{B}}})$ is $(0.2, 0.6, 0.2)$ for $y > 0$ and $(Y_{\mathrm{N}_2}, Y_{\mathrm{N}_2^{\mathrm{A}}}, Y_{\mathrm{N}_2^{\mathrm{B}}})$ is $(0.2, 0.2, 0.6)$. A reference simulation with pure N_2 is also performed. Support from Mr. Aaron Neville for the simulations in this section is acknowledged. An instantaneous snapshot of the flow field is shown in figure (4.9). Figures (4.10a,b) show the maximum overshoot in the species mass-fractions during the simulation and the growth of the mixing layer as it evolves in time. We note that use of bounded active scalar fluxes reduces the overshoots in the mixing layer without affecting its growth.

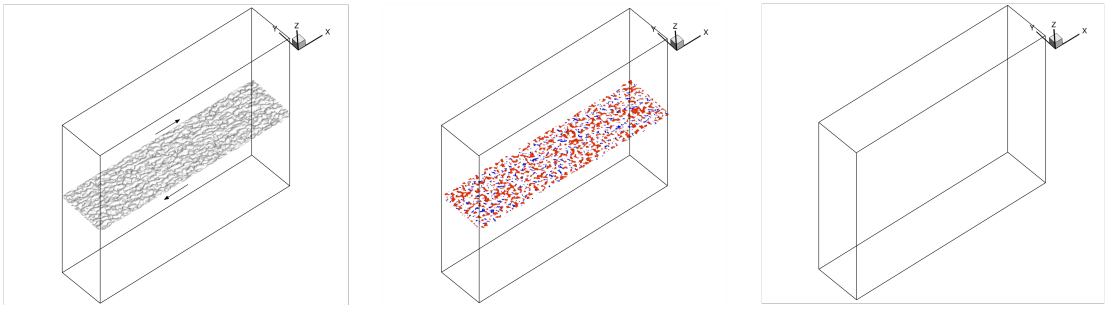

(a) (b) (c)

Figure 4.9: (a) Iso-contours of vorticity magnitude at a non-dimensional time $t^* = 50$ (pure N_2). (b) and (c): show regions where the mass fractions overshoot or undershoot the global bounds of $Y_{N_2^A}$ at the same time instant. (c) Standard low-dissipation fluxes (c) Proposed method.

Spatial, reacting mixing layer simulations

In high Reynolds number reacting flows, turbulence acts to "stir" up parcels of fluid – this results in enhanced gradients of species mass fraction and other transported quantities. For non-premixed combustion problems, especially, the surface area demarcating reactants is also greatly increased by the action of turbulence. Concurrently, of course, molecular diffusion acts to "mix" the fluid at a molecular level. Physically, the rate of mixing is set by the molecular diffusion coefficients and by the gradients in the flow. In practice, numerical and sub-grid diffusion also play a strong (often dominant) role in the simulated mixing process. A major goal of this paper is to suggest low numerical diffusion schemes for these problems, which should help mitigate the effect of numerical diffusivity. Note that this issue is coupled to the problem of species boundedness (both global and local bounds are to be respected): non-dissipative schemes without some form of artificial viscosity produce oscillatory mass fraction profiles which can result in aphysical results. On the other hand, too much added diffusion results in mixing that is too rapid. Clearly, a balance between the two is desirable. The role of sub-grid diffusion from particular turbulence models is outside the scope of this work here: it could be argued that the imposed sub-grid diffusion should be aware of the diffusion associated with the numerical method (this is the basis for implicit large eddy simulation methods).

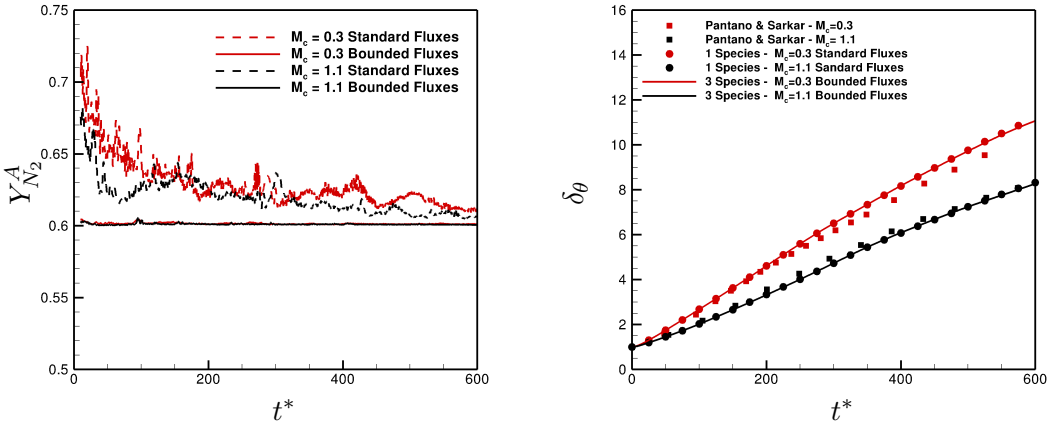

Figure 4.10: *a*) Comparison of evolution of maximum value of $Y_{N_2^A}$ in the domain at two different convective Mach numbers and *b*) Comparison of growth rate of the mixing layers with a single and multiple-species in the simulation.

The final test case is a simulation of a reacting mixing layer using LES. The conditions corresponding to the experiments of Slessor, Bond and Dimotakis [4]. The high Damköhler number in this flow (Da $\gg$ 1, typical of "mixing-limited" reacting flows) implies that the temperature rise due to chemical reactions is a close surrogate for the amount of mixing. Consequently, errors in mass fraction boundedness show up as (often egregious) errors in the temperature field. The dominant, hypergolic, reaction in this flow is between trace amounts of non-premixed H_2 and F_2, present in the primary and secondary streams respectively. Details of the computational set up, the composition of the species (Case 1) and the reaction mechanism is mentioned in Chapter 5, in the context of studying the physics of reacting mixing layers.

Figure (4.11) shows visualizations of the flow field. The left figure plots isosurfaces of the Q-criterion [120]: this is frequently used to indicate regions of the flow with high swirl. Note that the top stream contains an inert gas, Ar, whose mass fraction, Y_{Ar}, should in theory be strictly bounded by the initial and boundary conditions imposed. Additionally, the adiabatic temperature rise also has a maximum value ΔT_{ad} that is easily estimated using the top and bottom stream compositions. Regions in the flow

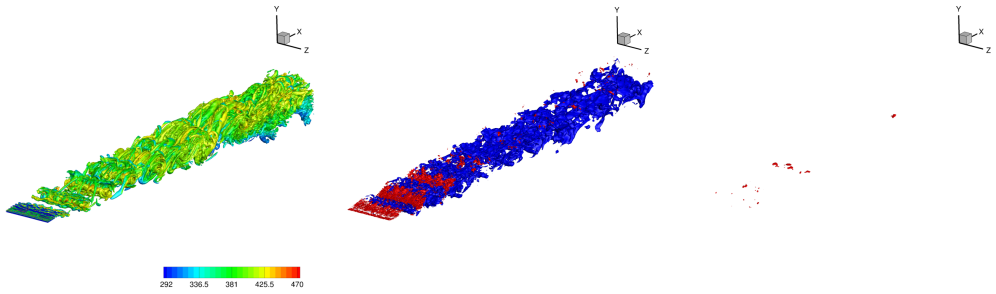

Figure 4.11: *(left)* Isosurface of Q-criterion colored by temperature. *(mid)* Isosurfaces of Ar mass fraction excursions (red) and temperature excursions (blue) (unmodified flux scheme).*(right)* Isosurfaces of Ar mass fraction excursions (red) and temperature excursions (blue) (proposed fluxes)

field where Y_{Ar} and ΔT_{ad} exceed their bounds beyond a small threshold are shown in figures (4.11(mid,right)) for the unmodified and proposed fluxes, respectively (red isosurfaces correspond to Y_{Ar} and blue isosurfaces correspond to temperature rise). The threshold for the temperature rise is 3° K, which is within the error bounds of the experiment. Note that the proposed fluxes produce usable, well bounded results (it is not exact, however - this is possible only under an extreme time-step restriction which makes the solution impractically expensive).

In the experiment, velocity and temperature measurements are made using probes located 36 cm downstream of the trailing edge of the splitter plate. We compare our results with this data in figure (4.12). It is important to note that due to slight variations in the initial development of the mixing layer, it is difficult to get an exact match for these quantities. The velocity profiles using the unmodified and proposed fluxes both agree reasonably well with experimental data. The temperature field, however, is extremely sensitive to excursions in species mass fractions for this flow - the proposed fluxes produce a temperature profile that is dramatically better than the unmodified fluxes - this can clearly be seen in figure (4.12(b)).

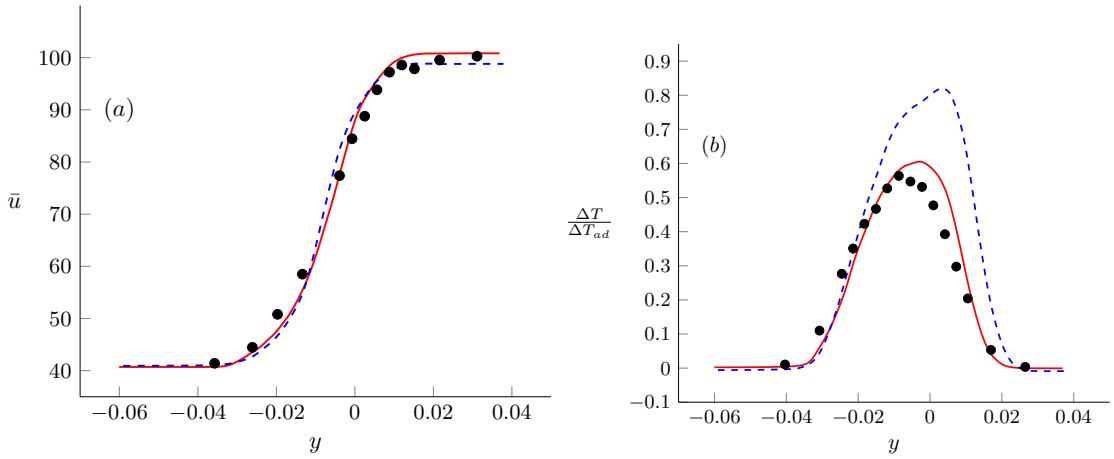

Figure 4.12: (a) Mean velocity profile at 0.36 m from splitter plate tip. (b) Mean temperature profile at the same location. Symbols – experimental data from [4]; solid line – proposed fluxes; dashed line – unmodified fluxes.

4.3 Inflow turbulence generation

While active scalar boundedness is important for reacting flows, to obtain results predictive of experiments it is also important to apply realistic turbulence at the inflow boundaries. To validate the implementation of inflow turbulence, simulations of fully-developed turbulent boundary layers over a zero pressure-gradient flat plate is performed. The conditions used for these simulations are given in Table 4.1, following the work of Souverein et al. [121]. The work presented in this section was an extensive collaboration with Dr. Jeffrey Komives, whose technical support made this simulation possible. Here, digitally filtered inflow turbulence is generated based on a RANS profile and is allowed to spatially and temporally develop. The initial conditions for these simulations were obtained from a priori two-dimensional RANS simulations using SA Catris model for turbulence closure and freestream conditions as mentioned in Table 4.1. Simulations with coarse near wall grid-spacing are performed with wall modeling developed by Komives [122].

The computational domain dimensions, normalized with the boundary layer thickness (δ_{99}), are 50×10×4 in the streamwise (x), transverse (y) and spanwise (z) directions, respectively. Uniform grid spacing is maintained in the streamwise and spanwise

Re_θ	M_e	δ_{99} (mm)	θ (mm)	U_e (m/s)
$5,000$	2.3	11.0	0.96	550.0

Table 4.1: Flow conditions of LES validation

directions by using 24 and 37 grid elements within the boundary layer. Three grids were used in the simulation with y_1^+ of 0.5, 2.0 and 10.0 for resolved, medium and coarse grid respectively. The grids were progressively coarsened at 5% growth rate till a height of $5\delta_{99}$, beyond which the growth rate was set to 20%. Supersonic inflow and outflow boundary conditions were imposed in the streamwise direction, while periodic boundary conditions were imposed in the spanwise direction. The far-field grid stretching in the transverse direction aids the reduction of reflections from the boundaries by introducing numerical dissipation. The Vreman turbulence model was used for closure and the simulation was time advanced using third-order RK3 scheme [95].

4.3.1 Generated fluctuations at the inflow plane

Inflow turbulence generated using digital filter based technique, mentioned in Chapter 2, is added to the RANS boundary layer profile to generate time varying inflow. The generated synthetic fluctuations should reproduce the Reynolds-stress and the appropriate integral length scales representative of turbulent boundary layers. Integral length scales and Reynolds stresses as a function of wall-normal distance is prescribed to achieve this objective. Two general philosophies exist in the literature as to the most appropriate way to prescribe integral length scales at the inflow. The first uses a constant length scale throughout the boundary layer, while the second method varies the length scale (at different zones) based on distance to the wall. Here, we use the latter.

First, we analyze the generated fluctuations at the inflow plane of the simulation by checking if it adheres to the prescribed correlations. An instance of the fluctuating velocity field at the inflow is shown in this figure (4.15) to give a qualitative idea of the fluctuating field at the inflow plane. Figure (4.13) shows a good match of the generated two-point correlation (computed as $R_{uu} = \frac{\langle u(x_i)u(x_i+r)\rangle}{\langle u(x_i)^2\rangle}$) in the spanwise and transverse directions at several heights in the inflow boundary layer. Also, the Reynolds stresses as a function of distance from the wall is seen to match well with the prescribed values in figure (4.14). Although these results are encouraging, their evolution and behavior

in a full three-dimensional simulation must be evaluated.The following sections discuss the evolution of the inflow turbulence in a supersonic flat plate boundary layer.

4.3.2 Evolution of inflow turbulence

The flow is allowed to convect through the domain for nearly five convective flow times ($\tau_c = \delta_{99}/U_e$). This allows for the startup transience to wash away. Statistics in the flow are computed beyond this time for nearly ten convective flow times. Volume statistics are collected for flow primitives and Reynolds stresses. These are then averaged in the spanwise direction. Surface statistics are collected as well for wall temperature, pressure, and shear.

Instantaneous visualization of the flow field is shown in figure (4.16) with Q-criterion, colored with instantaneous streamwise velocity in the inset. The temperature contours and the wall shear stress plotted in the figure qualitatively describe the spatial development of the compressible turbulent boundary layer.

Velocity profile

Figure (4.17a) shows the span-averaged mean velocity distribution at several streamwise stations. The velocity profile (u^+) is van Driest transformed to allow for comparison to the classic incompressible law of the wall, given as

$$u^+ = \frac{1}{\kappa} \log y^+ + C \tag{4.3}$$

where κ and C traditionally assume the values of 0.41 and 5.1 respectively. The simulations studied here produce the expected log-region with slightly different of value the log-law constant. These values are slightly above or below the value of 5.1, similar to the experimental measurements of Souverien [121]. They are offset from one another due to differences in mean wall shear.

Skin friction

The computed skin friction coefficient, $C_f = \tau_w / \frac{1}{2}\rho U_e^2$ is compared to the power-law fit by White [123]. The predicted skin friction (with wall-model) is seen to match

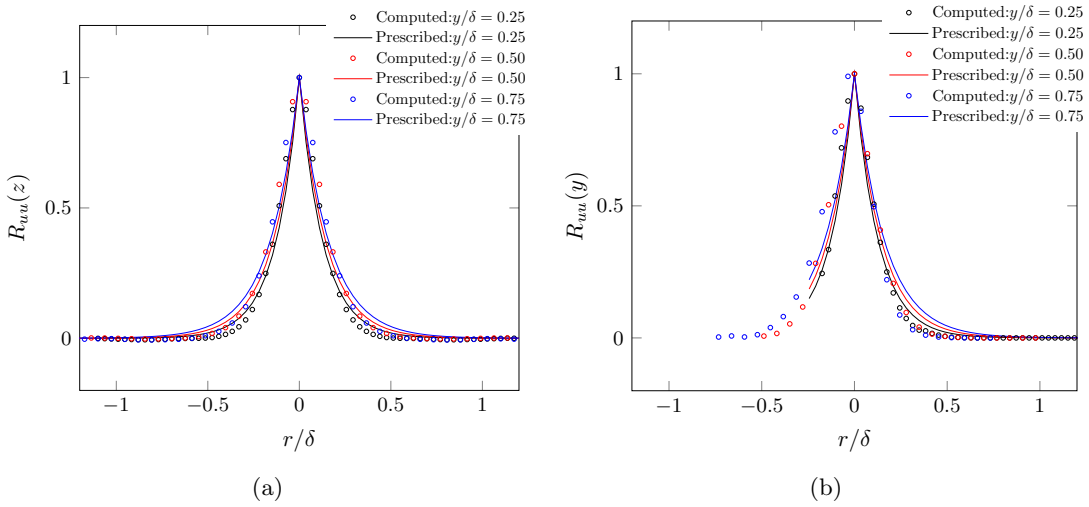

Figure 4.13: Comparison of computed and prescribed two-point correlation in the (a) spanwise and (b) transverse direction.

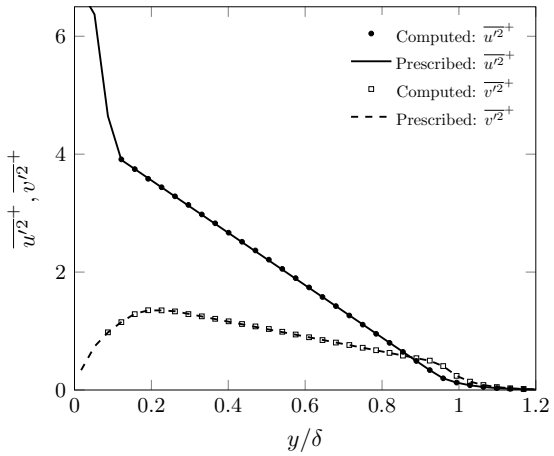

Figure 4.14: Comparison of computed and prescribed Reynolds stresses at the inflow plane. Here $\overline{u'^2}^+$, $\overline{v'^2}^+$ are $\overline{u'^2}/u_\tau^2$ and $\overline{v'^2}/u_\tau^2$ respectively.

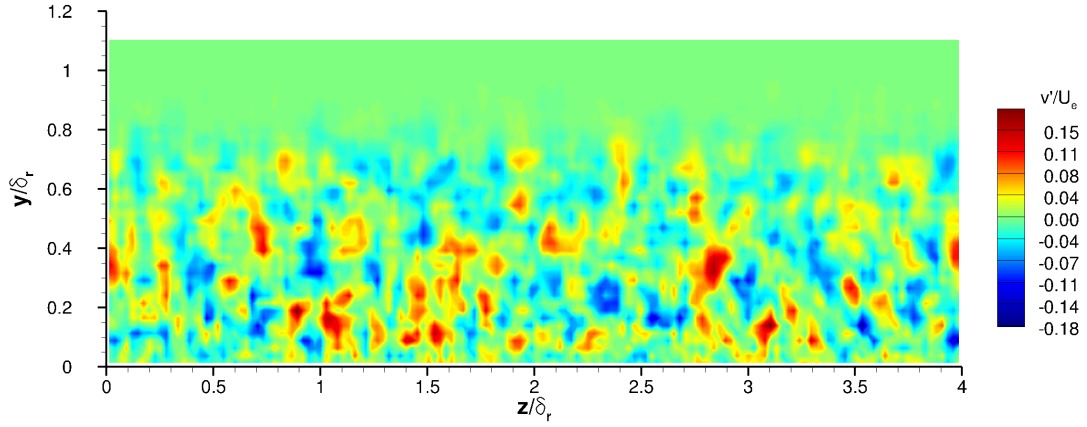

Figure 4.15: An instantaneous fluctuating velocity field generated at the inflow plane.

the fit by White within 5% error. Usually, the synthetic turbulence introduced at the inflow requires about 20 boundary layer thicknesses to develop into 'realistic' turbulence. Within this initial establishment region the skin-friction is seen to be suppressed in figure (4.17). Beyond this region, the simulated skin friction coefficient nearly follows the trend described by the one-sixth power law given by $C_f = 0.020 Re_\delta^{-1/6}$.

While the wall model results on both coarse and medium meshes are accurate when compared to the fit by White, they do not produce identical results. This is largely because of the insufficient resolution within the viscous sub-layer. The rationale behind these variations are discussed at length in Komives [122]. Additionally, the possibility of the finer grids allowing for the introduction of resolved fine-scale energetic structures near the wall cannot be ignored.

Favre averaged stresses

Obtaining the correct Reynolds stress gives credence to the nature of the turbulent structures developing in the simulation. In the simulations, Reynolds stress profiles collapse beyond the streamwise location of $x/\delta = 15$, indicating that the synthetically generated turbulence has evolved into a self-similar state. This nature can be seen shown in figure (4.17c). There is exceptional agreement between the averaged Reynolds normal stresses and the profile by Degraff and Eaton [78] and resonable agreement with

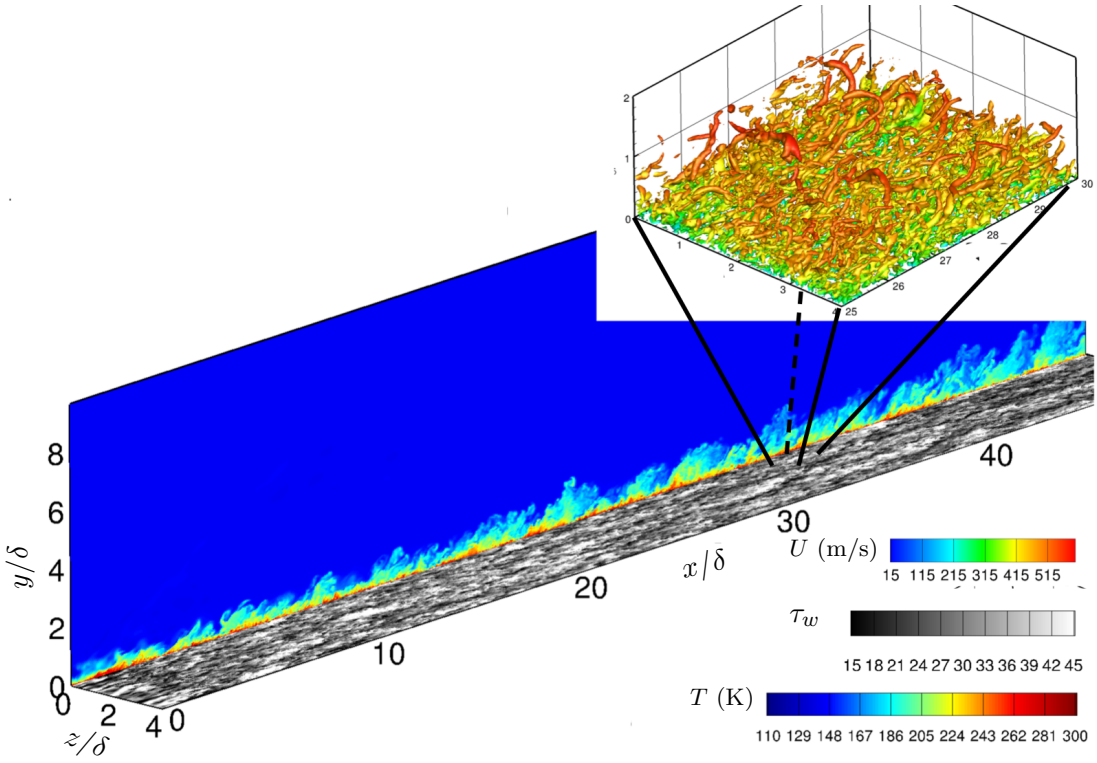

Figure 4.16: Instantaneous visualization of the flow field: vertical plane shows the contours of temperature, horizontal plane shows contours of wall shear stress and the inset shows the zoomed in view of the Q-criterion, colored by local velocity, at a downstream location on the flat plate.

the experimental measurements by Souverein [121]. Computed values of $\overline{u''u''}$ agrees better than the measurement of $\overline{v''v''}$, similar to the disagreement observed by Kawai and Larsson [124] when simulating the $Re_\theta = 50,000$ experiments by Souverein.

4.4 Subsonic boundary conditions

Accurate simulations of subsonic flows relies on good subsonic boundary conditions. The issue of spurious reflections at the boundaries for a subsonic flow is well known and few of the methods to mitigate them are discussed in Chapter 2. Here, validation of the implemented characteristic based boundary conditions is presented. A single vortex convection simulations are performed with conditions mentioned in Granet et al. [44].

The streamwise and the transverse velocities are initialized using the streamfunction

$$\psi(x,y) = \Gamma e^{\frac{(x-x_c)^2+(y-y_c)^2}{2R_c^2}} \tag{4.4}$$

where the vortex strength is represented by Γ, the coordinates of the vortex center are (x_c,y_c), R_c is the radius of the vortex and $U_{max} = \frac{\Gamma}{R_c\sqrt{e}}$. Streamwise velocity and transverse velocities are obtained as $u = \frac{\partial\psi(x,y)}{\partial y}$ and $v = -\frac{\partial\psi(x,y)}{\partial x}$ respectively. The pressure in the domain at the start of the simulation is prescribed as

$$p - p_\infty = \frac{\rho\Gamma^2}{2R_c^2} e^{\frac{(x-x_c)^2+(y-y_c)^2}{R_c^2}}. \tag{4.5}$$

Two cases of vortex convection are presented here. While Case A is set up with $\Gamma = 0.11$ and $U_{max}/U_0 = 0.5$, Case B is set up with $\Gamma = 0.022$ and $U_{max}/U_0 = 1$ with $M_\infty = 0.28$. Convecting these vortices out through the subsonic boundary with minimum distortions and spurious reflections would be the desired behavior when modeled boundary conditions are used. This is demonstrated in figures (4.18 and 4.19), where the convecting vortex very nearly retains it shape as it exits the domain and the pressure reflections, inferred from the normalized pressure, defined as

$$p^*(x,t^*) = \frac{p(x,t^*) - p_\infty}{p(0,0) - p_\infty}, \tag{4.6}$$

with $t^* = 2U_0t/L$, in the domain are at acceptable levels. The domain for these simulations are set up with a domain length of $L = 0.013$m and $R_c = 0.1L$.

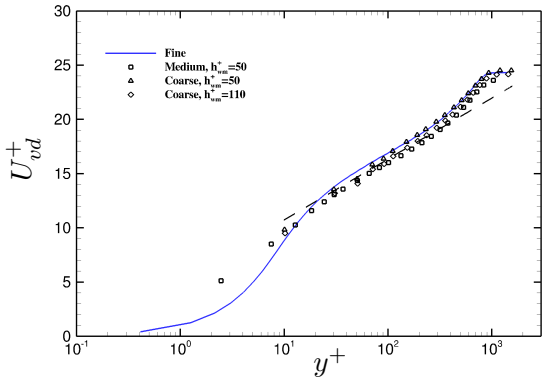

(a)

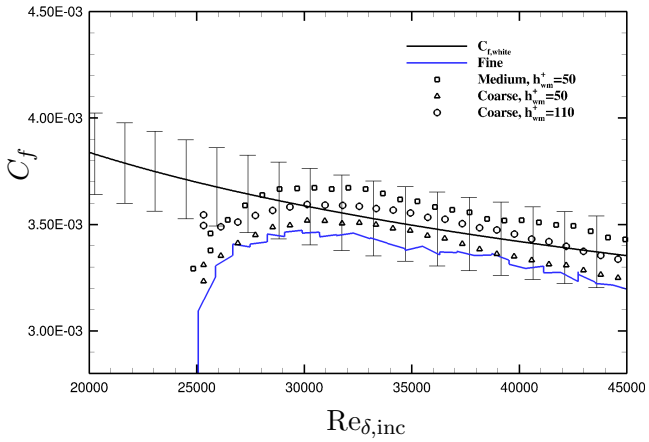

(b)

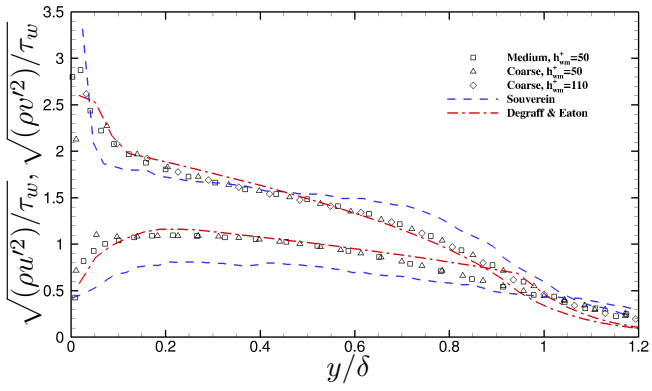

(c)

Figure 4.17: Comparison of (a) van Driest transformed velocity profiles, (b) computed skin friction coefficient and (c) turbulent stresses on three grid resolutions.

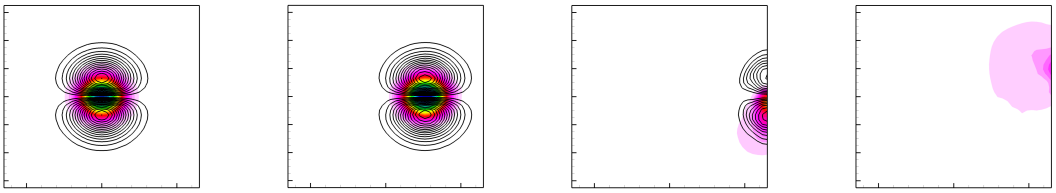

(a) $t^* = 0$ (b) $t^* = 45$ (c) $t^* = 112$ (d) $t^* = 143$

Figure 4.18: Comparison of streamwise velocity (black lines) and pressure contours at multiple instances for Case A. (p^*_{max}, p^*_{min}) for at these instances are $(0.99, 0)$, $(1.02, -0.03)$, $(0.51, -0.25)$ and $(0.16, -0.11)$ for (a), (b), (c) and (d) respectively.

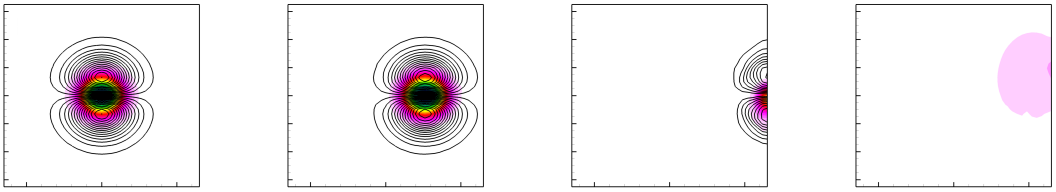

(a) $t^* = 0$ (b) $t^* = 45$ (c) $t^* = 112$ (d) $t^* = 143$

Figure 4.19: Comparison of streamwise velocity (black lines) and pressure contours at multiple instances for Case B. (p^*_{max}, p^*_{min}) for at these instances are $(0.99, 0)$, $(1.05, -0.01)$, $(0.51, -0.15)$ and $(0.08, -0.05)$ for (a), (b), (c) and (d) respectively.

4.5 Summary

In this chapter, we presented several examples to demonstrate the performance of numerical methods and models that have been implemented for this study. We show that the new method developed to ensure boundedness of active scalars mitigates dispersive errors significantly, resulting in reliable solutions. Along with this method, good boundary conditions and initial conditions are necessary to replicate experimental observations. These were also tested and presented in this chapter. These numerical methods are now used to investigate practical flow configurations in the following chapters.

Chapter 5

Reacting and non-reacting mixing layers

5.1 Introduction

In this chapter, we study reacting and non-reacting mixing layers using the newly developed numerical method presented and validated in the previous chapters. First, we provide a detailed review of experimental and computational studies on mixing layers. Then, we study spatially evolving reacting subsonic mixing layers following the experimental work of Slessor et al. [1] at the California Institute of Technology. We present our analysis and conclude with some discussions.

5.1.1 Review of mixing layers

Small disturbances perturb the shear between the two parallel streams of fluids, initiating a Kelvin-Helmholtz type instability. In the process, fluids from either sides of the mixing layer are brought into the mixed region redistributing species, momentum and energy. The presence of mean shear provides a continuous supply of energy to the mixing layer, sustaining its growth. A mixing layer typically features vortices of several length scales which evolve alongside the dominant spanwise roller-like structures.

Mixing in these eddies is visualized as a three stage Lagrangian process as explained in detail by Dimotakis [125]. In the first stage, the large scale motions bring fluid

into the mixing region. Fluid elements in the neighborhood of the vorticity-bearing fluid feels the induced velocity (Biot-Savart) and is set into motion kinematically (not through diffusive processes). The fluids thus entering the mixing region are irrotational. Then, this low wavenumber motion gives way to smaller spatial scale processes through viscous action, inducing vorticity to the fluid element. Later, in the third stage, diffusive processes mix the fluids at a molecular level. It is in this stage the reactants, carried by the fluids (if any), undergo chemical reactions leading to product formation and heat release. Experimental and computational studies for more than half a century are credited for this understanding (and more) of physical processes in a mixing layer and the factors influencing it. In the following paragraphs, we review this previous work.

Initially, mixing layer experiments focussed on studying the large scale structures in the flow. Investigations by Winant & Browand [7], Brown & Roshko [8], Roshko [9], Dimotakis & Brown [10] and Hernan & Jimenez [11] identified the large-spanwise vortical structures in the mixing layers. These studies also discussed the role of the coherent spanwise structures in the growth and mixing process. Subsequently, observations made by Konrad [12], Breidenthal [13], Hernan & Jimenez [11], Luis Bernal [126], Bernal & Roshko [14] and Liepmann & Gharib [15] showed the role of turbulent entrainment in the growth of individual vortex structures. Studies by Bernal [14, 126] noticed small-scale vortex structures which were associated with the secondary streamwise structures. They were presented as wrapped-vortex like structures in the flow. These structures not only introduce three-dimensionality in the mixing layers, but are also responsible for increased entrainment in the flow and are the primary mechanism that introduces mixing transition (the region beyond $\mathrm{Re} \approx 10^4$, where the mixing layer is observed to have increased mixing, larger interfacial areas, and several physical aspects being nearly independent of the Reynolds number [127]). The secondary structures become a part of the spanwise vortices through the process of amalgamation, redistributing the local three-dimensionality. This process is a precursor to mixing transition that occurs as a result of several such amalgamation processes, suggested to happen at local $\mathrm{Re} > 10^4$ [14, 128].

Simultaneously, analyzing the growth rate of mixing layers (typically linear in the absence of mean streamwise-pressure gradient) and understanding the factors influencing it became a subject of investigation. The growth rate was observed to be strongly

dependent on density and velocity ratios of the two streams that formed the mixing layer. The trends showed that the growth rate was inversely related to the velocity ratio and proportional to the density ratio [8, 12, 129] (ratio of velocity and density of slower stream to the faster stream). However, at low values of density ratio, the opposite behavior was observed in a few experiments [130]. Thereafter, experiments were conducted to understand the effects of compressibility on mixing layer growth. The organized quasi two-dimensional flow structures observed in incompressible flows were seen to be replaced by less organized three-dimensional structures in the flow at high convective Mach numbers ($M_c > 0.6$) by Clemens & Mungal [16], Messersmith & Dutton [131], Samimy, Reeder & Elliott [17], Elliott et al. [18], and Bonnet et al. [132]. Experiments by Bradshaw [133], Papamoschou & Roshko [134], Hall et al. [130], Clemens & Paul [22], and Samimy et al. [17] noted reduced growth in compresible mixing layers, and Elliot & Samimy [135] and Goebel & Dutton [136] reported reduced turbulence intensities and Reynolds stresses in the flow.

Studies on mixing at the smallest scales in the mixing layer were explored by employing passive scalars and chemical reactions with low heat-release. Experiments with chemical reactions alleviated the issues of poor resolution and were instrumental in revealing the probable composition of the mixing layer and the efficiency of mixing. Koochesfahani et al. [19] showed that the entrainment of the fluids into the mixing layer is asymmetric in favor of the chemical species present in the high-speed stream, and hence the composition. Koochesfahani & Dimotakis [20] showed how the composition of the mixing layer changes during initial roll-up and transition. Work by Clemens & Mungal [21], Clemens & Paul [22], and Island [23] indicated that the probability distribution function of the mixed fluid composition becomes increasingly marching (where the most probable composition varies along the transverse extend of the mixing layer) with increase in compressibility, demonstrating the increased role of smaller structures in the flow field. However, the studies on efficiency of mixing reported results that were at variance: Dutton et al. [137] found higher mixed fraction at higher compressible Mach numbers, Clemens & Paul [22] found only a small variation and Hall et al. [130] observed lower fraction of mixed fluid at higher compressible Mach numbers. While investigations of chemically reacting mixing layers by Breidenthal [13] gave insights to the structure of three-dimensional mixing layer, a study by Mungal & Dimotakis [129]

revealed the existence of hot structures and tongues of cold fluid, and that the temperatures in the mixing layers were well below the adiabatic flame temperature. Studies on mixing layers with chemical reactions by Hermanson & Dimotakis [138] and Hall [139], showed reduced growth rate in mixing layers with heat release and attributed this to reduction in the turbulent shear stress due to reduction in density owing to heat release. An extensive review of factors influencing the physics of mixing layers was documented by Dimotakis [32].

The inflow condition has been found to be one of the most critical parameters in determining the growth of the mixing layers. Experiments by Bradshaw [140] and Chandrsuda et al. [141] observed that the state of the boundary layers forming the mixing layer has a pronounced effect on the mixing layer, typically extending to over thousands of incoming boundary layer momentum thickness downstream of the splitter plate, altering the structures in the mixing layer and its the growth rate. Work by Bell & Mehta [142] and Goebel et al. [143] also found that the turbulence properties of the mixing layer formed from laminar and turbulent incoming boundary layers are significantly different. These findings were supported by Slessor et al. [1] who showed that the state of the incoming boundary layer alters the entrainment process and molecular mixing using chemically reacting mixing layers.

Progress in understanding the physics of mixing layers was also strongly aided by numerical simulations. Availability of large computational resources and advances in numerical methods helped to corroborate empirical observations and shed light on information that were otherwise not feasible to measure in the experiments. Direct Numerical Simulations (DNS) were performed by Moser & Rogers [24] and Rogers & Moser [25] to study the mechanisms responsible for the onset of transition to turbulence, the role of pairing in the growth of three-dimensionality, and self-similar evolution of incompressible mixing layers. The DNS of compressible temporal mixing layers were studied by Sandham & Reynolds [26] and Luo & Sandham [27], and found considerable changes in the flow structures (disappearance of strong two-dimensionality of the shear layer observed at low Mach numbers) with increase in compressibility, which hints at a very different mixing process at higher convective Mach numbers. A study of the effects of compressibility, in a spatially evolving mixing layer by Fu & Li [144] using a simplified BGK gas-kinetic scheme showed that compressibility affects large scale structures

more than the small scale ones, and that the shocklets are formed due to slow moving lumps of fluid entering into high-speed flow. Further, direct simulations of Sarkar [28] and Freund et al. [29] confirmed the reduced growth rate in mixing layers at higher compressible Mach numbers which were reported earlier by experimentalists. Although there were speculations about the role of dilatation in the reduced growth-rate in mixing layers, simulations by Sarkar [28] showed that the growth rate reduction was due to a large decrease in normalized Reynolds stresses and pressure-strain terms. Later, LES of Vreman et al. [145] confirmed this observation. A study by Pantano & Sarkar [30] showed that the delay in transmission of pressure-strain signals due to finite speed of sound in compressible flow, along with the increased decorrelation so introduced, leads to the decrease in the pressure-strain terms. Stability analysis also brought to light significant insights and understanding about mechanisms in a mixing layer. Linear and parabolizied stability analysis [146,147] revealed the significance of density ratio, vortex pairing and the role of instability modes in the flow in determining mixing efficiency.

The effect of heat release on mixing layers is another aspect that was widely investigated by studying temporal simulations. McMurtry et al. [148], in their direct simulations of mixing layers with moderate heat release found that the development of large-scale structures in the mixing layer is slowed down, and the entrainment of reactants is reduced resulting in decreased overall chemical product formation rate. They also point to an important role of baroclinic torque that could have in increased mixing at the edges of the large-scale structures in high heat-release cases. The decrease in product formation was also observed in the simulations of Miller et al. [149] which compared results using the steady laminar diffusion flamelet model (SLDFM) and the conditional moment method. They not only find the heat release delays the onset of pairing and transition in the mixing layers, but also observe shocklets in the flow above $M_c = 1.25$. Pantano et al. [31] studied the influence of heat release on the scalar field and found that the average scalar dissipation conditioned on the scalar depends strongly on the value of the scalar, informing model development. Further, they also mention that due to the strong coupling of density and scalar fields, the nature of the scalar pdfs change with heat release. They also point to the role of decreased density and mixing to decrease in the cross-stream profile width and reaction rates. Jaberi et

al. [150] simulated chemically reacting mixing layers using filtered mass density function methodology and found close agreement with experimental data. More recently, Mahle [151] performed DNS of temporal reacting mixing layers and reported a similar reduction in Reynolds stresses, turbulent kinetic energy, and their close relation to the pressure-strain correlations with increasing in compressibility. Also, with an increase in compressibility, a reduction in scalar fluctuations in the mixing layer and reduction in the extent of penetration of the pure streams into the mixing layer through probability density functions was reported.

Although temporal reacting mixing layers were studied extensively, only a sparse body of literature is available on spatially evolving reacting mixing layers. An obvious choice for preliminary spatially evolving mixing layer simulations, accounting for computational costs, is a two-dimensional geometrical setup (with a single computational cell in the spanwise direction). The results from such simulations give a qualitative picture of the flow, the behavior of numerical methods, models, and boundary conditions. But, they cannot capture key features, like vortex stretching and the streamwise vortices in the flow, which are responsible for increased entrainment into the mixing layers and leading to three-dimensionality of the flow [14]. A physically realistic simulation of the mixing layer therefore should be three-dimensional with sufficient spanwise domain length and resolution [152]. Further, beyond the region of mixing transition, $\mathrm{Re} \approx 10^4$, the mixing layer is observed to have increased mixing, larger interfacial areas and several physical aspects being nearly independent of the Reynolds number [127]. In order to capture this, the simulations are required to have a large domain in the streamwise direction.

Several non-reacting and reacting spatially-evolving mixing layer simulation studies have been performed [153, 154]. However, only very few studies have focussed on three-dimensional chemically reacting, spatially-evolving mixing layers, due to the huge computational requirements [155, 156]. More recently, Ferrer et al. [156, 157] presented DNS of high speed reacting mixing layers at $\mathrm{Re}_\omega \approx 10^4$. Subsonic, spatially evolving mixing layers, well beyond the mixing transition ($\mathrm{Re} > 10^5$), was simulated by Ferrero et al. [158] and Ferrero [159] using finite rate chemistry and filtered mass density functions (FMDF), respectively. While the particle-based FMDF method showed a good match with experimental observations, several numerical challenges (issues of dispersive errors

and sub-grid scale chemistry turbulence models) were brought to light in the detailed finite-rate chemistry study. In this thesis, we continue the investigation of spatially-evolving, subsonic, reacting mixing layers using a detailed finite-rate chemistry model to address few numerical challenges and investigate the effect of inflow conditions.

5.2 Computational domain and setup

Figure (5.1) shows a sketch of the experimental facility: the portion of the domain used in the computation is shown by the dotted red rectangle. The geometry is extended upstream of the subsonic injection to ensure that the initialization remains away from the dynamics inside the test section, maintaining a clean inflow. This region also provides sufficient length for synthetically generated inflow turbulence to evolve into realistic turbulence (nearly 20δ).

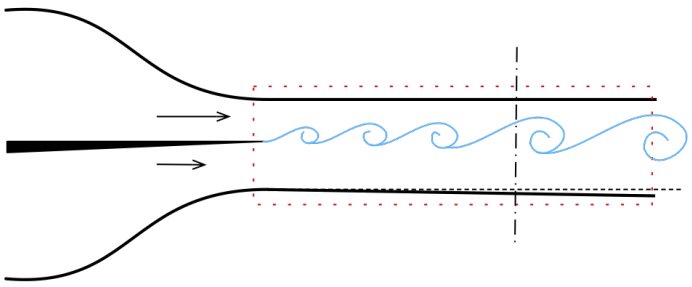

Figure 5.1: Cartoon of the experimental test section.

Views of the computational grid are shown in figure (5.2). The grid used has approximately 10 million cells in total. The computational domain dimensions are [-0.034, 0.77] $\times$ [-0.06, 0.04] $\times$ [0, 0.06] meters in the streamwise (x), transverse (y) and spanwise (z) directions, respectively. The lower guide-wall of the test-section is inclined at a small angle, $\beta = 0.01$ rad, to the horizontal. The top surface of the splitter plate is at $y = 0$. Refined regions of the grid approximate the spread of the mixing layer, as determined by preliminary simulations; it is much finer in the shear layer region with 15 uniformly spaced cells to resolve the incoming boundary layer thickness, δ, and is rapidly coarsened away from the edges of the shear layer. The finite thickness of the

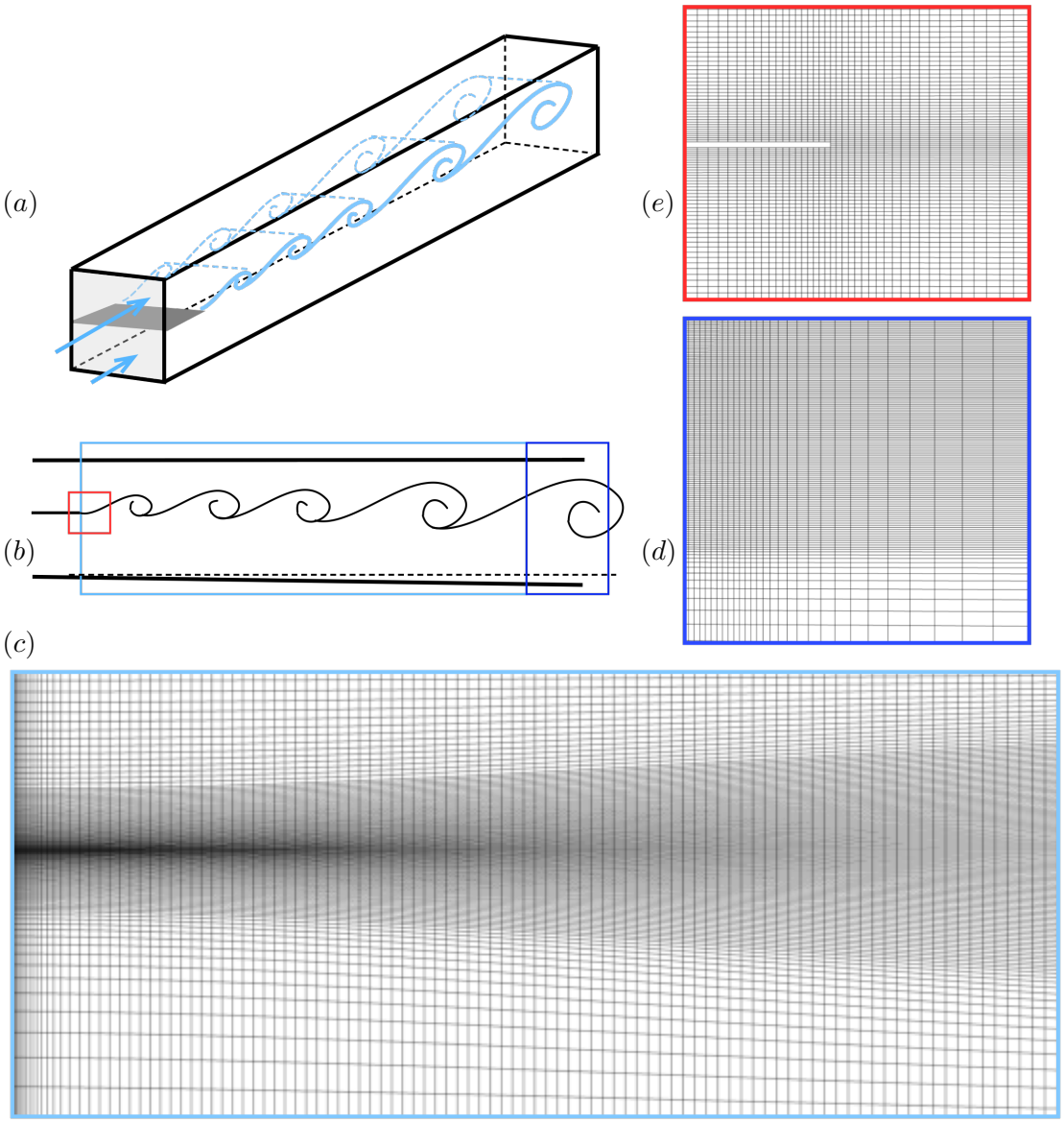

Figure 5.2: A qualitative view of the computational grid used in the simulation. A cartoon of the mixing layer is shown in (a) and several regions in the computational grid are marked in (b). The image in (c) gives a general idea of the density of the grid in the streamwise plane. Grid stretching beyond the domain of interest is shown in (d) and the resolution near the splitter plate is shown in (e).

splitter plate tip (0.13 mm) is coarsely resolved: three grid cells span this thickness. The grid is progressively stretched in the streamwise direction beyond $x = 50\,\text{cm}$ (the splitter plate tip is located at $x = 0\,\text{cm}$) and reactions are frozen beyond this point to facilitate the handling of the subsonic boundary condition at the outflow (discussed below).

5.3 Initial conditions

The simulations use the flow conditions from the experiments [1] and are shown in Table 1. As mentioned earlier, the top stream contains a small amount of H_2 and NO (fuel and catalyst), while a fraction of the bottom stream is F_2 (oxidizer). The ratio of oxidizer to fuel is

$$\phi = \frac{[F_2]}{[H_2] + \frac{[NO]}{2}},$$

where [X] = moles of X. We also study the "flip" experiment, with the ratio of oxidizer to fuel as $1/\phi$, performed by Slessor et al. [1] to highlight the differences due to asymmetric entrainment.

The velocity in the domain is initialized with a hyperbolic tangent function. A Blasius profile with the momentum thickness of the experiments ($\theta = 0.11\,\text{mm}$ for the top stream and $\theta = 0.17\,\text{mm}$ for the bottom stream) is used as the inlet velocity profile for simulations with laminar inflow. To get a mean flow profile for the simulation with turbulent inflow, we perform a RANS calculation of a flat plate boundary layer. A numerical trip is placed at the location where the laminar boundary layer has a momentum thickness of 0.095 mm to match the flow conditions just before the trip as described in Slessor et al. [1] Dimensions of the numerical trip match the dimension of the trip wire (0.8 mm diameter) used in the experiments. For simulations with inflow turbulence, we use the digital filter technique of Klein et al. [160], with modifications suggested by Xie & Castro [75], as implemented in Touber & Sandham [74]. With this method, inflow perturbations are generated to match the prescribed Reynolds stresses and two-point correlations. These fluctuating quantities are added to the mean flow and imposed at the inflow plane of the computational domain.

The simulations performed correspond to a low convective Mach number ($M_c = 0.2$), high Damköhler number ($Da > 1.0$) and large Reynolds number ($Re = \frac{\Delta U \delta_T}{\bar{\nu}} \approx 2 \times 10^5$)

Table 5.1: Summary of the flow conditions chosen for the present work. Flow conditions closely match the experiments of Slessor et al. [1]

Run	Chemical Composition (mole fractions)		ϕ
	Primary stream	Secondary stream	
Case 1	$H_2 = 0.93\%$, NO $= 0.14\%$,	$F_2 = 8.00\%$, $N_2 = 76.0\%$,	8
(F_2 rich)	Ar $= 8.00\%$, He $= 15.07\%$,	He $= 16.0\%$.	
$\Delta T_{ad} = 171$ K	$N_2 = 75.86\%$.		
	$U_1 = 100\,\mathrm{m/s}$, $\rho_1 = 1.03\,\mathrm{kg/m^3}$	$U_2 = 40\,\mathrm{m/s}$, $\rho_2 = 1.04\,\mathrm{kg/m^3}$	
	$T_1 = 292$ K	$T_2 = 292$ K	
Case 2	$H_2 = 12.00\%$, NO $= 0.75\%$,	$F_2 = 1.55\%$, $N_2 = 76.00\%$,	1/8
(H_2 rich)	Ar $= 8.00\%$, He $= 4.00\%$,	Ar $= 6.45\%$,He $= 16.00\%$.	
$\Delta T_{ad} = 267$ K	$N_2 = 75.25\%$.		
	$U_1 = 100\,\mathrm{m/s}$, $\rho_1 = 1.03\,\mathrm{kg/m^3}$	$U_2 = 40\,\mathrm{m/s}$, $\rho_2 = 1.04\,\mathrm{kg/m^3}$	
	$T_1 = 292$ K	$T_2 = 292$ K	

flow with a density ratio (ρ_R/ρ_1) of ≈ 1. The Reynolds number is based on the velocity difference ($\Delta U = U_1 - U_R$), temperature rise thickness for the chemically reacting flow (δ_T), and the average kinematic viscosity of the two streams ($\overline{\nu}$). Here, the convective velocity is computed using the formula

$$U_c = \frac{a_2 U_1 + a_1 U_2}{a_2 + a_1},$$

where a_1, a_2 are the speeds of sound and U_1 and U_2 are velocities of the top and the bottom streams respectively. The chemical compositions of the two streams and the state of the gas are mentioned in in Table 5.3.

5.3.1 Boundary conditions

Characteristic-based subsonic boundary conditions are prescribed at the inlet for both the streams. In the experiments, beyond the test section, the flow expands into a large duct and is neutralized before it is exhausted to the atmosphere [161]. In the simulation, towards the far end of the computational domain, chemistry is deactivated, and subsonic outflow boundary conditions (Poinsot and Lele [50], extended to handle

multiple species by Yoo and Im [162]) are prescribed. Beyond the streamwise location of $x = 0.5\,\mathrm{m}$, numerical dissipation was progressively added as a function of streamwise distance to ensure that the flow exits at the prescribed pressure with minimal numerical reflections at the outflow. Slip-wall boundary conditions are prescribed at the top and the bottom walls of the test section and periodic boundary conditions are prescribed in the spanwise direction.

5.3.2 Reaction mechanism

The chemical reactions we are concerned with are between molecular hydrogen and fluorine. However, a more realistic reaction mechanism is composed of the hydrogen-fluorine chain reaction initiated by nitric oxide (catalyst):

$$\mathrm{NO} + \mathrm{F_2} \overset{k_1}{\rightleftharpoons} \mathrm{NOF} + \mathrm{F}, \qquad \Delta Q = -76.6 \ \ \mathrm{kJ/mole}, \qquad k_1 = 4.2\times10^8 \ \exp\left(\frac{-1150}{T}\right), \tag{5.1}$$

$$\mathrm{H_2} + \mathrm{F} \overset{k_2}{\rightleftharpoons} \mathrm{HF} + \mathrm{H}, \qquad \Delta Q = -133.9 \ \ \mathrm{kJ/mole}, \qquad k_2 = 2.6\times10^9\, T^{0.5} \exp\left(\frac{-307}{T}\right), \tag{5.2}$$

$$\mathrm{F_2} + \mathrm{H} \overset{k_3}{\rightleftharpoons} \mathrm{HF} + \mathrm{F}, \qquad \Delta Q = -411.3 \ \ \mathrm{kJ/mole}, \qquad k_3 = 3.0\times10^6\, T^{1.5} \exp\left(\frac{-845.5}{T}\right). \tag{5.3}$$

Although additional reactions for the formation of NOF and dissociation of $\mathrm{F_2}$ could be considered [5], they are ignored due to the much larger computational cost involved: in previous work by Ferrero et al. [158], a validation of the chemistry model was presented and it was shown that using the reaction set Eq. (5.1-5.3) is adequate.

5.4 Results

Simulations are initially run for at least one convective flow time, during which the initial transients are convected out of the domain. The convective-flow through time is calculated based on the length of the test section and the secondary stream velocity. Following which, statistics are then collected for over four eddy turn-over times, calculated based on the size of the largest eddy and convective velocity (U_c). The collected

flow quantities are then averaged in the statistically homogeneous (spanwise) direction. These flow quantities from the simulations are then compared with the experimental data at the measuring station: $x = 0.365\,\mathrm{m}$ for laminar inflow, and $x = 0.41\,\mathrm{m}$ for turbulent inflow conditions. In both cases, the simulations use a constant physical time step of $6.5 \times 10^{-8}\,\mathrm{s}$, corresponding to a CFL ≈ 0.7. The simulations were run on a cluster consisting of 24-core 64-bit AMD Opteron CPUs connected with an Infiniband interconnect using 960 cores. These simulation took nearly 60 hours for one convective flow time, and nearly 30 hours collecting statistics for each case.

5.4.1 Validation of the chemistry model

A well-stirred zero-dimensional simulation was performed to compare the simulation results with the data in Mungal and Frieler [5]. The result from such a simulation validates the reaction mechanism and can be used to check the adiabatic flame temperature rise for the mixture of species used in the three-dimensional simulations. The code for the validation uses the chemistry routines from the solver, the chemical source terms are active, the routine solves the energy equation, and for the chemical species over time starting from a well-defined set of initial conditions.

Figure (5.3a) shows the evolution of temperature for an initial concentration of 4% H_2 and 0.5% F_2 and 0.015% NO in an N_2 diluent. The maximum heat released in the system, which determines the adiabatic flame temperature rise, ΔT_{ad}, is a function only of the initial concentrations of F_2 and H_2. In the simulations performed in this work, the reduced reaction system, Eqs. (5.1-5.3), were used. The curves closely reproduce those obtained by Mungal and Frieler [5] using the CHEMKIN software. Also, in figure (5.3b), the temperature rise profiles for the chemically reacting cases considered in the present simulation are shown. The maximum temperature rise (ΔT_{ad}) matches the reported value of adiabatic flame temperature for this composition in Slessor et al. [1]. Furthermore, these simulations help to determine the value of a stable time step for 3-D simulations that use explicit time integration schemes. Although explicit time stepping is used for simulations with Case-1 composition, semi-implicit chemistry is employed for simulations with Case-2 composition considering stiffer chemistry inferred from figure (5.3b).

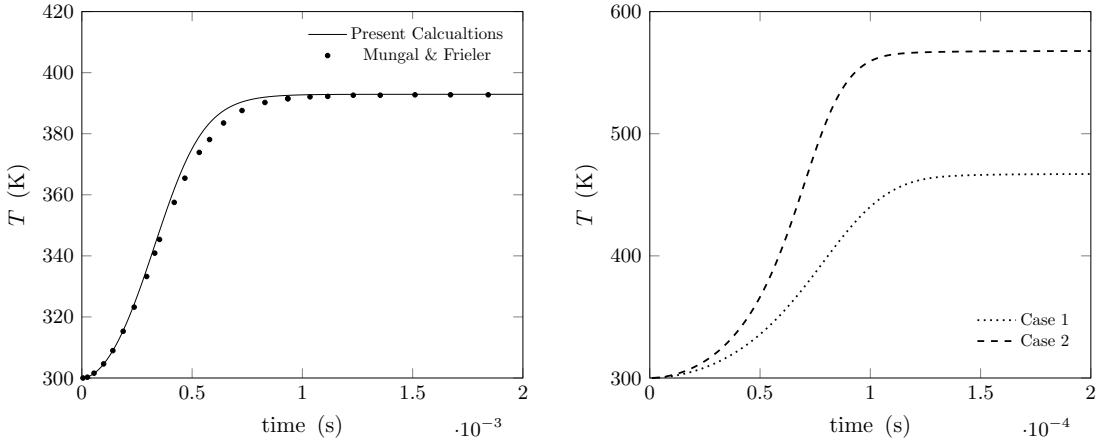

(a) (b)

Figure 5.3: Temperature evolution for 4% H_2 and 0.5% F_2 and 0.015% NO in an N_2 diluent are shown in the plot on the left. Solid lines are for the reduced reaction set, Eqs. (5.1-5.3). Circles were obtained by Mungal and Frieler [5] using the software CHEMKIN. $\Delta T_{ad} = 93K$ for this case. The temperature rise profiles for the chemically reacting Cases (1 & 2), considered for the present study, are shown on the right.

5.4.2 Reacting and non-reacting flow simulations

We perform chemically reacting large-eddy simulations with laminar and turbulent inflow conditions with compositions given in Table 1. Further, to get an idea of differences in the flow field due to reactions, we perform non-reacting simulations with the same compositions, but with frozen chemistry. We analyze the simulation data starting with a qualitative analysis of the flow field. Following which, we compare the simulation data with experimental measurements and present a few observations.

Flow visualization: Schlieren Images

Contours of the density gradient magnitude from the simulations and corresponding Schlieren images from Bond [6] (an experimental study with similar flow conditions as Slessor et al. [1]) are compared to understand the qualitative behavior of the flow field. While figure (5.4a) shows visualization from the non-reacting simulations, figure (5.4b) shows the comparison for the reacting case (Case-1) with laminar inflow conditions. Red lines are overlaid on the Schlieren images from the experiment to mark the extent of the shear layer in the experiment and to give a guide of the visual growth rate. Blue lines are overlaid on the results from the simulation for the same purpose. We observe that the flow fields look qualitatively similar and also that the two colored lines in figure (5.4a,b) nearly match each other (a perfect match between the experiments and the simulation data would be surprising as these images are a snapshot from a particular instant during the flow). These images indicate a reasonable agreement of the growth rate, the extent of the mixing layer and vortex spacings (qualitatively), giving an encouraging possibility that the simulations could correctly represent the entrainment rates.

Flow visualization: Q-criterion

Figure (5.5) compares the isosurfaces of the Q-criterion for the reacting and the non-reacting flows. Here, Q is the second invariant of the velocity gradient tensor and is colored using the local value of Ar mass fraction (a species initially present only in the top stream). Figure (5.5a) shows dominant spanwise rollers residing alongside streamwise 'rib vortices' in the braid region for the non-reacting simulation with laminar inflow

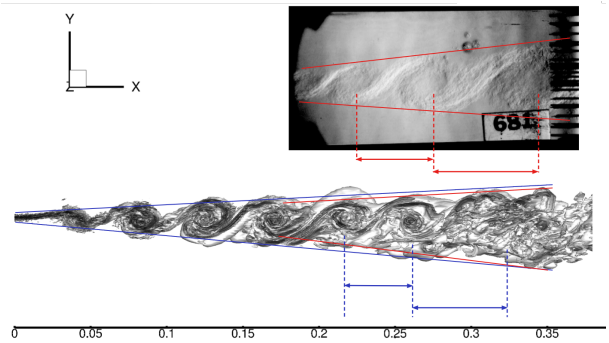

(a) non-reacting flow

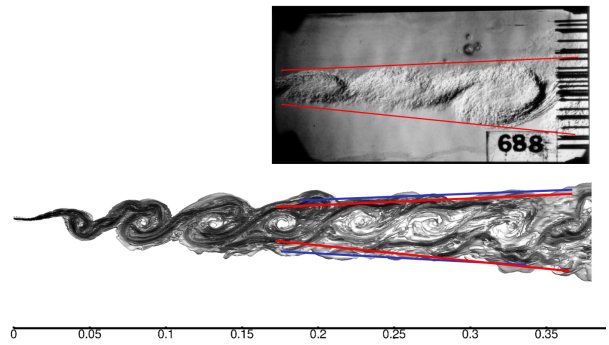

(b) reacting flow

Figure 5.4: Comparison of the Schlieren images (top) from the experiments [6] and the density gradient magnitudes from the corresponding computed flow fields.

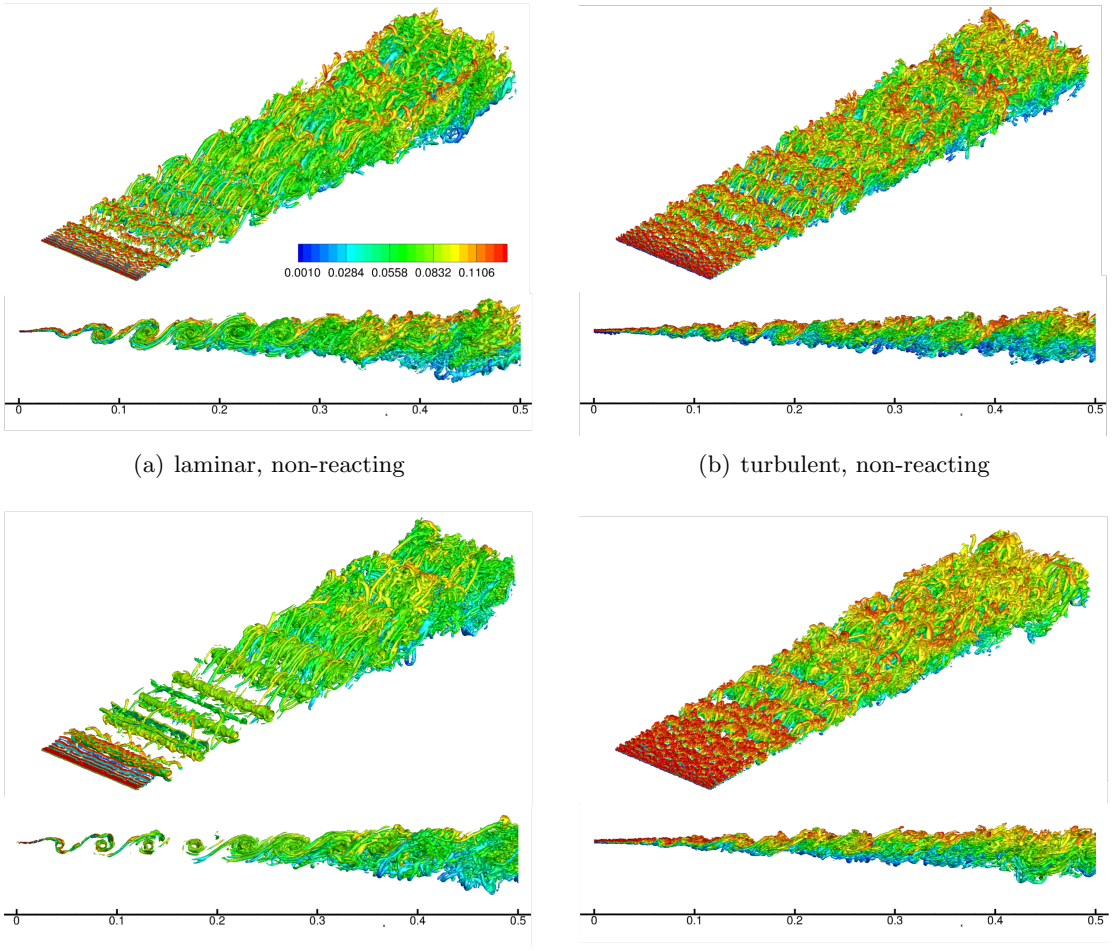

(a) laminar, non-reacting

(b) turbulent, non-reacting

(c) laminar, reacting

(d) turbulent, non-reacting

Figure 5.5: Angled three-dimensional view, and side views of an isosurface of the Q-criterion colored with Ar mass fractions (top-stream species).

condition. Further, we see that the mixing layer begins to show increased vorticity beyond the 4^{th} dominant roller, suggesting transition in the flow. Far downstream it is very clear that the mixing layer has transitioned to a fully-turbulent state. On the other hand, inflow turbulence is seen to impede the formation of large distinguishable spanwise rollers in figure (5.5b). Although the spanwise vortices are noticeable, they exist alongside several small scale vortices. This image also points to increased vorticity from very early stages of the mixing layer. This is consistent with the empirical observations of Pickett and Ghandhi [163], who studied low speed incompressible mixing layers at the same velocity ratio. Interestingly, for the reacting mixing layer with laminar inflow, figure (5.5c), the mixing layer seems to develop dominant spanwise vortices much later compared to the non-reacting case, before quickly transitioning into a state of increased vorticity. Figure (5.5d) shows a small decrease in the spanwise roller size compared to the corresponding non-reacting case in figure (5.5b) due to the presence of heat release. But otherwise, they qualitatively retain the similar trend as the non-reacting case.

Because the Q-isosurfaces, in figure (5.5), are colored with mass fractions of Ar (species present only in the primary-stream), they give a picture of the composition in the mixing layers. The mixing layers with laminar inflow are seen to predominantly have green color, which corresponds to about half of the maximum value of the Ar mass fraction in the flow ($Y_{\text{Ar}}^{max} = 0.1273$, use contour legend for reference). This is an indicator that the mixing layers have a preferred composition. However, far downstream we observe a slight departure from this trend. Turbulent mixing layers, on the other hand, are seen to have varying compositions along the transverse direction. These trends in the species composition can be better understood using the probability density functions presented below.

Probability density functions

"Numerical probes" were placed in the test section to collect statistics at three x locations ($x = 20\,\text{cm}$, $30\,\text{cm}$ and $40\,\text{cm}$). In each of these planes, the probes are placed at several locations along the height of the test section and across the spanwise direction. The data collected were used to calculate the mixture fraction, ξ, which is defined as the mole fraction of high-speed stream fluid [20,32]. With this definition, $\xi = 0$ corresponds to pure low-speed-stream fluid, $\xi = 1$ represents pure top-stream fluid, and any values

in between represent the fraction of top-stream fluid. Based on the probe data it is possible to build a probability density function, $\mathscr{P}(\xi; y)$, of the mixture fraction at each transverse location.

Figures (5.6 and 5.7) show the probability of finding mixed fluid across the height of the test section at a particular streamwise location. In the freestream region of the top stream, the amount of mixing is almost zero ($\xi = 1$). Hence, the plots are expected to have a peak in the probability near $\xi = 1$. Similarly, for pure bottom stream fluid, $\xi = 0$. As one traverses through the mixing layer from the top of the test section, one would expect a transition from $\xi = 1$ to $\xi = 0$. Figures (5.6a-c, 5.7a-c) show the probability density function for non-reacting and reacting simulations with laminar inflow conditions. Although the PDFs show peak values of 1 and 0 in the top and bottom stream locations, they show a distinguishable peak in the shear layer too, centered about a value closer to 0.65. These non-marching PDFs (where the most probable composition is independent of the location along the transverse extent of the mixing layer) give a hint that the mixing layer tends to have a preferred composition, indicating that the large-scale motions in the flow have effectively mixed the two streams.

However, far downstream there is an indication of the non-marching PDFs changing their nature, as seen in figure (5.6c and 5.7c). Slessor et al. [1] also infer a non-marching behavior from the symmetric temperature rise profile observed in their experiment with laminar inflow conditions. Non-marching PDFs were also observed in the work of Picket & Ghandhi [163], who were studying the effect of inflow conditions in low-speed mixing layers. The present observations also agree with the observations made by Konrad [12] and Koochesfahani & Dimotakis [20]. Such non-marching PDFs can be linked to the presence of large spanwise vortices in the flow and a relatively uniform composition across the transverse direction, as shown in figures (5.5a-d).

Figures (5.6d-f and 5.7d-f) show PDFs of non-reacting and reacting mixing layers with turbulent inflow. These marching PDFs are strikingly different from those with laminar inflow conditions, indicating differences in the nature of entrainment with changes in inflow conditions. The marching PDFs not only support that species composition varies along the transverse direction, it also hints at an asymmetrical temperature profile for chemically reacting simulations. Slessor et al. [1] arrived at the same conclusion from the temperature rise profiles using different compositions in the two streams.

Pickett and Ghandhi [163], however, observe hybrid PDFs for their mixing layers with turbulent inflow. For the reacting flow simulations, figures (5.7a-f), the PDFs look similar to the corresponding non-reacting flow, showing that heat release and chemical reactions, for the cases in this study, introduce only negligible changes in the local chemical compositions.

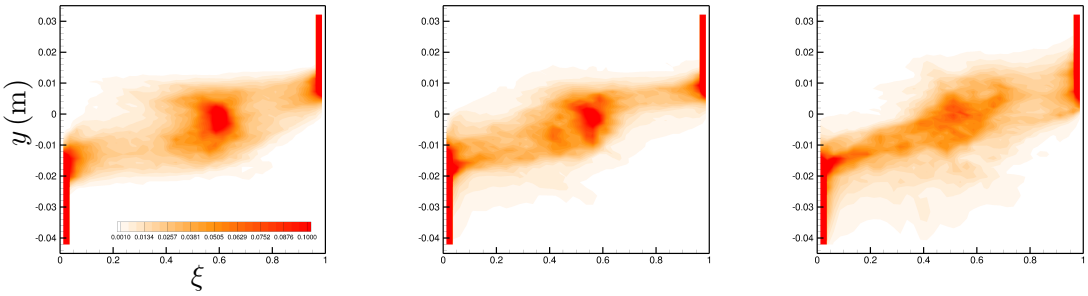

(a) $x = 20.0\,\text{cm}$ (b) $x = 30.0\,\text{cm}$ (c) $x = 40.0\,\text{cm}$

(d) $x = 20.0\,\text{cm}$ (e) $x = 30.0\,\text{cm}$ (f) $x = 40.0\,\text{cm}$

Figure 5.6: The probability density functions for the non-reacting flow simulations with laminar (top) and turbulent (bottom) inflow conditions.

Velocity profiles

Figure (5.8) compares velocity profiles in the simulations with that in the experiment at the experimental measuring stations. The velocity profiles from the simulations are seen to closely follow the measured value of velocity in the experiment, as shown in figures (5.8a). This figure shows that the extent of the mixing layer is similar to that seen

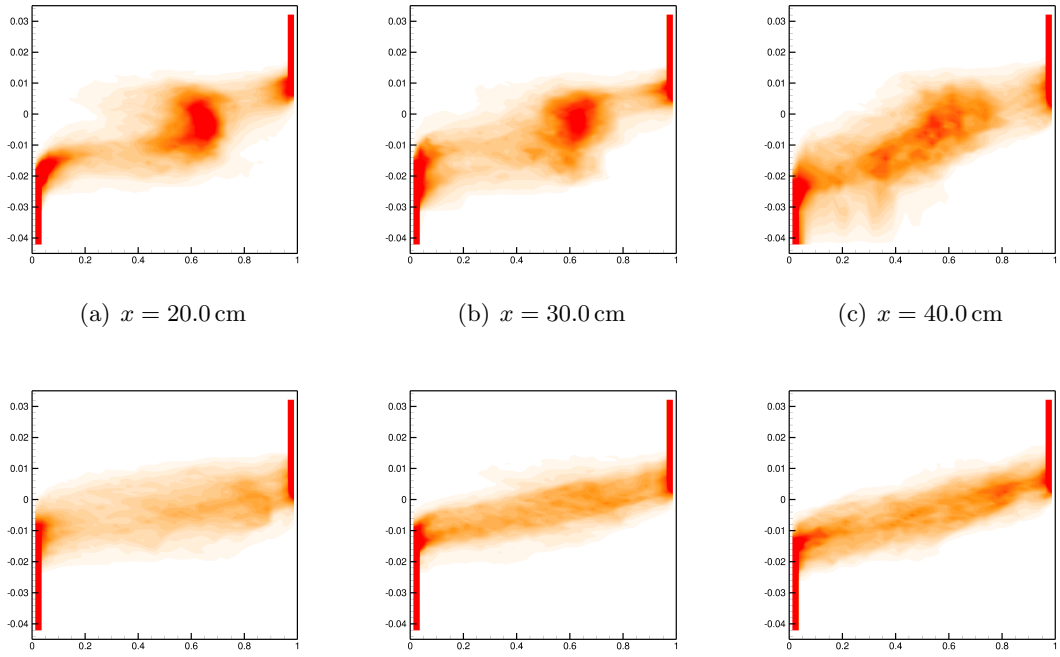

(a) $x = 20.0\,\text{cm}$ (b) $x = 30.0\,\text{cm}$ (c) $x = 40.0\,\text{cm}$

(d) $x = 20.0\,\text{cm}$ (e) $x = 30.0\,\text{cm}$ (f) $x = 40.0\,\text{cm}$

Figure 5.7: The probability density functions for the reacting flow simulations with laminar (top) and turbulent (bottom) inflow conditions.

in the experiments at the measurement location. In the same figure, we also observe that there is no appreciable difference between the velocity profiles of the reacting and non-reacting cases. Next, we compare the same data in non-dimensionalized coordinates, as studied in Slessor et al. [1], and observe that these profiles nearly collapse, as shown in figure (5.8b). These observations indicate that inflow conditions and heat-release effects have only a weak effect on mean velocity profiles at the measurement locations. Alternatively, we can comment that differences in mixing and entrainment induced by changes in inflow conditions and chemical compositions, show negligible influence on the mean streamwise velocity profiles, consistent with the observations made by Slessor et al. [1].

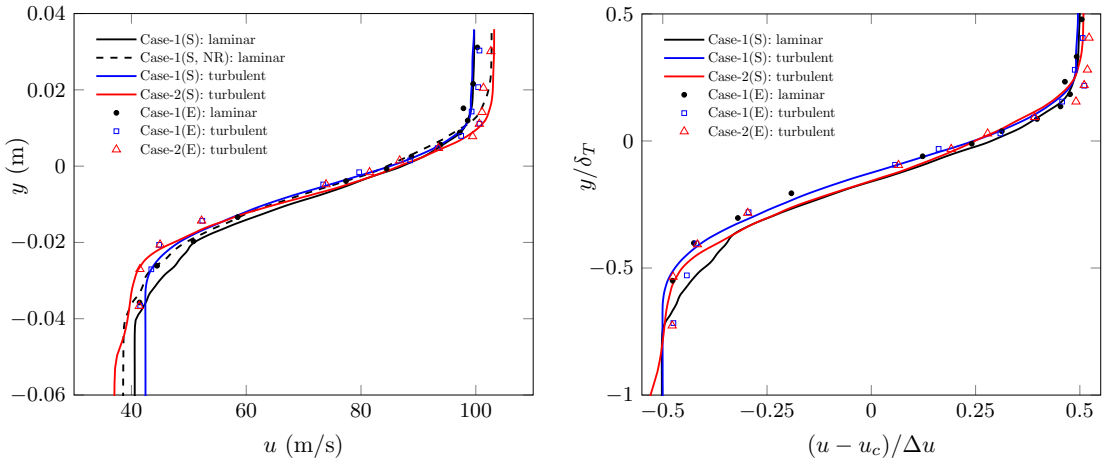

(a) physical coordinates

(b) non-dimensional coordinates

Figure 5.8: Streamwise velocity measurements from the experiments (E) are compared with data from the simulation (S) at the same locations. Non-reacting simulation data are marked as (NR).

Temperature profiles

The temperature rise in flows with hypergolic chemical reactions at high Damköhler numbers, such as in the cases studied here, is an indicator of molecular mixing. Capturing the temperature rise profile with good accuracy is therefore important, as it is an indicator of the amount of entrainment and mixing. The temperature rise is obtained by subtracting temperature in the non-reacting simulations from the temperature predicted in the chemically-reacting flow simulations. The rise in temperature is normalized by the adiabatic flame temperature rise is plotted in figure (5.9). We observe that the temperature rise profiles from the simulation are in good agreement with the experiment. The shape of the temperature rise profile and the spread is captured well. Furthermore, the location of the maximum temperature rise and its peak value is predicted with good accuracy within the experimental error estimates.

In figure (5.9), we observe that turbulent inflow condition leads to a higher peak temperature and a smaller value of δ_T (1% temperature rise thickness) compared to the flow with laminar inflow conditions, for the same free-stream composition of the

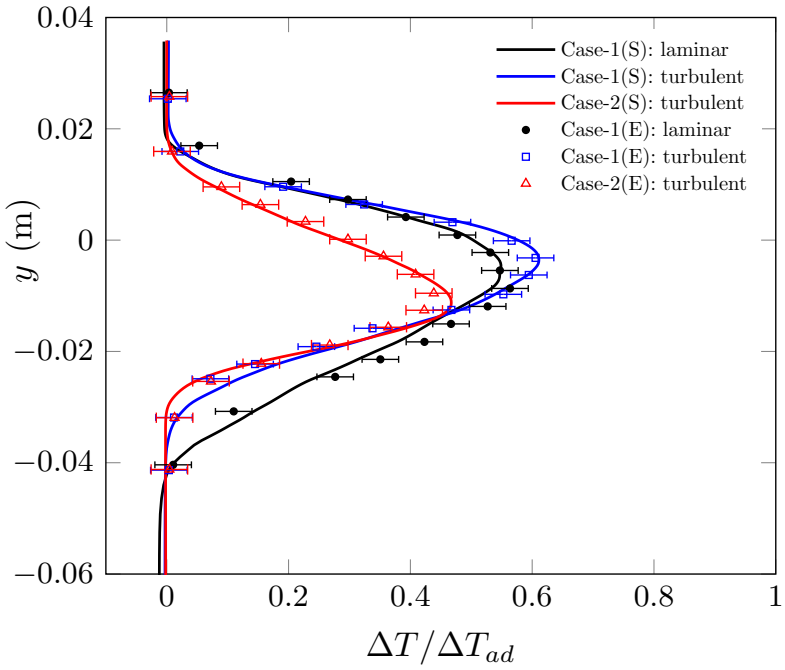

Figure 5.9: Comparison of normalized temperature rise at the measuring station for different inflow conditions and free-stream compositions.

two streams (Case-1). We also notice that the turbulent inflow conditions lead to a temperature rise profile with a marginal 'tilt' towards the lean-reactant side (primary-stream side for Case-1), when compared to the temperature rise profile obtained from the laminar inflow conditions. However, when the compositions of the two streams are changed, as in Case-2, we note a change in the nature of the temperature rise profile. The temperature rise profile agrees with the experimentally observed 'tilt' towards the secondary-stream (lean-reactant side in this case).

Studies by Mungal & Dimotakis [129], Koochesfahani et al. [19], Koochesfahani & Dimotakis [20], and Dimotakis [32] bring to light the significance of asymmetric entrainment of mixing layers in the context of chemically-reacting mixing layers. These studies reveal noticeable differences in the amount of product-formation and mean product formation profiles depending on which stream carries lean reactants. They attribute these differences to the asymmetric entrainment nature of the mixing layers. As mentioned previously, in the simulations studied here the temperature rise profile is a direct indicator of the amount of mixing, and hence, the amount of product formed and the mean product formation profiles. Therefore, capturing the nature of the temperature rise profiles and their peak correctly in Cases 1 and 2 suggest that the simulations represent the experimentally-observed asymmetric entrainment. Temporally-evolving mixing layers fail to produce this behavior which can only be observed in spatially evolving mixing layers. All simulation results in this section were obtained using the PaSR-2b sub-grid scale chemistry turbulence model. The roles of the sub-grid scale model and numerical method are discussed in the following section.

Sub-grid scale chemistry-turbulence model and bounded higher-order species reconstructions

Figure (5.10) shows the comparison of temperature rise plots at several streamwise locations for the PaSR models used in the simulations. Preliminary two-dimensional simulations with the PaSR-2 model showed no significant differences in the resulting temperature profiles relative to those with laminar finite-rate chemistry model. Since the two streams are predominantly composed of inert gases, the evaluation of the chemistry time scale using Eq. 2.23 results in large values of t_c, which leads to γ^* being unity. However, when t_c is evaluated using Eq. 2.29, in which the chemistry time scales

depend on the densities of reactive species, we note that there are several regions of the flow where γ^* is less than 1. This results in temperatures lower than the laminar finite rate chemistry predictions in a few regions of the flow, as seen in figure (5.10a). However, simulations with the PaSR-2b model result in temperatures that are not only significantly lower than the laminar finite-rate chemistry and PaSR-2a model, but are also very close to the experimental temperature rise measurements.

Simulations of non-premixed combustion often encounter multiple regions in the flow with steep gradients in species mass fractions. The use of symmetric higher-order numerical methods without carefully tuned dissipation, produces dispersive errors in the solution that lead to species mass-fractions exceeding their physical bounds, as shown in figure (5.11a). In the case of reacting flows, these errors in reactant mass fractions lead to spurious reactions and aphysical temperatures in the simulations, as shown in figure (5.12a). Mean-temperature profiles so obtained result in unreliable temperature predictions, as shown in figure (5.10b). However, when higher-order numerical methods that respect the physical bounds of the species mass fractions, developed in Subbareddy, Kartha & Candler [102], are implemented, we observe that the mass fractions are within the physical bounds, figure (5.11b) and temperature predictions in the computational domain are below that allowed by the adiabatic temperature rise (figure (5.12b)).

Figure (5.13) shows the temperature rise at multiple transverse locations at the measurement location, collected using 'numerical' probes. The temperature rise is normalized by the adiabatic flame temperature and vertically separated by 1 unit. These figures not only show the existence of hot and cold structures in the flow, as observed by Mungal & Dimotakis [129], but also show that the temperature rise in the simulations is well below the adiabatic flame temperature.

Grid resolution study

The sensitivity of the solutions to grid resolution is studied by simulating Case-1 and Case-2 flows with turbulent inflow conditions. A coarser grid with 6 million computational cells is used for this study. In the transverse direction, 1 cell is used to represent the splitter plate thickness, which means that the smallest cell in the simulation is three times larger than the cell in the 10 million element grid. The transverse and spanwise

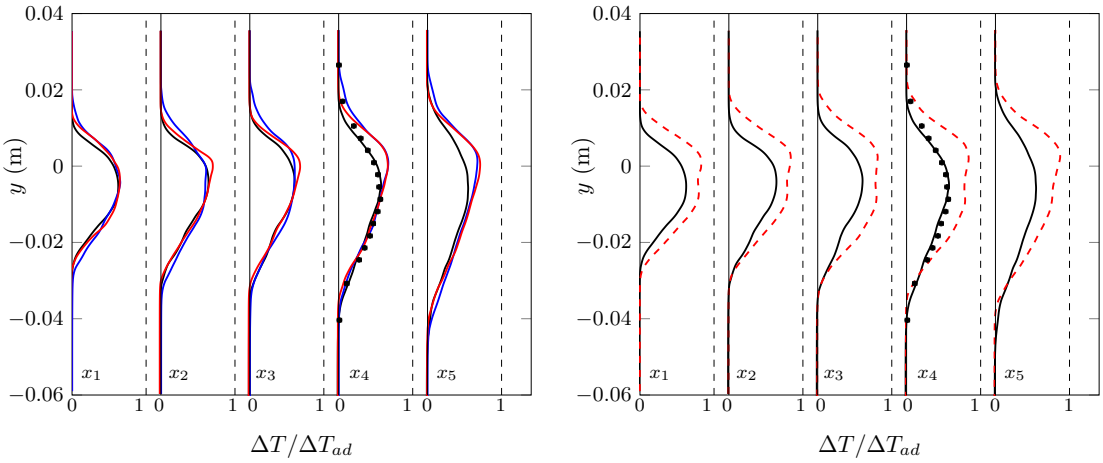

(a) Effect of SGS-chemistry turbulence model

(b) Effect of ensuring active scalar boundedness

Figure 5.10: Temperature profiles at several streamwise locations showing (a) the effect of using laminar finite-rate chemistry model (blue, solid line), PaSR-2a model (red, solid line), PaSR-2b model (black, solid line) using active scalar bounded fluxes and (b) the effect of using standard-shock capturing schemes (red, dashed lines). The dots in these figures represent the experimental data. Here, $x_{1,2,..,5} = [20, 25, 30, 35, 40]$ cm downstream of the splitter plate trailing-edge.

directions have only $\sim 75\%$ of cells for the same domain length, compared to the 10 million element grid. In the streamwise direction, however, the grid density is not changed considerably. Figure (5.14) shows that the results from the two grids used in this study yield nearly similar temperature rise profiles, showing that the results are independent of the grid used for these simulations.

Growth rates

The mixing layer growth and thickness are computed based on the momentum thickness, temperature rise profiles, and chemical product thickness. The thickness based on temperature rise, δ_T, is obtained using the distance between the two points in the normalized temperature profile,

$$\Theta(y) = \frac{\Delta T}{\Delta T_{ad}}, \tag{5.4}$$

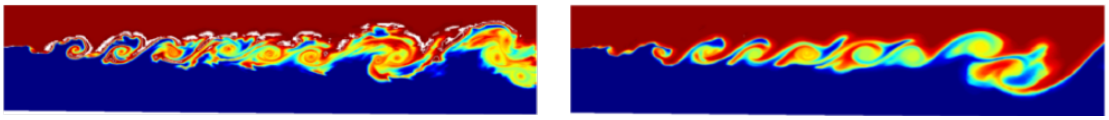

(a) standard shock-capturing fluxes (b) bounded active scalar fluxes

Figure 5.11: Contours of Y_{Ar} from a two-dimensional simulation of Case-1, plotted along with (white) lines that represent regions in the flow with mass-fraction overshoots.

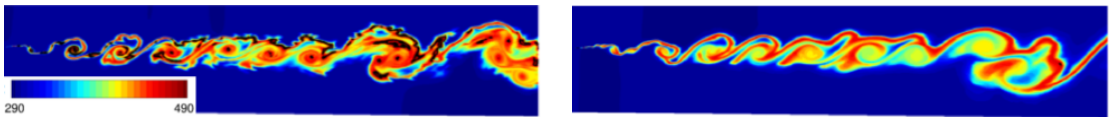

(a) standard shock-capturing fluxes (b) bounded active scalar fluxes

Figure 5.12: Contours of temperature from a two-dimensional simulation of Case-1, plotted along with (black) lines that represent regions in the flow with temperatures above that allowed by the adiabatic flame temperature rise.

at 1% of its peak value. The momentum thickness is evaluated as

$$\delta_\theta = \int_{-\infty}^{\infty} \rho(\frac{1}{2}\Delta U - u)(\frac{1}{2}\Delta U + u)dy \tag{5.5}$$

and the product thickness, which represents the thickness of chemical product formed by reactants mixed at the stoichiometric-mixture ratio, is calculated as

$$\delta_p = \int_{-\infty}^{\infty} \Theta(y)dy. \tag{5.6}$$

Figure (5.15) shows nearly linear growth of the mixing for reacting and non-reacting simulations. We observe that simulations with laminar inflow conditions show a linear growth only beyond a streamwise location of nearly $x = 0.32\,\mathrm{m}$. Interestingly, the growth rate of the reacting and non-reacting mixing layers are nearly the same, pointing to the low heat-release in these simulation which results in minimal impact. Although the figure (5.15b) shows nearly equal δ_T for the flip cases with turbulent inflow conditions, figure (5.15c) shows that the product thickness is significantly different, illustrating the effects of asymmetric entrainment. Further, data from the experiments at the measurement location are compared with simulation data, and are reported in

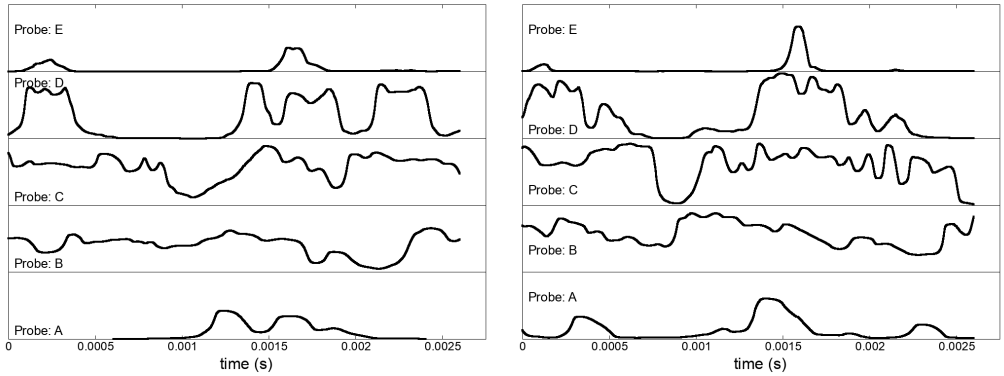

(a) Case-1, laminar inflow (b) Case-1, turbulent inflow

Figure 5.13: Measured temperature rise at multiple transverse locations at the measuring station.

Table 5.4.2. We note a reasonable agreement with the values from the experiment. The value of δ_p/δ_T, a non-dimensional estimate of the chemical product formation that is independent of the local mixing layer width, matches within 10% of the experimental values. Further, the measured Reynolds number in the simulation matches well with those observed in the experiment, which shows that the mixing layer simulations are well beyond the mixing transition (Re $\sim 10^4$) [127].

Table 5.2: Comparison of experimental (E) data from Slessor et al. [1] and data from present simulations (S) at the experimental measurement station located at $x = 36.5$ cm from the trailing end of the splitter plate.

Run	δ_T/x	$\delta_T/(\text{mm})$	$\delta_p/(\text{mm})$	δ_p/δ_T	$Re_\delta \times 10^5$	δ_θ
Case-1, laminar (E)	0.178	65.1	18.0	0.277	2.3	-
Case-1, laminar (S)	0.153	55.1	16.5	0.299	2.01	51.6
Case-1, tripped (E)	0.140	51.1	15.0	0.293	1.8	-
Case-1, tripped (S)	0.142	51.2	15.7	0.306	1.75	44.5
Case-2, tripped (E)	0.123	50.5	10.7	0.211	1.8	-
Case-2, tripped (S)	0.132	54.1	12.4	0.229	1.85	48.6

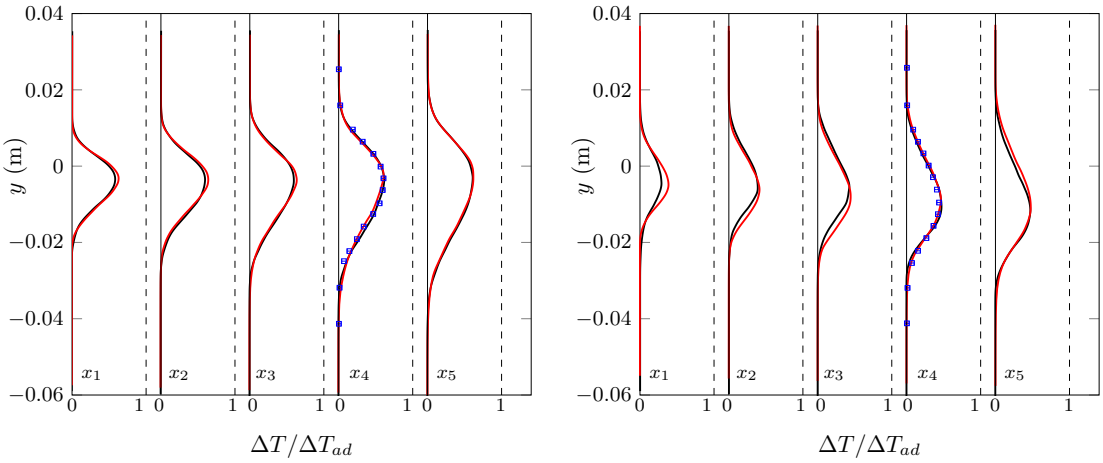

(a) Case-1 (b) Case-2

Figure 5.14: Temperature rise profiles at streamwise locations (x_i) computed using 10 million element grid (black lines) and 6 million element grid (red lines). Here, $x_{1,2,..,5} = [20, 25, 30, 35, 40]$ cm downstream of the splitter plate trailing-edge. Experimental data are represented by square symbols.

Favre-averaged stresses

Figure (5.16) shows the Favre-averaged stress profiles. Here R_{ij} are obtained from the collected Favre-averaged quantities in the simulations. They are computed from the following equation

$$R_{ij} = \frac{\overline{\rho u_i'' u_j''}}{\bar{\rho}(\Delta U)^2}. \tag{5.7}$$

Here, $\Delta U = U_1 - U_2$, is the difference in velocities of the two streams. Reynolds stresses are computed at different locations along the streamwise direction, we observe that these plots nearly collapse on each other for all components of Reynolds stresses beyond $x = 0.32\,\text{m}$ for the laminar mixing layer, indicating that mixing layer has attained self similarity. However, for the turbulent mixing layers, these profiles are seen to collapse as early as 0.05 m. This significantly shorter distance for attaining self similarity was also reported in Bell & Mehta [142]. These Favre-averaged profiles are then averaged in the self-similar region and presented in figure (5.16). Along with the data

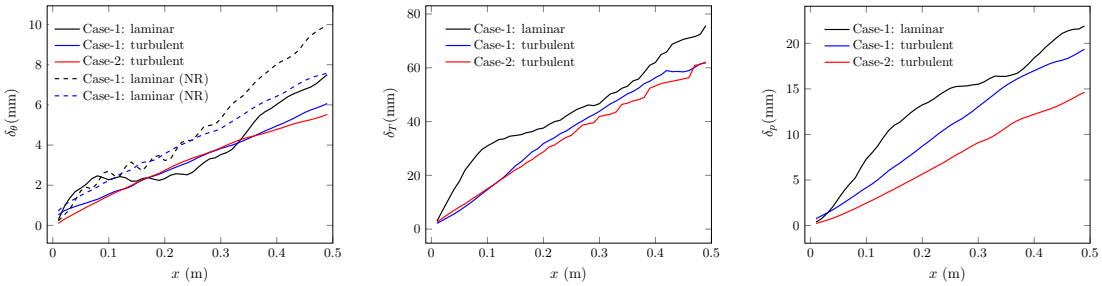

(a) (b) (c)

Figure 5.15: Comparison of (a) momentum thickness, (b)1% temperature rise thickness and (c) product thickness for different inflow conditions and free-stream composition, along the streamwise direction. Non-reacting simulation data is marked as (NR).

from this simulation, other experimental and computational results are plotted for reference. Figure (5.16) shows that while reacting and non-reacting simulations have nearly the same nature and peak values of turbulent stresses, simulations with laminar inflow conditions have noticeably higher peak values of turbulent stresses compared to the simulations with turbulent inflow. Analysis of this data is still in progress, more details will be provided in an upcoming publication.

5.5 Conclusion

In this work chemically reacting, spatially-evolving, subsonic mixing layers were studied by performing large-eddy simulations. Reactions in this flow were characterized by a high Damköhler number, implying that the temperature rise is an indicator of the amount of mixing. Reacting and non-reacting mixing layers were simulated with the Vreman turbulence model and a grid resolution study was presented. A numerical method that respects the physical bounds of species mass-fractions and thermodynamics, developed by Subbareddy et al [102], was employed to reduce active scalar overshoots and temperatures overshoots above the adiabatic-flame temperature. We demonstrate that numerical methods and sub-grid scale chemistry-turbulence interaction models used in the simulations play a critical role in determining the correct flow physics. Computed

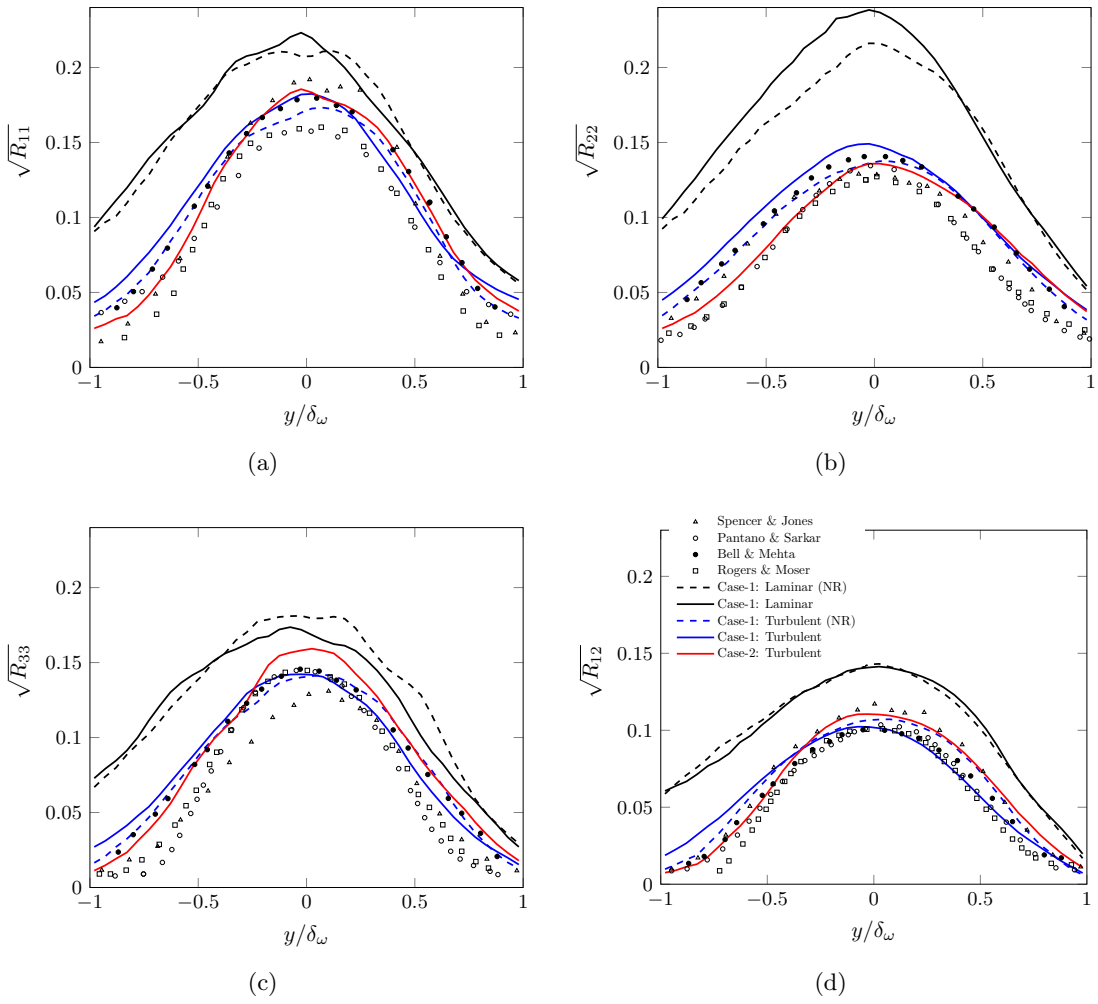

Figure 5.16: Favre averaged fluctuating flow quantities. Symbols correspond to the data from the experiments, while the lines show the data from the present simulation. Non-reacting simulation data are marked as (NR).

velocity and temperature rise profiles compare well with those measured in the experiment. Laminar and turbulent inflow conditions are seen to change the structure and the preferred chemical composition in the shear layer. Heat release effects, in the low-heat release cases studied here, are seen to have only minimal influence on the flow field. Computed turbulent stresses have minimal change in the reacting cases compared to the non-reacting cases due to the low-heat release in cases considered. Mixing layer simulations with laminar inflow conditions show higher values of turbulent stresses compared to simulations with turbulent inflow conditions. PDFs suggest that there is a significant difference in the nature of entrainment for laminar and turbulent inflow conditions and minimal change due to the presence of chemical reactions (low heat release).

Chapter 6

LES of inclined ramp geometry

6.1 Introduction

In this chapter, we study a class of chemically-reacting, spatially-evolving, supersonic mixing layers via large-eddy simulations. Specifically, the goal is to reproduce the experimental results on molecular mixing and heat release performed at Caltech by Bonanos et al. [2]. Here, the mixing layer is formed as a result of the interaction of supersonic and subsonic streams: the supersonic stream expands over a 30° perforated ramp and interacts with a subsonic stream of fluid injected into the combustor through the ramp. The primary (top, supersonic) stream contains a small amount of H_2 as the fuel. The secondary stream (injected through the ramp) contains a fractional amount of F_2 which acts as the oxidizer.

The hypergolic reaction between hydrogen and fluorine is characterized by a large Damköhler number, making the chemistry fast compared with the flow time scales. Hence, the product formation and temperature rise in the flow is mixing limited. Both reacting and non-reacting simulations are performed with two turbulence models (Smagorinsky and Vreman [38]) and comparisons are made with the available experimental data. The species fluxes are evaluated using the ideas presented in Chapter 3 to ensure boundedness and conservation of species mass fractions. The simulations show close agreement of the velocity profiles and the temperature rise profiles to those measured in the experiment.

Several studies, both experimental [1, 8, 10, 14, 21, 134] and computational [25, 26, 30,

164,165], have been done on conventional mixing layers, chemically-reacting mixing layers [158,166] and jets in crossflow. The geometry and the flow in the present simulations are slightly different from that of a conventional mixing layer. The 'expansion-ramp' geometry [2] is compact, as required for practical applications [167], and also minimizes total-pressure losses by avoiding the possibility of bow-shock formation [2]. The primary, supersonic, stream is injected through the top of the test section while the secondary, subsonic, stream is injected through a porous inclined ramp. In the experiment, the value of the secondary stream velocity is intentionally chosen to provide insufficient entrainment into the shear layer. As a result, the top stream reattaches on the lower wall of the test section some distance downstream, creating a subsonic recirculation region. This recirculation region helps in flame holding [2], which is important in a combustor.

From a computational standpoint, however, kinetically-fast reactions pose a challenge if the source term is treated in an explicit manner, as is done in this work. The kinetically-fast reactions impose a strict requirement on the time step for stable numerical simulation, leading to a physical time step of approximately 8.6×10^{-8} sec for the present calculation.

6.2 Computational domain and setup

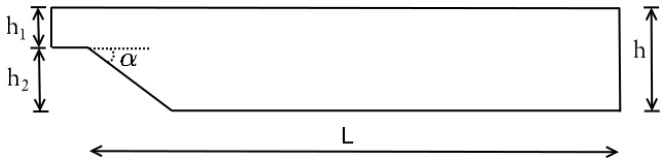

Figure 6.1: Sketch of the computational geometry.

Figure (6.1) shows a sketch of the computational geometry. The total height (h) of the test section is 8.38 cm. The supersonic top stream height, h_1, is 3.3 cm and the distance from the splitter plate tip to the lower wall of the test section is $h_2 = 5.08$ cm. The porous ramp through which the secondary stream is injected is placed at an angle (α) of 30° with the horizontal. The length of the test section from the tip of the splitter plate to the location of the probes is $L = 46.7$ cm. The test section ends at 50 cm in the

computations and beyond this, a "dump tank" is placed to mimic the large-diameter cylindrical duct into which the fluid exits in the experiment. The spanwise (z-direction) computational domain length is 12.57 cm. The geometry is extended upstream of the supersonic injection to ensure that the initialization remains away from the dynamics inside the test section, maintaining a clean inflow.

Views of the computational grid are shown in figure (6.2). The grid used has approximately 9 million cells.

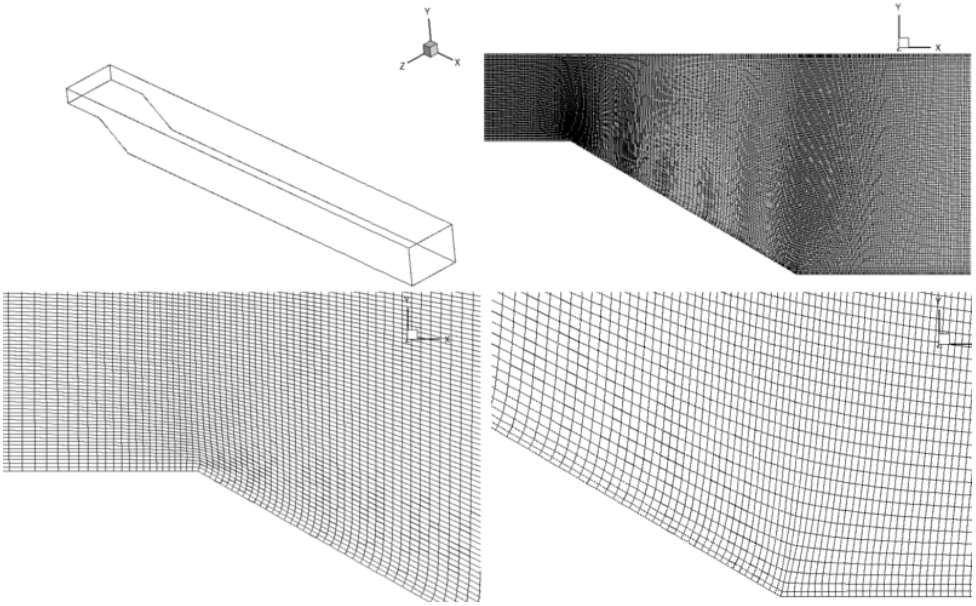

Figure 6.2: The computational grid used for this simulation. The image on the top left shows the edges of the computational domain (dump tank is not shown). The image on the top right gives a general idea of the density of the grid in a streamwise plane. The images on the bottom left and bottom right show the smoothness of the grid at the corners.

The density of grid points at the corners (at the splitter plate, intersection of the ramp and the bottom wall and intersection of the test section with the dump tank) is increased compared to the rest of the domain and care is taken to make sure that the corners and other parts of the grid are smooth. The grid cells in the dump tank are progressively coarsened to facilitate the handling of the subsonic boundary condition at

the outflow (discussed below).

The simulation is initially run for at least one convective flow time, during which the initial transients are convected out of the domain. Statistics are then collected for approximately two convective flow times. Here, the convective flow time is defined by the length of the test section and the convective velocity in the simulation. The simulations were run on a cluster consisting of 24-core 64-bit AMD Opteron CPUs connected with an Infiniband interconnect using 576 cores. The calculations took approximately 18 hours for one convective flow time.

6.2.1 Initial conditions

The simulations use the flow conditions from the experiments [2] and these are shown in Table 1. As mentioned earlier, the top stream contains a small amount of H_2 and NO (fuel and catalyst) while a fraction of the bottom stream is F_2 (oxidizer). The ratio of oxidizer to fuel is

$$\phi = \frac{[F_2]}{[H_2] + \frac{[NO]}{2}} = 4,$$

where [X] = moles of X. This gives rise to an adiabatic flame temperature rise, ΔT_{ad}, of 308 K. The velocity in the test section is initialized with a hyperbolic tangent function,

$$u(y) = U_1\eta(y) + U_2(1-\eta(y)), \qquad -h_2 \le y \le h_1, \qquad \eta(y) = 0.5(1+\tanh(\alpha y)), \quad (6.1)$$

where α is computed using

$$\frac{U_1 - u(\delta)}{U_1} = 0.01, \qquad \delta = 0.1h_2. \quad (6.2)$$

A similar approach for the initialization of the velocity in the test section was used by Matheou et al. [168]

The primary stream is introduced at ($U_1 = 570$m/s), while the secondary stream has a velocity of $U_R = 30$m/s, where U_R is the velocity normal to the ramp. Static pressure of the primary stream is 1bar, but the secondary stream is maintained at slightly lower pressure (0.95 bar). Both streams have a stagnation temperature of 288K. The top stream is composed of ($H_2,\ NO,\ Ar,\ He,\ N_2$) with corresponding mole fraction

percentages (1.90, 0.20, 19.0, 15.07, 73.83). The bottom stream contains (F_2, N_2, He) with mole fraction percentages (8, 76, 16).

The simulations performed correspond to a high convective Mach number (M_c = 0.88), high Damköhler number (Da = 2.2), and large Reynolds number (Re = $\frac{\Delta U \delta_T}{\overline{\nu}}$ $\approx 3 \times 10^6$) flow with a density ratio (ρ_R/ρ_1) of 0.456. The Reynolds number is based on the velocity difference ($\Delta U = U_1 - U_R$), temperature rise thickness for the chemically reacting flow (δ_T) and the average kinematic viscosity of the two streams ($\overline{\nu}$). Here, the convective velocity is computed using the formula

$$U_c = \frac{a_2 U_1 + a_1 U_2}{a_2 + a_1},$$

where a_1, a_2 are the speeds of sound in the top and the bottom streams respectively and U_2 is the horizontal component of the velocity injected through the ramp.

6.2.2 Boundary conditions

Supersonic boundary conditions are prescribed at the inlet for the laminar primary stream, whereas constant ramp normal velocity, stagnation temperature and static pressure are prescribed for the secondary stream (through the angled ramp). In the experiments, beyond the test section, the flow expands into a large duct and is neutralized before it is exhausted to the atmosphere [169]. To start the simulation as close to the experimental outflow condition as possible, the dump tank is initialized with pure nitrogen, the chemistry in the dump tank is deactivated and at the far end of the computational domain, subsonic outflow boundary conditions (Poinsot and Lele [50], extended to handle multiple species by Yoo and Im [162]) are prescribed. Beyond the test section, numerical dissipation was progressively added as a function of streamwise distance to ensure that the flow exits at the prescribed pressure with minimal numerical reflections at the outflow. Slip-wall boundary conditions are prescribed at the top and bottom walls of the test section and periodic boundary conditions are prescribed in the spanwise direction.

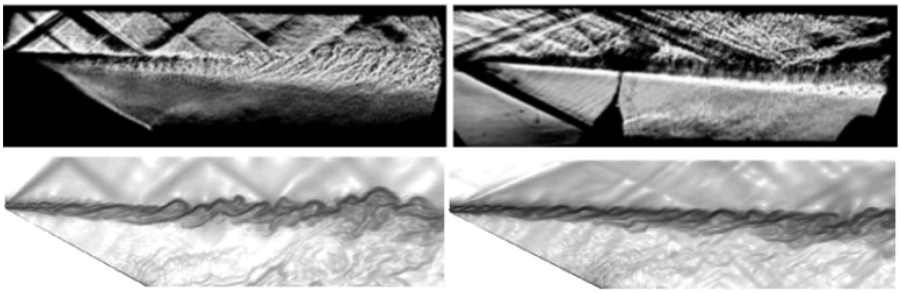

Figure 6.3: Comparison of the non-reacting flow fields from the experiment and simulation. The image on the top left shows the Schlieren image for $M_1 = 1.5$ and $M_1 = 2.5$ is shown on the top right. The images below show the density gradient magnitude of the corresponding computed flow fields.

6.3 Results

6.3.1 Non-reacting simulations

As a first step, a non-reacting flow was computed in order to understand the mean-flow behavior. For these cases, the gas is N_2, but the setup and boundary conditions are the same as those discussed above. The top stream Mach number in the first case is $M_1 = 1.5$ (with $U_1 = 470\,\mathrm{m/s}$, $U_R = 23\,\mathrm{m/s}$) and for the second case, $M_1 = 2.5$ (with $U_1 = 570\,\mathrm{m/s}$, $U_R = 30\,\mathrm{m/s}$). Centerplane (x-y, zoomed into the ramp region) slices from the simulations with contours of the density gradient magnitude and corresponding Schlieren images from the experiment and are shown in figure (6.3). The flow fields are qualitatively similar.

The angles in the shock trains closely match each other. Furthermore, the primary stream remains nearly horizontal in the $M_1 = 1.5$ flow and bends downwards in the $M_1 = 2.5$ flow. This behavior is clearly visible in the results from the simulation and suggests that the simulations correctly represent the entrainment rates.

A fuller view for the $M_1 = 1.5$ case is shown in figure (6.4). Two of the main flow features, the secondary shear layer and the recirculation region appear to be well matched (the top figure labels both these features).

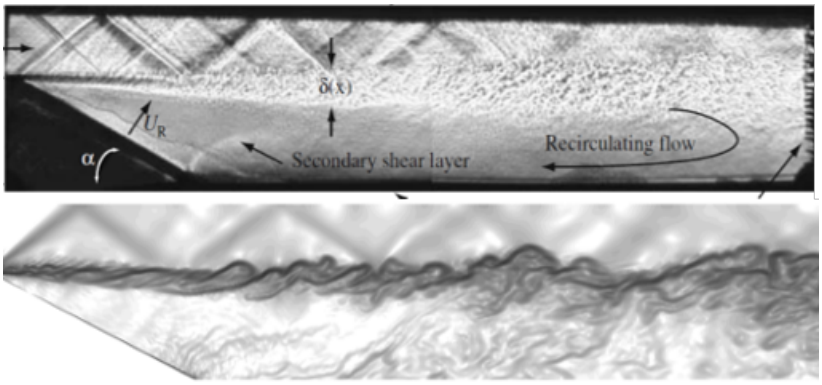

Figure 6.4: The comparison of the full Schlieren image from the experiment for $M_1 = 1.5$ flow and the density gradient magnitude plot from the simulations. The secondary shear layer and the recirculating flow are the focus of this comparison.

6.3.2 Reacting and non-reacting multi-species flow simulations

Previous work by Ferrero et al. [158], which examined subsonic, chemically reacting mixing layers (corresponding to experiments by Slessor et al. [1]), revealed issues related to the excursions in the species mass fractions. These excursions in the species mass fractions result in additional aphysical reactions between the fuel and the oxidizer, thereby creating more products and heat release. This causes erroneous overshoots in the temperature field. To mitigate this issue, we use limiters on the reconstructed species concentrations, used in the flux evaluation in order to ensure boundedness of the species mass fractions, as discussed in the previous sections.

To analyze the chemically-reacting flow, two simulations were performed: (a) multi-species with the chemistry inactive and (b) multi-species with finite-rate chemistry activated. Both simulations were performed with the same chemical composition, as mentioned in Table 1. Smagorinsky and Vreman turbulence models were used for each case. With the value of Smagorinsky constant equal to 0.1, the non-reacting mixing layer showed breakdown to turbulent flow but, with a value of Smagorinsky constant of 0.2 the flow remained laminar. Thus, for both the reacting and the non-reacting simulations, the value of the Smagorinsky constant was set to 0.1 for the final set of simulations.

Velocity and temperature profiles

Figure (6.5) compares the velocity profile in the simulations with that in the experiment at the experimental measuring station ($x = 46.7\,\text{cm}$). The velocity profile from the simulations is seen to closely follow the measured value of velocity in the experiment. The simulation with the Vreman model for the SGS terms captures the velocity profile slightly better than the simulation with Smagorinsky model. Near the top wall, a mismatch in the velocity profiles is observed which is most likely due to the top wall being modeled as a slip wall.

Meanwhile, closer to the lower wall, the velocity profile from the simulation does not match the data from the experiment with great accuracy, which is an indicator of the fact that the recirculation region is not perfectly matched in the simulation. Note that there are difficulties in the accurate measurement of separated flow with pitot tubes facing upstream in the region of recirculation. In the experimental data, a hyperbolic tangent function was fitted to correct the velocities obtained from direct measurement and is used to extrapolate the velocity profile in the regions of recirculation [2]. This data is labeled as 'corrected measurements' in figure (6.5).

Figure (6.5b) compares the velocity profiles of the reacting flow with those in the experiment. The plots show that the velocity profiles in the simulations do not match the experimental data as accurately as in the non-reacting flow simulation. Nevertheless, the velocity profiles from the simulations appear to be in reasonable agreement with the experiments. In the simulations, the top and the bottom walls are modeled as slip walls: as a result, the simulations do not reproduce the boundary layer formed on the top wall (in the experiments) which has a displacement effect on the flow. This is most likely the reason for the slight upward shift in the velocity profiles in the simulation. The experimental data presented in figure (6.5b) is from Bonanos and Dimotakis (private communication; a detailed publication by these authors is in preparation).

The rise in temperature normalized with adiabatic flame temperature rise is plotted in figure (6.6). This temperature rise in the figure was obtained by subtracting the temperature data in the non-reacting flow from the chemically reacting flow. Interestingly, the temperature rise profile from the simulation is in good agreement with the experiment. The Smagorinsky model captures the temperature rise profiles very closely when compared to the experiments. Although the solution obtained from the Vreman

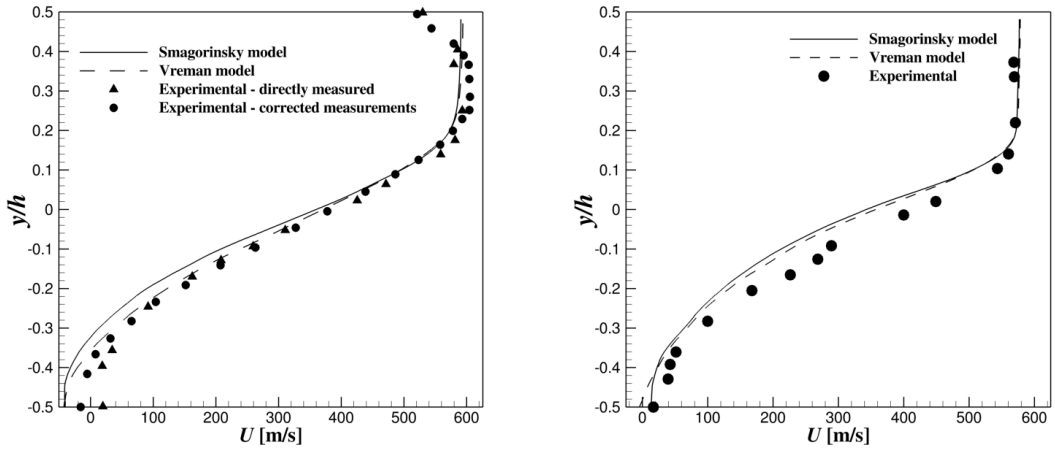

(a) Non-reacting flow velocity profiles

(b) Reacting flow velocity profiles

Figure 6.5: Comparison of velocity profiles for the non-reacting and reacting flows at the measuring station $x = 46.7\,\text{cm}$.

model is close to the experimental data, the temperature rise in the recirculation region (closer to the lower wall) is slightly larger compared to the results using the Smagorinsky model.

This discrepancy could possibly be due to the differences in the top stream entrainment into the recirculation region. In the next sub-section this behavior is revisited and is explained using plots of the probability density of the mixture fraction, ξ. With both SGS models, the location of the maximum temperature rise is captured well, and the error in the normalized maximum temperature rise is about 5%. This is significantly lower than the error in the prediction of temperature rise (27%) from previous low-speed simulations [158]. The temperature rise plot from the simulations performed without limiters on the species concentration are also plotted in figure (6.6). The result from this simulation shows a huge overshoot in the temperature rise profile, which is obviously incorrect. Clearly, limiting the species concentration reduces the erroneous species mass formation, and hence improves the predicted values of heat release and temperature rise in the simulations.

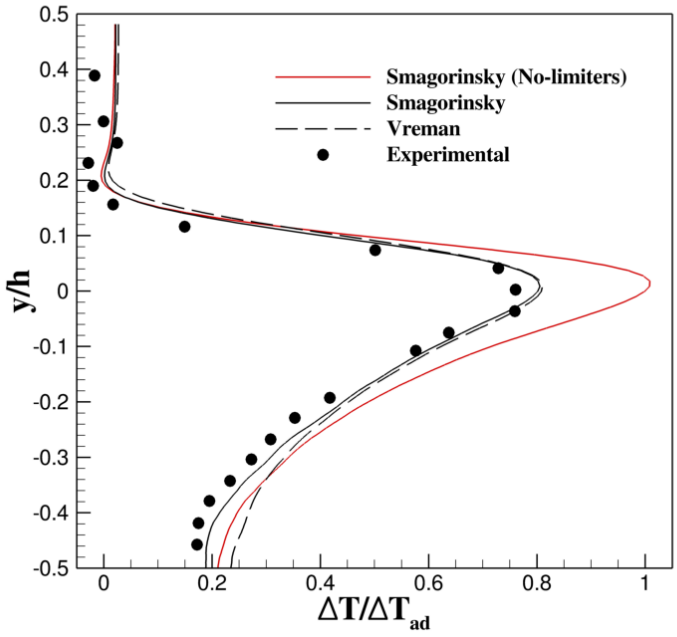

Figure 6.6: Comparison of the normalized temperature rise at the measuring station $x = 46.7\,\text{cm}$.

Probe data

"Numerical probes" were placed in the test section to collect statistics. The probes were placed at three x-locations ($x = 26.7\,\text{cm}$, $36.7\,\text{cm}$ and $46.7\,\text{cm}$). In each of these planes, the probes are placed at several locations along the height of the test section and across the spanwise direction. The data collected were used to calculate the mixture fraction ξ, which is defined as the mole fraction of high-speed stream fluid [20,32]. With this definition, $\xi = 0$ corresponds to pure low-speed-stream fluid, $\xi = 1$ represents pure high-speed-stream fluid and any values in between represents the fraction of high-speed-stream fluid. Complete consumption of all reactants, leading to the largest possible temperature rise, occurs at the stoichiometric mixture mole fraction

$$\xi_\phi = \frac{\phi}{\phi + 1}, \tag{6.3}$$

which is $\xi_\phi = 4/5$ for this flow. Based on the probe data, it is possible to build a probability density function $\mathscr{P}(\xi; y)$ of the mixture fraction at each transverse location.

Probability density functions

Figures (6.7 and 6.8) show the probability of finding mixed fluid across the height of the test section at a particular streamwise location. Figures (6.7a-c) show the PDF for the non-reacting flow using the Smagorinsky model. These figures show that as one moves downstream, the nature of the PDF changes. In the regions closer to the lower wall, a departure from the peak at $\xi = 0$ is visible. It is also seen that the PDF develops a spread closer to the lower wall. This indicates that there is a greater amount of top stream fluid being entrained into the lower stream in the recirculation region.

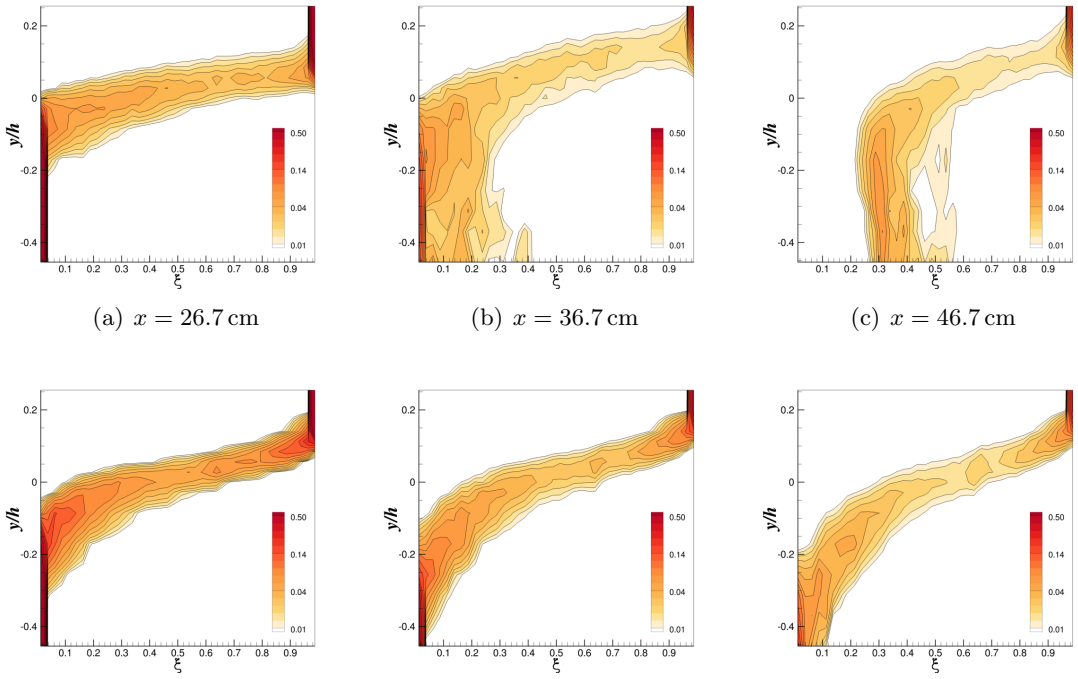

(a) $x = 26.7\,\text{cm}$ (b) $x = 36.7\,\text{cm}$ (c) $x = 46.7\,\text{cm}$

(d) $x = 26.7\,\text{cm}$ (e) $x = 36.7\,\text{cm}$ (f) $x = 46.7\,\text{cm}$

Figure 6.7: The probability density functions for the non-reacting (top) and the reacting (bottom) flow simulations computed with the Smagorinsky SGS model.

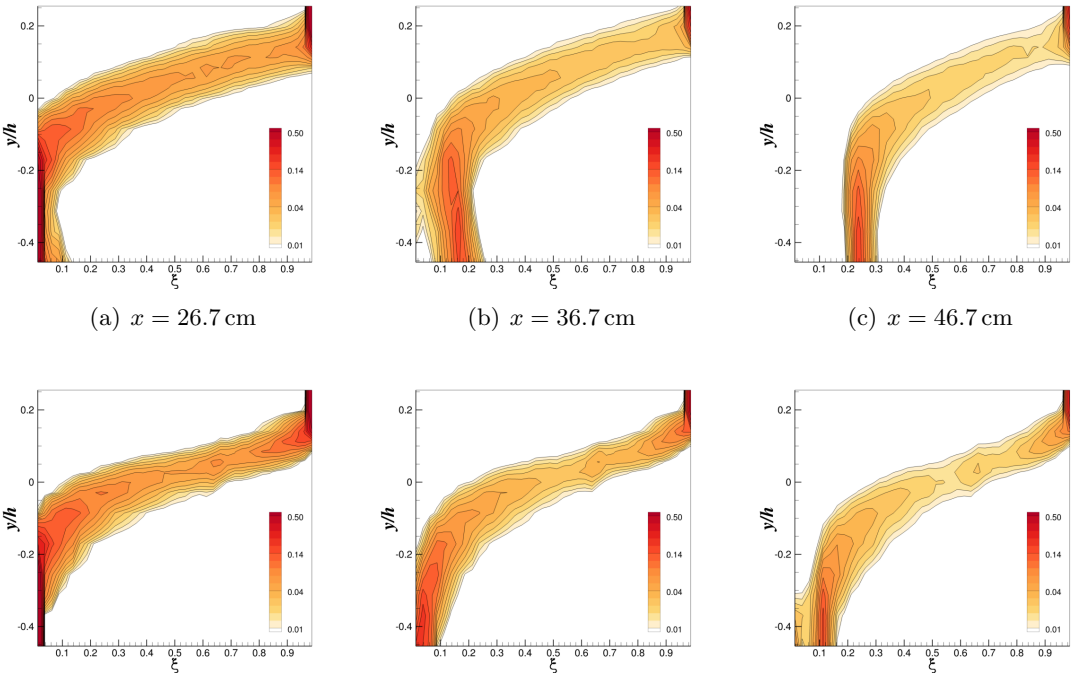

(a) $x = 26.7\,\text{cm}$ (b) $x = 36.7\,\text{cm}$ (c) $x = 46.7\,\text{cm}$

(d) $x = 26.7\,\text{cm}$ (e) $x = 36.7\,\text{cm}$ (f) $x = 46.7\,\text{cm}$

Figure 6.8: The probability density functions for the non-reacting (top) and the reacting (bottom) flow simulations computed with the Vreman SGS model.

Close to the experimental measuring station at $x = 46.7\,\text{cm}$, (see figure (6.7c)), at the lower wall, the PDF tends to move away from $\xi = 0$ and is centered about a value closer to 0.35. This shows the formation of a recirculation region with well-mixed fluid. Also, the contours seem to be aligned vertically, indicating that the large-scale motions in the flow have effectively mixed the two streams. This could be interpreted as the asymptotic value of ξ in the recirculation region. Had the molecular mixing been more efficient, the spread of the PDF about its asymptotic value would have been a minimum (one would have seen a narrow line at the asymptotic value). The spread reveals that perfect molecular mixing has not been achieved. One could make a similar inference from figures (6.8a-c), which were obtained with the Vreman model. Note that the data for these simulations were sampled for a longer duration, and hence have more precise

peaks.

For the reacting-flow simulations, figures (6.7d-f) and figures (6.8d-f), the PDF looks significantly different from the corresponding non-reacting flow, showing that heat release and chemical reactions affect the flow field and change the chemical composition in the recirculation region. An isosurface of the composition of argon, used here as a top-stream marker, is shown in figure (6.9). This figure reveals a significant change in the entrainment of the top stream into the recirculation region for the non-reacting and reacting flows which supports the observation from the PDF plots. This change in entrainment ratio has a direct effect on the temperature rise. Comparing figures (6.7f and 6.8f), it could be argued that the difference in the temperature rise profiles (see figure 6.6)), for the two turbulence models, close to the lower wall, is due to the differences in the values of ξ observed in the calculations. In the Vreman model, close to the lower wall, the value of ξ is observed to be larger than the Smagorinsky model. It is expected that with a relatively larger amount of top stream being present in the recirculation region, the temperature rise would be higher. Hence, we observe a larger temperature rise in the recirculation region for the simulation when using the Vreman model.

These plots also indicate that the use of passive scalars to estimate the temperature rise via non-reacting simulations may not give the right temperature rise prediction. This is mainly because heat release and chemical reactions in the high-speed flow changes the flow field considerably. However, a passive scalar based method could give a reasonable prediction of the temperature rise in the low speed flows where such strong coupling between heat release and temperature rise is absent.

Figures (6.10 and 6.11) show the Reynolds stress profiles. Here R_{12} (Reynolds stress), k (turbulent kinetic energy), R_{uT} and R_{vT} are obtained from the collected Favre averaged quantities from the simulations. They are computed from the following equations

$$k = \widetilde{u''u''} + \widetilde{v''v''} + \widetilde{w''w''}, \tag{6.4}$$

$$R_{uT} = \frac{\widetilde{u''T''}}{\Delta U T_\circ}, \qquad R_{vT} = \frac{\widetilde{v''T''}}{\Delta U T_\circ}, \qquad R_{12} = \frac{\overline{\rho u'' v''}}{\rho_1 (\Delta U)^2}. \tag{6.5}$$

Here, $\Delta U = U_1 - U_R$ and $T_\circ = 288$K, which is the stagnation temperature of the two streams. In a reacting mixing layer, it is expected that the Reynolds stresses decrease

compared to the non-reacting mixing layer [32]. This trend is observed in figure (6.10a and 6.11a). Also, figure (6.10b and 6.11b) show a decrease in the turbulent kinetic energy, indicating an overall decrease in the turbulent fluctuations. Further, the decrease in the width of the curves in both reacting simulations, figure (6.10a,b and 6.11a,b), compared to the corresponding non-reacting simulations, points to a decrease in the mixing layer thickness for the reacting simulations. Interestingly, the R_{uT} and R_{vT} behaviors are significantly different for the reacting flow when compared with the non-reacting flow obtained with both turbulence models. The reacting flow simulations show a flip in the nature of R_{uT} and R_{vT} compared to the non-reacting flow. This happens largely due to the difference in the nature of the gradient of the temperature profile in the reacting flow (induced by chemical reactions) and the non-reacting flow. This behavior indicates a strong correlation between the velocity-temperature fluctuations. More interpretation of this behavior will be presented in an upcoming publication.

Visualization and baroclinic torque

Figure (6.12) compares the Q-criterion plots for the reacting and the non-reacting flows. Here, Q is the second invariant of the velocity gradient tensor and is colored by the local value of the streamwise velocity. The Q-criterion plots for the non-reacting flow simulations show coherent hairpin-like structures that extend a fair amount into the primary stream. This is seen to be significantly reduced in the chemically reacting flow. Further, these plots also give an indication that the scales of the turbulent structures in the reacting flows are noticeably smaller than the scales seen in the non-reacting flow. The Q-criterion plots also show that the secondary shear layer (formed at the intersection of the ramp and the lower wall) is considerably diminished in the reacting flow, pointing to a decrease in recirculation and the amount of fluid flowing upstream close to the lower wall. This is consistent with the empirical observation of reduced entrainment rate requirement in reacting mixing layers. The reduced entrainment requirement forces the top-stream to reattach further downstream, compared to the non-reacting flows, thereby reducing the amount of fluid moving upstream closer to the lower wall. Viewing figures (6.9 and 6.12) together, supports the notion that the recirculation region in the chemically reacting flow is pushed further downstream compared to the non-reacting flow.

Misalignment in the gradients of pressure and density gives rise to baroclinic torque. Flows with heat release due to chemical reactions show significant local density variation. Figures (6.13a and 6.13b) show the isosurfaces of the resolved-scale baroclinic torque for the non-reacting and the reacting flows. The contour levels have a magnitude of approximately five times the initial vorticity in one convective flow time. The increased role of baroclinic torque is evident if we compare figures (6.13a and 6.13b).

6.4 Conclusion

In this work a chemically-reacting, spatially-evolving, supersonic mixing layer is studied by performing large-eddy simulations. Bounded scalar fluxes are used to reduce the effect of excursions in the species mass fractions in the multi-species LES calculation. Both reacting and non-reacting mixing layers were simulated with two turbulence models: Smagorinsky and Vreman. Comparison of the Schlieren images from the experiment and the density gradient magnitude from the simulations show reasonable qualitative agreement. The computed velocity and temperature rise profiles compare well with those measured in the experiment for the chemically reacting flows. Computed turbulent stresses and turbulent fluctuations reduce in the chemically reacting flow, consistent with experimental observation [32]. Also, the PDF plots suggest that there is a significant difference in the flow field between the reacting and the non-reacting flow due to heat release. It is also seen that heat release significantly alters the chemical composition in the recirculation region, which is consistent with the experimental observations.

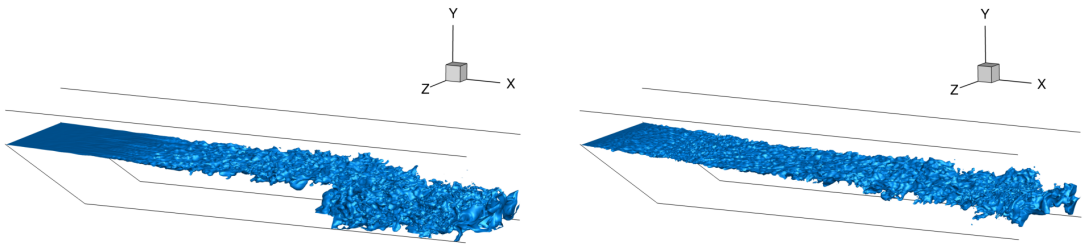

(a) Non-reacting flow

(b) Chemically reacting flow

Figure 6.9: Plots show an isosurface of the concentration of argon, which is present only in the top stream.

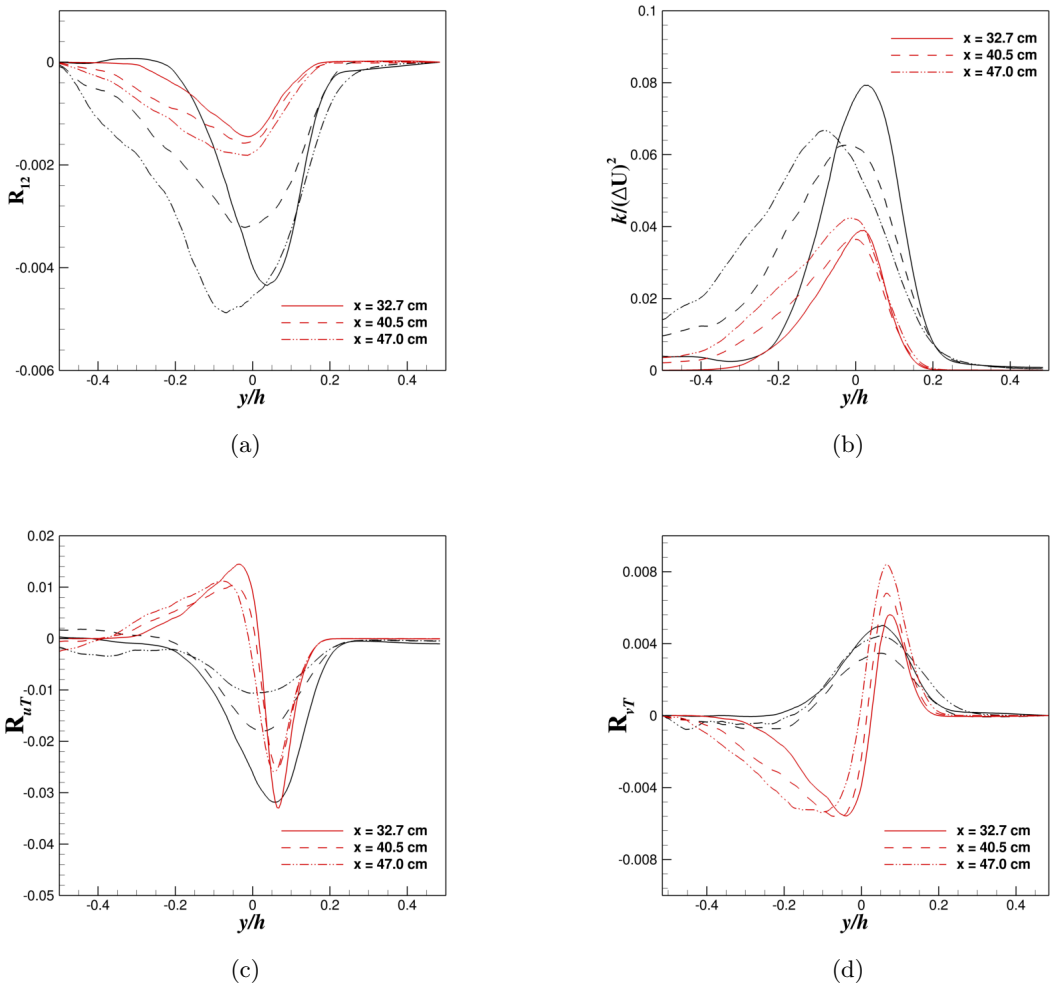

Figure 6.10: The Favre-averaged fluctuating flow quantities that are computed with the Smagorinsky SGS model. The black lines correspond to the non-reacting flow simulation, while the red lines correspond to the reacting-flow simulation.

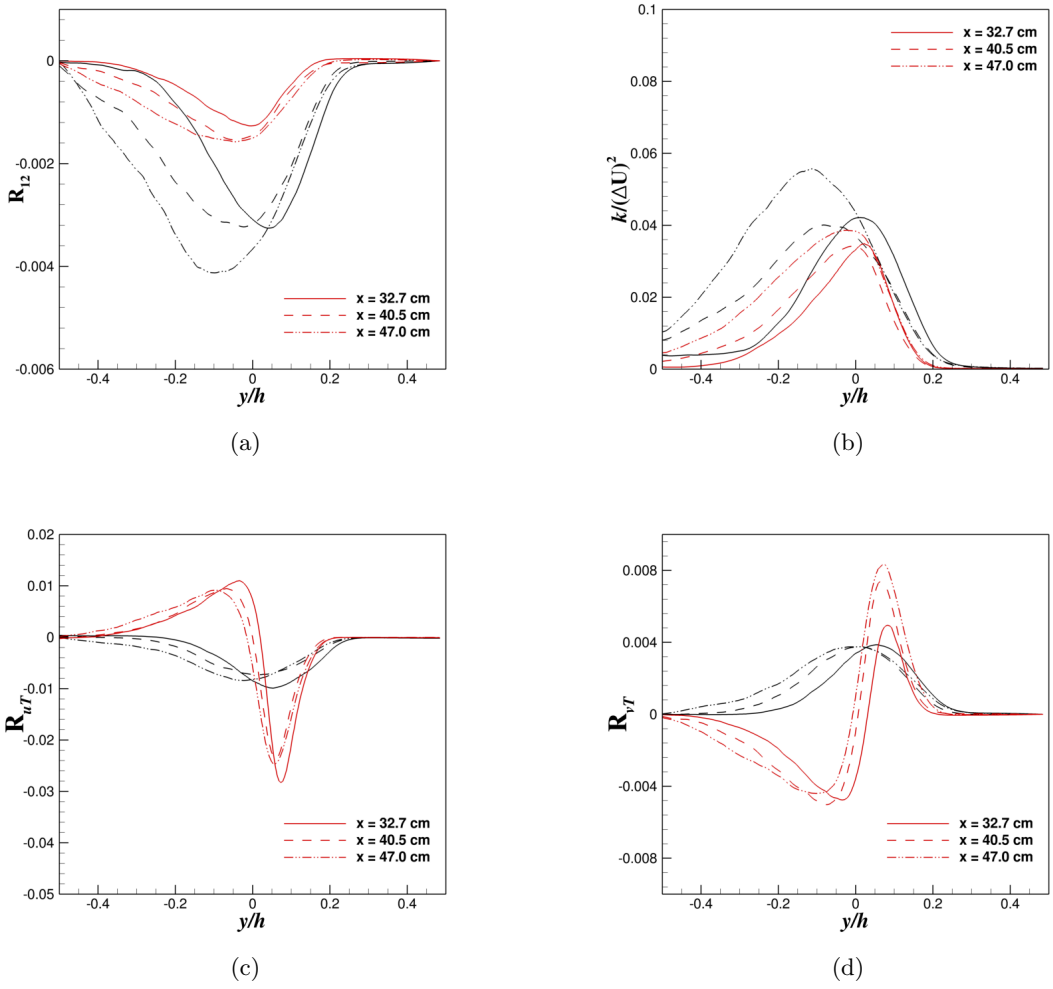

Figure 6.11: The Favre-averaged fluctuating flow quantities that are computed with the Vreman SGS model. The black lines correspond to the non-reacting flow simulation, while the red lines correspond to the reacting-flow simulation.

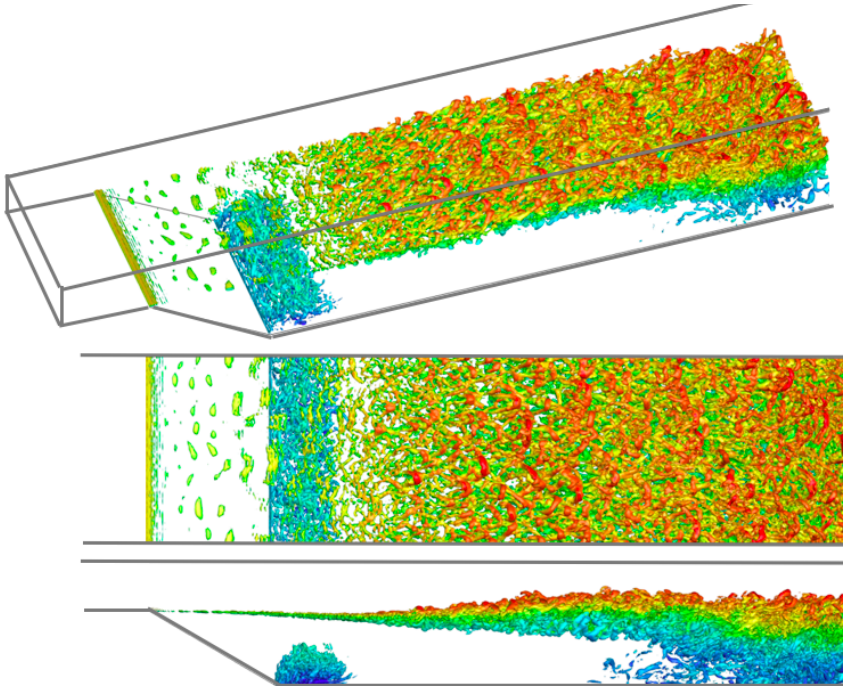

(a) Non-reacting flow

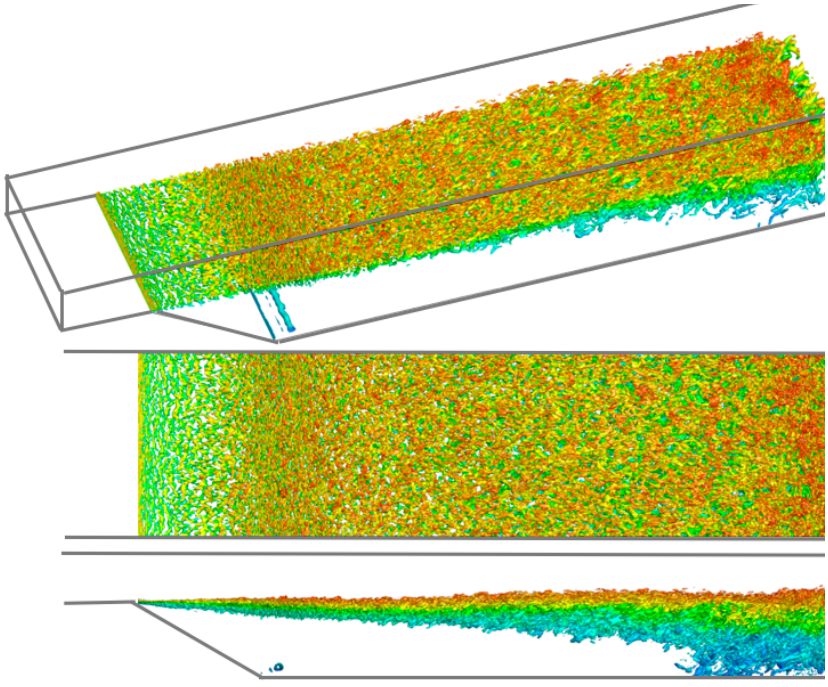

(b) Chemically reacting flow

Figure 6.12: The isosurface of the Q-criterion colored based on the local streamwise velocity. An angled view, top view and the side view of the test section are shown.

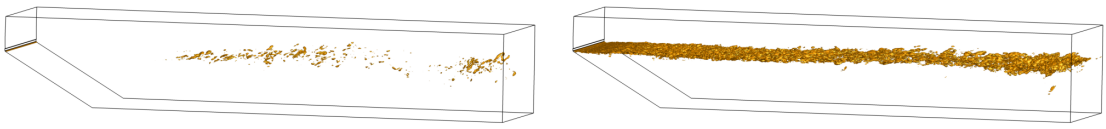

(a) Non-reacting flow (b) Chemically reacting flow

Figure 6.13: The isosurface of the resolved-scale baroclinic torque in the non-reacting and reacting flows.

Chapter 7

Conclusions and future work

In this work we developed a switched, low-dissipation flux methodology for scalar conservation and boundedness in compressible flows. The newly developed flux scheme uses a 'jump detector', a non-linear scaling limiter, and the addition of localized dissipation (using entropy eigen vectors only) to achieve the objectives of ensuring boundedness in scalar fields and maintaining low levels of dissipation. In this method, we also take care that the added dissipation does not affect vorticity and acoustic components of the flow. Maintaining boundedness of scalars (mass fractions) is found to be not only critical for conservation of mass, but also, to mitigate artificial chemical reactions and temperature rise in reacting flow simulations. A few heuristic choices, involving the low-dissipation switch and the jump detectors are made: these parameters can be tuned for specific applications. To demonstrate the effectiveness of the new method, several numerical tests were performed. We start our studies with simple one-dimensional problems and systematically add complexities to them. We then simulate two-dimensional mixing layers and shock-density bubble interaction problems and observe that the newly-developed method is capable of producing reliable simulations and results. Finally, we investigate high-Reynolds number chemically-reacting flows by performing large-eddy simulations corresponding to the experiments of Slessor et al. [1] and Bonanos et al. [2] at California Institute of Technology. We present the results of these simulations at length in Chapters 4, 5 & 6. In summary, the new numerical method is seen to significantly mitigate the overshoots and undershoots in mass fractions and temperature in the flow, resulting in more reliable flow predictions.

Simulations of spatially-evolving chemically-reacting mixing layers at high-Reynolds numbers required implementing several additional capabilities in the code. To prevent spurious numerical reflection from the boundaries, characteristic based subsonic inflow and outflow conditions were implemented. A digital filter based inflow turbulence generation method was implemented to mimic turbulent inflow conditions and was used, along with a wall-model developed by Komives [122]. The Hirschfelder-Curtiss approximation was put in place to account for differential diffusion of species. Further, to prevent over-prediction of chemical reactivity in a computational cell, sub-grid scale chemistry turbulence interaction models were employed. Finally, semi-implicit time integration was used to facilitate simulations with stiff chemical source terms. It was observed that all the abovementioned models were vital constituents, and were required to work in unison to yield reliable simulations of chemically-reacting flows at high Reynolds numbers.

7.1 Future directions

The bounded scalar flux methodology developed in this work was extensively tested for non-premixed flows. Its application and performance in problems involving premixed combustion is a natural next step in the broad scheme of studying chemically reacting flows. Investigation of premixed propane-air combustion is already in progress and will be reported in Candler et al. [170]. Secondly, work could be done towards reducing the computational overhead of the newly developed method for flows involving chemical reactions of large number of species. Incorporating ideas from this study into a evolution-variable manifold framework is also recommended as the combination of the two methods promise to be computationally faster and reliable. While, chemically-reacting mixing layers in this study were simulated using the Favre-averaged Navier-Stokes equations, the Reynolds-averaged framework developed by Sidharth G.S. [171] may alternatively be used to model sub-grid scale variable-density effects on the filtered vorticity. These effects are non-negligible particularly under strong heat release conditions.

References

[1] MD Slessor, CL Bond, and PE Dimotakis. Turbulent shear-layer mixing at high reynolds numbers: effects of inflow conditions. *Journal of Fluid Mechanics*, 376:115–138, 1998.

[2] Aristides M Bonanos, Jeffrey M Bergthorson, and Paul E Dimotakis. Molecular mixing and flowfield measurements in a recirculating shear flow. part ii: supersonic flow. *Flow, turbulence and combustion*, 83(2):251–268, 2009.

[3] Hiroshi Terashima and Grétar Tryggvason. A front-tracking/ghost-fluid method for fluid interfaces in compressible flows. *Journal of Computational Physics*, 228(11):4012–4037, 2009.

[4] MD Slessor, CL Bond, and PE Dimotakis. Turbulent shear-layer mixing at high reynolds numbers: effects of inflow conditions. *Journal of Fluid Mechanics*, 376:115–138, 1998.

[5] MG Mungal and CE Frieler. The effects of damköhler number in a turbulent shear layer. *Combustion and flame*, 71(1):23–34, 1988.

[6] Christopher Llewellyn Bond. *Reynolds number effects on mixing in the turbulent shear layer*. PhD thesis, California Institute of Technology, 1999.

[7] C. D. Winant and F. K. Browand. Vortex pairing : the mechanism of turbulent mixing-layer growth at moderate Reynolds number. *J. Fluid Mech.*, 63(02):237–255, 1974.

[8] Garry L Brown and Anatol Roshko. On density effects and large structure in turbulent mixing layers. *Journal of Fluid Mechanics*, 64(04):775–816, 1974.

[9] Anatol Roshko. Structure of turbulent shear flows: a new look. *AIAA journal*, 14(10):1349–1357, 1976.

[10] Paul E Dimotakis and Garry L Brown. The mixing layer at high reynolds number: large-structure dynamics and entrainment. *Journal of Fluid Mechanics*, 78(03):535–560, 1976.

[11] Miguel A Hernan and Javier Jimenez. Computer analysis of a high-speed film of the plane turbulent mixing layer. *Journal of Fluid Mechanics*, 119:323–345, 1982.

[12] John Harrison Konrad. *An experimental investigation of mixing in two-dimensional turbulent shear flows with applications to diffusion-limited chemical reactions*. PhD thesis, California Institute of Technology, 1977.

[13] R Breidenthal. Structure in turbulent mixing layers and wakes using a chemical reaction. *Journal of Fluid Mechanics*, 109:1–24, 1981.

[14] LP Bernal and A Roshko. Streamwise vortex structure in plane mixing layers. *Journal of Fluid Mechanics*, 170:499–525, 1986.

[15] Dorian Liepmann and Morteza Gharib. The role of streamwise vorticity in the near-field entrainment of round jets. *Journal of Fluid Mechanics*, 245:643–668, 1992.

[16] NT Clemens and MG Mungal. Two-and three-dimensional effects in the supersonic mixing layer. *AIAA journal*, 30(4):973–981, 1992.

[17] M Samimy, MF Reeder, and GS Elliott. Compressibility effects on large structures in free shear flows. *Physics of Fluids A: Fluid Dynamics*, 4(6):1251–1258, 1992.

[18] Gregory S Elliott, MO Samimy, and Stephen A Arnette. Study of compressible mixing layers using filtered rayleigh scattering based visualizations. *AIAA journal*, 30(10):2567–2569, 1992.

[19] M Koochesfahani, PE Dimotakis, and JE Broadwell. A'flip'experiment in a chemically reacting turbulent mixing layer. *AIAA journal*, 23(8):1191–1194, 1985.

[20] MM Koochesfahani and PE Dimotakis. Mixing and chemical reactions in a turbulent liquid mixing layer. *Journal of Fluid Mechanics*, 170:83–112, 1986.

[21] NT Clemens and MG Mungal. Large-scale structure and entrainment in the supersonic mixing layer. *Journal of Fluid Mechanics*, 284:171–216, 1995.

[22] NT Clemens and PH Paul. Scalar measurements in compressible axisymmetric mixing layers. *Physics of Fluids*, 7(5):1071–1081, 1995.

[23] Tobin Christopher Island. Quantitative scalar measurements and mixing enhancement in compressible shear layers. 1997.

[24] Robert D Moser and Michael M Rogers. The three-dimensional evolution of a plane mixing layer: pairing and transition to turbulence. *Journal of Fluid Mechanics*, 247(1):275, 1993.

[25] Michael M Rogers and Robert D Moser. Direct simulation of a self-similar turbulent mixing layer. *Physics of Fluids*, 6(2):903–923, 1994.

[26] ND Sandham and WC Reynolds. Three-dimensional simulations of large eddies in the compressible mixing layer. *Journal of Fluid Mechanics*, 224:133–158, 1991.

[27] KH Luo and ND Sandham. On the formation of small scales in a compressible mixing layer. In *Direct and Large-Eddy Simulation I*, pages 335–346. Springer, 1994.

[28] S Sarkar. The stabilizing effect of compressibility in turbulent shear flow. *Journal of Fluid Mechanics*, 282:163–186, 1995.

[29] Jonathan B Freund, Sanjiva K Lele, and Parviz Moin. Compressibility effects in a turbulent annular mixing layer. part 1. turbulence and growth rate. *Journal of Fluid Mechanics*, 421:229–267, 2000.

[30] C Pantano and S Sarkar. A study of compressibility effects in the high-speed turbulent shear layer using direct simulation. *Journal of Fluid Mechanics*, 451:329–371, 2002.

[31] C Pantano, S Sarkar, and FA Williams. Mixing of a conserved scalar in a turbulent reacting shear layer. *Journal of Fluid Mechanics*, 481:291–328, 2003.

[32] PE Dimotakis. Turbulent free shear layer mixing and combustion. *High Speed Flight Propulsion Systems*, 137:265–340, 1991.

[33] Arjun Sharma, Rathakrishnan Bhaskaran, and Sanjiva K Lele. Large-eddy simulation of supersonic, turbulent mixing layers downstream of a splitter plate. *AIAA Paper*, 208, 2011.

[34] M.D. Slessor. *Aspects of turbulent-shear-layer dynamics and mixing*. PhD thesis, California Institute of Technology, 1998.

[35] Georgios Matheou and Paul E. Dimotakis. Scalar excursions in large-eddy simulations. *Journal of Computational Physics*, 327:97–120, 2016.

[36] Joseph Hirschfelder, R Byron Bird, and Charles F Curtiss. Molecular theory of gases and liquids. 1964.

[37] Thierry Poinsot and Denis Veynante. *Theoretical and numerical combustion*. RT Edwards, Inc., 2005.

[38] AW Vreman. An eddy-viscosity subgrid-scale model for turbulent shear flow: Algebraic theory and applications. *Physics of Fluids (1994-present)*, 16(10):3670–3681, 2004.

[39] Heinz Pitsch. Large-eddy simulation of turbulent combustion. *Annu. Rev. Fluid Mech.*, 38:453–482, 2006.

[40] Christer Fureby. LES for supersonic combustion. *AIAA Paper*, 5979:2012, 2012.

[41] Jesse A Fulton, Jack R Edwards, Andrew D Cutler, James C McDaniel, and Christopher P Goyne. Turbulence/chemistry interactions in a ramp-stabilized supersonic hydrogen-air diffusion flame. In *52nd Aerospace Sciences Meeting*, page 0627, 2014.

[42] JC Buell and P Huerre. Inflow/outflow boundary conditions and global dynamics of spatial mixing layers. *Center for Turbulence Research, Proceedings of the Summer Program*.

[43] Tim Colonius. Modeling artifical boundary conditions for compressible flows. *Annu. Rev. Fluid Mech.*, 36(1):310–345, 2004.

[44] Victor Granet, Olivier Vermorel, Thomas Léonard, Laurent Gicquel, and Thierry Poinsot. Comparison of nonreflecting outlet boundary conditions for compressible solvers on unstructured grids. *AIAA journal*, 48(10):2348–2364, 2010.

[45] C. S. Yoo and H. G. Im. Characteristic boundary conditions for simulations of compressible reacting flows with multi-dimensional, viscous and reaction effects. *Combust. Theory Model.*, 11(2):259–286, 2007.

[46] T. J. Poinsot and S. K. Lele. Boundary conditions for direct simulations of compressible viscous flows. *J. Comput. Phys.*, 101(1):104–129, 1992, arXiv:1011.1669v3.

[47] Guido Lodato, Pascale Domingo, and Luc Vervisch. Three-dimensional boundary conditions for direct and large-eddy simulation of compressible viscous flows. 227:5105–5143, 2008.

[48] John Rudy, David and Strikwerda. A Nonreflecting Outflow Boundary Condition for Subsonic Navier-Stokes Calculations. *J. Comput. Phys.*, 36:55–70, 1980.

[49] R Prosser. Improved boundary conditions for the direct numerical simulation of turbulent subsonic flows. i. inviscid flows. *Journal of Computational Physics*, 207(2):736–768, 2005.

[50] T. J. Poinsot and S. K. Lele. Boundary conditions for direct simulations of compressible viscous flows. *Journal of Computational Physics*, 101(1):104–129, 1992.

[51] Nitin S Dhamankar, Gregory A Blaisdell, and Anastasios S Lyrintzis. An overview of turbulent inflow boundary conditions for large eddy simulations. In *22nd AIAA Computational Fluid Dynamics Conference.(Dallas, USA, 2015)(cf. p. 55)*, 2015.

[52] Xiaohua Wu. Inflow turbulence generation methods. *Annual Review of Fluid Mechanics*, 49:23–49, 2017.

[53] Philippe R. Spalart and Jonathan H. Watmuff. Experimental and numerical study of a turbulent boundary layer with pressure gradients. *Journal of Fluid Mechanics*, 249:337–371, 1993.

[54] S. K. Xiong, Z. , Nagarajan, S. and Lele. Simple Method for Generating Inflow Turbulence. 42(10):1–3, 2004.

[55] Johan Larsson. Blending technique for compressible inflow turbulence : Algorithm localization and accuracy assessment. *J. Comput. Phys.*, 228(4):933–937, 2009.

[56] Anthony Keating, Ugo Piomelli, Elias Balaras, and Hans-Jakob Kaltenbach. A priori and a posteriori tests of inflow conditions for large-eddy simulation. *Physics of Fluids*, 16(12):4696–4712, 2004.

[57] JU Schlüter, H Pitsch, and P Moin. Large-eddy simulation inflow conditions for coupling with reynolds-averaged flow solvers. *AIAA Journal*, 42(3):478–484, 2004.

[58] Thomas S Lund, Xiaohua Wu, and Kyle D Squires. Generation of turbulent inflow data for spatially-developing boundary layer simulations. *Journal of Computational Physics*, 140(2):233–258, 1998.

[59] Gerald Urbin and Doyle Knight. Large-eddy simulation of a supersonic boundary layer using an unstructured grid. *AIAA journal*, 39(7):1288–1295, 2001.

[60] Pierre Sagaut, Eric Garnier, Eric Tromeur, Lionel Larcheveque, and Emmanuel Labourasse. Turbulent inflow conditions for large-eddy-simulation of compressible wall-bounded flows. *AIAA journal*, 42(3):469–477, 2004.

[61] Sheng Xu and M Pino Martin. Assessment of inflow boundary conditions for compressible turbulent boundary layers. *Physics of Fluids*, 16(7):2623–2639, 2004.

[62] PR Spalart, M Strelets, and A Travin. Direct numerical simulation of large-eddy-break-up devices in a boundary layer. *International Journal of Heat and Fluid Flow*, 27(5):902–910, 2006.

[63] A Ferrante and SE Elghobashi. A robust method for generating inflow conditions for direct simulations of spatially-developing turbulent boundary layers. *Journal of Computational Physics*, 198(1):372–387, 2004.

[64] Sangsan Lee, Sanjiva K Lele, and Parviz Moin. Simulation of spatially evolving turbulence and the applicability of taylors hypothesis in compressible flow. *Physics of Fluids A: Fluid Dynamics*, 4(7):1521–1530, 1992.

[65] Hung Le, Parviz Moin, and John Kim. Direct numerical simulation of turbulent flow over a backward-facing step. *Journal of fluid mechanics*, 330(1):349–374, 1997.

[66] Lars Davidson. Hybrid LES-RANS: inlet boundary conditions for flows including recirculation. In *TSFP Digital Library Online*. Begel House Inc., 2007.

[67] Rixin Yu and Xue-Song Bai. A fully divergence-free method for generation of inhomogeneous and anisotropic turbulence with large spatial variation. *Journal of Computational Physics*, 256:234–253, 2014.

[68] Gaofeng Wang, Matthieu Boileau, and Denis Veynante. Implementation of a dynamic thickened flame model for large eddy simulations of turbulent premixed combustion. *Combustion and Flame*, 158(11):2199–2213, 2011.

[69] Philippe Druault, S Lardeau, J-P Bonnet, F Coiffet, J Delville, E Lamballais, J-F Largeau, and L Perret. Generation of three-dimensional turbulent inlet conditions for large-eddy simulation. *AIAA journal*, 42(3):447–456, 2004.

[70] ND Sandham, YF Yao, and AA Lawal. Large-eddy simulation of transonic turbulent flow over a bump. *International Journal of Heat and Fluid Flow*, 24(4):584–595, 2003.

[71] Neil D Sandham and Richard D Sandberg. Direct numerical simulation of the early development of a turbulent mixing layer downstream of a splitter plate. *Journal of Turbulence*, (10):N1, 2009.

[72] Pramod Subbareddy, David Peterson, Graham V Candler, and Ivan Marusic. A synthetic inflow generation method using the attached eddy hypothesis. *AIAA paper*, 3672:2006, 2006.

[73] Makoto Matsumoto and Takuji Nishimura. Mersenne twister: a 623-dimensionally equidistributed uniform pseudo-random number generator. *ACM Transactions on Modeling and Computer Simulation (TOMACS)*, 8(1):3–30, 1998.

[74] Emile Touber and Neil D Sandham. Large-eddy simulation of low-frequency unsteadiness in a turbulent shock-induced separation bubble. *Theoretical and Computational Fluid Dynamics*, 23(2):79–107, 2009.

[75] Zheng-Tong Xie and Ian P Castro. Efficient generation of inflow conditions for large eddy simulation of street-scale flows. *Flow, turbulence and combustion*, 81(3):449–470, 2008.

[76] Sergio Pirozzoli and Matteo Bernardini. Turbulence in supersonic boundary layers at moderate reynolds number. *Journal of Fluid Mechanics*, 688:120–168, 2011.

[77] Thomas S Lund, Xiaohua Wu, and Kyle D Squires. Generation of turbulent inflow data for spatially-developing boundary layer simulations. *Journal of Computational Physics*, 140(2):233–258, 1998.

[78] David B De Graaff and John K Eaton. Reynolds-number scaling of the flat-plate turbulent boundary layer. *Journal of Fluid Mechanics*, 422:319–346, 2000.

[79] B Perthame. Boltzmann type schemes for gas dynamics and the entropy property. *SIAM Journal on Numerical Analysis*, 27(6):1405–1421, 1990.

[80] Benoit Perthame and Chi-Wang Shu. On positivity preserving finite volume schemes for Euler equations. *Numerische Mathematik*, 73(1):119–130, 1996.

[81] Timur Linde and Philip L Roe. Robust Euler codes. In *Thirteenth Computational Fluid Dynamics Conference, AIAA Paper-97-2098*, 1997.

[82] Bernd Einfeldt, Claus-Dieter Munz, Philip L Roe, and Björn Sjögreen. On Godunov-type methods near low densities. *Journal of Computational Physics*, 92(2):273–295, 1991.

[83] Meng-Sing Liou. A sequel to AUSM: AUSM$^+$. *Journal of Computational Physics*, 129(2):364–382, 1996.

[84] Xiangxiong Zhang and Chi-Wang Shu. On positivity-preserving high order discontinuous Galerkin schemes for compressible Euler equations on rectangular meshes. *Journal of Computational Physics*, 229(23):8918–8934, 2010.

[85] Xiangxiong Zhang and Chi-Wang Shu. On maximum-principle-satisfying high order schemes for scalar conservation laws. *Journal of Computational Physics*, 229(9):3091–3120, 2010.

[86] Xiangxiong Zhang and Chi-Wang Shu. Maximum-principle-satisfying and positivity-preserving high-order schemes for conservation laws: survey and new developments. *Proceedings of the Royal Society A: Mathematical, Physical and Engineering Science*, 467(2134):2752–2776, 2011.

[87] Xu-Dong Liu and Stanley Osher. Nonoscillatory high order accurate self-similar maximum principle satisfying shock capturing schemes I. *SIAM Journal on Numerical Analysis*, 33(2):760–779, 1996.

[88] Xiangyu Y Hu, Nikolaus A Adams, and Chi-Wang Shu. Positivity-preserving method for high-order conservative schemes solving compressible Euler equations. *Journal of Computational Physics*, 242:169–180, 2013.

[89] John von Neumann and Robert D Richtmyer. A method for the numerical calculation of hydrodynamic shocks. *Journal of Applied Physics*, 21(3):232–237, 1950.

[90] Sergio Pirozzoli. Numerical methods for high-speed flows. *Annual Review of Fluid Mechanics*, 43:163–194, 2011.

[91] Andrew W. Cook and William H. Cabot. A high-wavenumber viscosity for high-resolution numerical methods. *Journal of Computational Physics*, 195(2):594 – 601, 2004.

[92] B. Fiorina and S.K. Lele. An artificial nonlinear diffusivity method for supersonic reacting flows with shocks. *Journal of Computational Physics*, 222(1):246 – 264, 2007.

[93] Andrew W. Cook. Artificial fluid properties for large-eddy simulation of compressible turbulent mixing. *Physics of Fluids*, 19(5):055103, 2007.

[94] P. Subbareddy and G. Candler. A fully discrete, kinetic energy consistent finite-volume scheme for compressible flows. *Journal of Computational Physics*, 228:1347–1364, 2009.

[95] Sigal Gottlieb, Chi-Wang Shu, and Eitan Tadmor. Strong stability-preserving high-order time discretization methods. *SIAM Review*, 43(1):89–112, 2001.

[96] P.L. Roe. Approximate Riemann solvers, parameter vectors, and difference schemes. *Journal of Computational Physics*, 43(2):357–372, 1981.

[97] R.W. MacCormack and G.V. Candler. The solution of the Navier-Stokes equations using Gauss-Seidel line relaxation. *Computers and Fluids*, 17(1):135–150, 1989.

[98] F. Ducros, V. Ferrand, F. Nicoud, C. Weber, D. Darracq, C. Gacherieu, and T. Poinsot. Large-eddy simulation of shock/turbulence interaction. *Journal of Computational Physics*, 152:517–549, 1999.

[99] Jay P Boris and David L Book. Flux-corrected transport. I. SHASTA, A fluid transport algorithm that works. *Journal of Computational Physics*, 11(1):38–69, 1973.

[100] Steven T Zalesak. Fully multidimensional flux-corrected transport algorithms for fluids. *Journal of Computational Physics*, 31(3):335–362, 1979.

[101] Pramod K Subbareddy, Graham V Candler, and Pietro Ferrero. Scalar conservation in large eddy simulations of reacting flows. In *7th AIAA Theoretical Fluid Mechanics Conference*, page 3203, 2014.

[102] Pramod K Subbareddy, Anand Kartha, and Graham V Candler. Scalar conservation and boundedness in simulations of compressible flow. *Journal of Computational Physics*, 348:827–846, 2017.

[103] Hiroshi Terashima, Soshi Kawai, and Mitsuo Koshi. Consistent numerical diffusion terms for simulating compressible multicomponent flows. *Computers & Fluids*, 88:484–495, 2013.

[104] Amiram Harten. The artificial compression method for computation of shocks and contact discontinuities. III. Self-adjusting hybrid schemes. *Mathematics of Computation*, 32(142):363–389, 1978.

[105] Yu-Xin Ren, Hanxin Zhang, et al. A characteristic-wise hybrid compact-WENO scheme for solving hyperbolic conservation laws. *Journal of Computational Physics*, 192(2):365–386, 2003.

[106] Dimitri J Mavriplis. Revisiting the least-squares procedure for gradient reconstruction on unstructured meshes. *AIAA paper*, 3986:2003, 2003.

[107] Sung-Eun Kim, Boris Makarov, and Doru Caraeni. A multi-dimensional linear reconstruction scheme for arbitrary unstructured grids. *AIAA paper*, 3990:2003, 2003.

[108] Peter Kaps and Peter Rentrop. Generalized runge-kutta methods of order four with stepsize control for stiff ordinary differential equations. *Numerische Mathematik*, 33(1):55–68, 1979.

[109] Gilbert Strang. On the construction and comparison of difference schemes. *SIAM Journal on Numerical Analysis*, 5(3):506–517, 1968.

[110] Jack L Ziegler, Ralf Deiterding, Joseph E Shepherd, and Dale I Pullin. An adaptive high-order hybrid scheme for compressive, viscous flows with detailed chemistry. *Journal of Computational Physics*, 230(20):7598–7630, 2011.

[111] Eric Johnsen and Frank Ham. Preventing numerical errors generated by interface-capturing schemes in compressible multi-material flows. *Journal of Computational Physics*, 231(17):5705–5717, 2012.

[112] Smadar Karni. Multicomponent flow calculations by a consistent primitive algorithm. *Journal of Computational Physics*, 112(1):31–43, 1994.

[113] Rémi Abgrall. How to prevent pressure oscillations in multicomponent flow calculations: a quasi conservative approach. *Journal of Computational Physics*, 125(1):150–160, 1996.

[114] G Billet and R Abgrall. An adaptive shock-capturing algorithm for solving unsteady reactive flows. *Computers & Fluids*, 32(10):1473–1495, 2003.

[115] Yu Lv and Matthias Ihme. Discontinuous Galerkin method for multicomponent chemically reacting flows and combustion. *Journal of Computational Physics*, 270:105–137, 2014.

[116] Ryan W Houim and Kenneth K Kuo. A low-dissipation and time-accurate method for compressible multi-component flow with variable specific heat ratios. *Journal of Computational Physics*, 230(23):8527–8553, 2011.

[117] ND Sandham and Helen C Yee. A numerical study of a class of TVD schemes for compressible mixing layers. *NASA TM-102194 (1989)*, 1989.

[118] J-F Haas and Bradford Sturtevant. Interaction of weak shock waves with cylindrical and spherical gas inhomogeneities. *Journal of Fluid Mechanics*, 181:41–76, 1987.

[119] James J Quirk and Smadar Karni. On the dynamics of a shock–bubble interaction. *Journal of Fluid Mechanics*, 318:129–163, 1996.

[120] J. C. R. Hunt, A. A. Wray, and P. Moin. Eddies, stream, and convergence zones in turbulent flows. *Center for Turbulent Research Report*, 1988.

[121] Louis J Souverein, Pierre Dupont, Jean-Francois Debiève, Jean-Paul Dussauge, Bas W van Oudheusden, and Fulvio Scarano. Effect of interaction strength on unsteadiness in turbulent shock-wave-induced separations. *AIAA journal*, 48(7):1480, 2010.

[122] Jeffrey Komives. *Development and Validation of a Turbulence Wall Model for Compressible Flows with Heat Transfer*. PhD thesis, University of Minnesota, 2016.

[123] Frank M White and Isla Corfield. *Viscous fluid flow*, volume 3. McGraw-Hill Higher Education Boston, 2006.

[124] Soshi Kawai and Johan Larsson. Wall-modeling in large eddy simulation: Length scales, grid resolution, and accuracy. *Physics of Fluids*, 24(1):015105, 2012.

[125] Paul E. Dimotakis. Two-dimensional shear-layer entrainment. *AIAA journal*, 24(11):1791–1796, 1986.

[126] Luis Paulino Bernal. *The coherent structure of turbulent mixing layers. I. Similarity of the primary vortex structure. II. Secondary streamwise vortex structure.* PhD thesis, California Institute of Technology, 1981.

[127] Paul E Dimotakis. Turbulent mixing. *Annu. Rev. Fluid Mech.*, 37:329–356, 2005.

[128] Paul E Dimotakis. The mixing transition in turbulent flows. *Journal of Fluid Mechanics*, 409:69–98, 2000.

[129] MG Mungal and PE Dimotakis. Mixing and combustion with low heat release in a turbulent shear layer. *Journal of Fluid Mechanics*, 148:349–382, 1984.

[130] JL Hall, PE Dimotakis, and H Rosemann. Experiments in nonreacting compressible shear layers. *AIAA journal*, 31(12):2247–2254, 1993.

[131] NL Messersmith and JC Dutton. Characteristic features of large structures in compressible mixing layers. *AIAA journal*, 34(9):1814–1821, 1996.

[132] J Bonnet, J Debisschop, and O Chambres. Experimental studies of the turbulent structure of supersonic mixing layers. In *31st Aerospace Sciences Meeting*, page 217, 1993.

[133] Peter Bradshaw. Compressible turbulent shear layers. *Annual Review of Fluid Mechanics*, 9(1):33–52, 1977.

[134] Dimitri Papamoschou and Anatol Roshko. The compressible turbulent shear layer: an experimental study. *Journal of Fluid Mechanics*, 197:453–477, 1988.

[135] GS Elliott and M Samimy. Compressibility effects in free shear layers. *Physics of Fluids A: Fluid Dynamics*, 2(7):1231–1240, 1990.

[136] Steven G Goebel and J Craig Dutton. Experimental study of compressible turbulent mixing layers. *AIAA journal*, 29(4):538–546, 1991.

[137] JC Dutton, RF Burr, SG Goebel, and NL Messersmith. Compressibility and mixing in turbulent free shear layers. In *12th Symposium on Turbulence*, volume 1, page 22, 1990.

[138] JC Hermanson and PE Dimotakis. Effects of heat release in a turbulent, reacting shear layer. *Journal of Fluid Mechanics*, 199:333–375, 1989.

[139] Jeffery Lawrence Hall. *An experimental investigation of structure, mixing and combustion in compressible turbulent shear layers*. PhD thesis, California Institute of Technology, 1991.

[140] P Bradshaw. The effect of initial conditions on the development of a free shear layer. *Journal of Fluid Mechanics*, 26(02):225–236, 1966.

[141] C Chandrsuda, Rabindra D Mehta, AD Weir, and Peter Bradshaw. Effect of free-stream turbulence on large structure in turbulent mixing layers. *Journal of Fluid Mechanics*, 85(4):693–704, 1978.

[142] James H Bell and Rabindra D Mehta. Development of a two-stream mixing layer from tripped and untripped boundary layers. *AIAA journal*, 28(12):2034–2042, 1990.

[143] SG Goebel, JC Dutton, H Krier, and JP Renie. Mean and turbulent velocity measurements of supersonic mixing layers. *Experiments in Fluids*, 8(5):263–272, 1990.

[144] Song Fu and Qibing Li. Numerical simulation of compressible mixing layers. *International journal of heat and fluid flow*, 27(5):895–901, 2006.

[145] Albertus Willem Vreman, ND Sandham, and KH Luo. Compressible mixing layer growth rate and turbulence characteristics. *Journal of Fluid Mechanics*, 320:235–258, 1996.

[146] MJ Day, WC Reynolds, and NN Mansour. The structure of the compressible reacting mixing layer: Insights from linear stability analysis. *Physics of Fluids*, 10(4):993–1007, 1998.

[147] MJ Day, NN Mansour, and WC Reynolds. Nonlinear stability and structure of compressible reacting mixing layers. *Journal of Fluid Mechanics*, 446:375–408, 2001.

[148] PA McMurtry, James J Riley, and RW Metcalfe. Effects of heat release on the large-scale structure in turbulent mixing layers. *Journal of Fluid Mechanics*, 199:297–332, 1989.

[149] Richard S Miller, CK Madnia, and P Givi. Structure of a turbulent reacting mixing layer. *Combustion science and technology*, 99(1-3):1–36, 1994.

[150] FA Jaberi, PJ Colucci, S James, P Givi, and SB Pope. Filtered mass density function for large-eddy simulation of turbulent reacting flows. *Journal of Fluid Mechanics*, 401:85–121, 1999.

[151] Inga Mahle. Direct and large-eddy simulation of inert and reacting compressible turbulent shear layers. *Dr. Ing. thesis, Technische Universität München (under preparation)*, 2007.

[152] William A McMullan. Spanwise domain effects on the evolution of the plane turbulent mixing layer. *International Journal of Computational Fluid Dynamics*, 29(6-8):333–345, 2015.

[153] William A McMullan, S Gao, and Christopher M Coats. Organised large structure in the post-transition mixing layer. part 2. large-eddy simulation. *Journal of Fluid Mechanics*, 762:302–343, 2015.

[154] BJ Delarue and SB Pope. Calculations of subsonic and supersonic turbulent reacting mixing layers using probability density function methods. *Physics of Fluids*, 10(2):487–498, 1998.

[155] MRH Sheikhi, P Givi, and SB Pope. Velocity-scalar filtered mass density function for large eddy simulation of turbulent reacting flows. *Physics of fluids*, 19(9):095106, 2007.

[156] Pedro José Martínez Ferrer, Guillaume Lehnasch, and Arnaud Mura. Compressibility and heat release effects in high-speed reactive mixing layers i.: Growth rates and turbulence characteristics. *Combustion and Flame*, 180:284–303, 2017.

[157] Pedro José Martínez Ferrer, Guillaume Lehnasch, and Arnaud Mura. Compressibility and heat release effects in high-speed reactive mixing layers ii. structure of the stabilization zone and modeling issues relevant to turbulent combustion in supersonic flows. *Combustion and Flame*, 180:304–320, 2017.

[158] Pietro Ferrero, Anand Kartha, Pramod K Subbareddy, Graham V Candler, and Paul E Dimotakis. Les of a high-reynolds number, chemically reacting mixing layer. *AIAA Paper*, 2013.

[159] P. Ferrero. *A stochastic particle method for the investigation of turbulence/chemistry interactions in large-eddy simulations of turbulent reacting fows.* PhD thesis, University of Minnesota, 2007.

[160] M Klein, A Sadiki, and J Janicka. A digital filter based generation of inflow data for spatially developing direct numerical or large eddy simulations. *Journal of computational Physics*, 186(2):652–665, 2003.

[161] Aristides M Bonanos, M Jeffrey, and Paul E Dimotakis. Molecular mixing and flowfield measurements in an expansion-ramp combustion: Supersonic flow. *AIAA 2007*, 5417, 2007.

[162] Chun Sang Yoo and Hong G Im. Characteristic boundary conditions for simulations of compressible reacting flows with multi-dimensional, viscous and reaction effects. *Combustion Theory and Modelling*, 11(2):259–286, 2007.

[163] Lyle M Pickett and Jaal B Ghandhi. Passive scalar mixing in a planar shear layer with laminar and turbulent inlet conditions. *Physics of fluids*, 14(3):985–998, 2002.

[164] Qiang Zhou, Feng He, and MY Shen. Direct numerical simulation of a spatially developing compressible plane mixing layer: flow structures and mean flow properties. *Journal of Fluid Mechanics*, 711:437, 2012.

[165] Bert Vreman, Bernard Geurts, and Hans Kuerten. Large-eddy simulation of the turbulent mixing layer. *Journal of Fluid Mechanics*, 339:357–390, 1997.

[166] PE Dimotakis, JE Broadwell, and MG Mungal. Turbulent mixing and combustion in a reacting shear layer. *AIAA journal*, 22(6):797–800, 1984.

[167] Paul E Dimotakis, Graham V Candler, Lance Jacobsen, Michael Holden, Daniel I Meiron, and Joseph A Schetz. Design, performance, and operation of efficient ramjet/scramjet combined cycle hypersonic propulsion. Technical report, DTIC Document, 2009.

[168] Georgios Matheou, Aristides M Bonanos, Carlos Pantano, and Paul E Dimotakis. Large-eddy simulation of mixing in a recirculating shear flow. *Journal of Fluid Mechanics*, 646:375–414, 2010.

[169] Aristides M Bonanos, Jeffrey M Bergthorson, and Paul E Dimotakis. Mixing measurements in a supersonic expansion-ramp combustor. *Flow, Turbulence and Combustion*, 80(4):489–506, 2008.

[170] Graham V Candler, Anand Kartha, Pramod K Subbareddy, and Paul Dimotakis. LES of the volvo combustion experiment with an ignition-delay scalar. *AIAA Conference*, 2018.

[171] Sidharth GS, Anand Kartha, and Graham V Candler. Filtered velocity based LES of mixing in high speed recirculating shear flow. *AIAA Conference*, 2016.